

¹ **Searches for Supersymmetry using the α_T**
² **variable with the CMS detector at the LHC**

³ Darren Burton

⁴ Imperial College London
⁵ Department of Physics

⁶ A thesis submitted to Imperial College London
⁷ for the degree of Doctor of Philosophy

Abstract

10

Declaration

11

I, the author of this thesis, declare that the work presented within this
document to be my own. The work presented in Chapters 3.4.1, 4 and 5
is a result of the authors own work or that of which I have been a major
contributor unless explicitly stated otherwise, and is carried out within the
context of the Imperial College London and CERN SUSY groups, itself a
subsection of the greater CMS collaboration. All figures and studies taken
from external sources are referenced appropriately throughout this document.

18

Darren Burton

19

Acknowledgements

20

Of the many people who deserve thanks, some are particularly prominent....

Preface

Contents

23	List of Figures	viii
24	List of Tables	xii
25	1. Introduction	2
26	2. A Theoretical Overview	5
27	2.1. The Standard Model	5
28	2.1.1. Gauge Symmetries of the SM	7
29	2.1.2. The Electroweak Sector and Electroweak Symmetry Breaking	9
30	2.2. Motivation for Physics Beyond the Standard Model	13
31	2.3. Supersymmetry Overview	15
32	2.3.1. R-Parity	16
33	2.4. Experimental signatures of SUSY at the LHC	17
34	2.4.1. Simplified Models	18
35	3. The LHC and the CMS Detector	20
36	3.1. The LHC	20
37	3.2. The CMS detector	23
38	3.2.1. Detector Subsystems	23
39	3.2.2. Tracker	24
40	3.2.3. Electromagnetic Calorimeter	25
41	3.2.4. Hadronic Calorimeter	26
42	3.2.5. Muon Systems	28
43	3.3. Event Reconstruction and Object Definition	28
44	3.3.1. Jets	28
45	3.3.2. B-tagging	30
46	3.4. Triggering System	32
47	3.4.1. The Level-1 Trigger	34

48	3.4.2. L1 Trigger Jet Algorithm	35
49	3.4.3. Measuring L1 Jet Trigger Efficiencies	36
50	3.4.4. Effects of the L1 Jet Seed	38
51	3.4.5. Robustness of L1 Jet Performance against Pile-up	41
52	3.4.6. Summary	43
53	4. SUSY searches in Hadronic Final States	45
54	4.1. An introduction to the α_T search	46
55	4.1.1. The α_T variable	48
56	4.2. Search Strategy	50
57	4.2.1. Physics Objects	53
58	4.2.2. Event Selection	55
59	4.2.3. Control Sample Definition	58
60	4.2.4. Estimating the QCD background multi-jet background	65
61	4.3. Trigger Strategy	65
62	4.4. A method to determine MC yields with higher statistical precision	66
63	4.5. Measuring MC normalisation factors via H_T sidebands	66
64	4.6. Systematic Uncertainties on Transfer Factors	66
65	4.7. Searches for Natural SUSY with B-tag templates.	66
66	5. Results	67
67	5.1. Statistical Interpretation	67
68	5.2. Interpretation in Simplified Signal Models	67
69	A. Miscellaneous	68
70	A.1. Noise Filters	68
71	A.2. Primary Vertices	69
72	B. L1 Jets	70
73	B.1. Jet matching efficiencies	70
74	B.2. Leading Jet Energy Resolution	71
75	B.3. Resolution for Energy Sum Quantities	74
76	Bibliography	80

⁷⁷ List of Figures

⁷⁸ 2.1.	One loop quantum corrections to the Higgs squared mass parameter m_h^2 due to a fermion.	⁷⁹ 14
⁸⁰ 2.2.	Two example simplified model decay chains.	⁸⁰ 19
⁸¹ 3.1.	A top down layout of the LHC, with the position of the four main detectors labelled.	⁸² 21
⁸³ 3.2.	The total integrated luminosity delivered to and collected by Compact Muon Solenoid (CMS) during the 2012 8 TeV pp runs	⁸⁴ 22
⁸⁵ 3.3.	A pictorial depiction of the CMS detector.	⁸⁵ 24
⁸⁶ 3.4.	Illustration of the CMS Electromagnetic CALorimeter (ECAL).	⁸⁶ 26
⁸⁷ 3.5.	Schematic of the CMS Hadronic CALorimeter (HCAL).	⁸⁷ 27
⁸⁸ 3.6.	Combined Secondary Vertex (CSV) algorithm discriminator values in enriched $t\bar{t}$ and inclusive multi jet samples	⁸⁹ 31
⁹⁰ 3.7.	Data/MC b-tag scale factors derived using the Combined Secondary Vertex Medium Working Point (CSVM) tagger.	⁹¹ 32
⁹² 3.8.	Data/MC mis-tag scale factors derived using the CSVM tagger.	⁹² 33
⁹³ 3.9.	The CMS Level 1 Trigger (L1) Trigger system.	⁹³ 34
⁹⁴ 3.10.	Illustration of the Level-1 jet finding algorithm.	⁹⁴ 36
⁹⁵ 3.11.	L1 jet efficiency turn-on curves as a function of the offline CaloJet and PFJet E_T	⁹⁶ 38
⁹⁷ 3.12.	L1 jet efficiency turn-on curves as a function of the offline CaloJet E_T for the 2012 run period B and C.	⁹⁸ 39

99	3.13. Trigger cross section for the L1HTT150 trigger path.	40
100	3.14. L1 H_T efficiency turn-on curves as a function of the offline CaloJet H_T	41
101	3.15. L1 jet efficiency turn-on curves as a function of the leading offline E_T Calo	
102	(left) and PF (right) jet, for low, medium and high pile-up conditions.	42
103	3.16. Fit values from an Exponentially Modified Gaussian (EMG) function fitted	
104	to the resolution plots of leading Calo jet E_T measured as a function of	
105	$\frac{(L1\ E_T - \text{Offline}\ E_T)}{\text{Offline}\ E_T}$ for low, medium and high pile-up conditions.	43
106	3.17. Fit values from an EMG function fitted to the resolution plots of leading	
107	PF jet E_T measured as a function of $\frac{(L1\ E_T - \text{Offline}\ E_T)}{\text{Offline}\ E_T}$ for low, medium and	
108	high pile-up conditions.	44
109	4.1. Reconstructed offline H_T for 11.7fb^{-1} of data after a basic pre-selection.	48
110	4.2. The event topologies of background QCD dijet events (right) and a generic	
111	SUPERSYmmetry (SUSY) signature with genuine Z_T (left).	48
112	4.3. The α_T distributions for the low 2-3 (left) and high ≥ 4 (right) jet	
113	multiplicities after a full analysis selection and shown for $H_T > 375$	50
114	4.4. Pictorial depiction of the analysis strategy employed by the α_T search to	
115	increase sensitivity to a wide spectra of SUSY models.	52
116	4.5. Data/MC comparisons of key variables for the hadronic signal region.	58
117	4.6. Data/MC comparisons of key variables for the $\mu + \text{jets}$ selection.	61
118	4.7. Data/MC comparisons of key variables for the $\mu\mu + \text{jets}$ selection.	63
119	4.8. Data/MC comparisons of key variables for the $\gamma + \text{jets}$ selection.	64
120	B.1. Leading jet matching efficiency as a function of the offline CaloJet E_T	70
121	B.2. Resolution plots of the leading offline Calo E_T measured as a function of	
122	$\frac{(L1\ E_T - \text{Offline}\ E_T)}{\text{Offline}\ E_T}$ for low (a), medium (b) and high (c) pile-up conditions.	72
123	B.3. Resolution plots of the leading off-line PF E_T measured as a function of	
124	$\frac{(L1\ E_T - \text{Offline}\ E_T)}{\text{Offline}\ E_T}$ for low (a), medium (b) and high (c) pile-up conditions.	74

125	B.4. $\sum E_T$ resolution parameters in bins of Calo $\sum E_T$ measured for the defined low, medium and high pile up conditions.	75
126		
127	B.5. $\sum E_T$ resolution parameters in bins of PF $\sum E_T$ measured for the defined low, medium and high pile up conditions.	75
128		
129	B.6. \cancel{E}_T resolution parameters in bins of Calo \cancel{E}_T measured for the defined low, medium and high pile up conditions.	76
130		
131	B.7. \cancel{E}_T resolution parameters in bins of PF \cancel{E}_T measured for the defined low, medium and high pile up conditions.	76
132		
133	B.8. H_T resolution parameters in bins of Calo H_T measured for the defined low, medium and high pile up conditions.	77
134		
135	B.9. H_T resolution parameters in bins of PF H_T measured for the defined low, medium and high pile up conditions.	77
136		
137	B.10. \cancel{H}_T resolution parameters in bins of Calo \cancel{H}_T measured for the defined low, medium and high pile up conditions.	78
138		
139	B.11. \cancel{H}_T resolution parameters in bins of PF \cancel{H}_T measured for the defined low, medium and high pile up conditions.	78
140		

¹⁴¹ List of Tables

¹⁴²	2.1. The fundamental particles of the Standard Model (SM), with spin, charge and mass displayed.	6
¹⁴³		
¹⁴⁴	3.1. Results of a cumulative EMG function fit to the turn-on curves for L1 single jet triggers in 2012 Run Period C.	38
¹⁴⁵		
¹⁴⁶	3.2. Results of a cumulative EMG function fit to the turn-on curves for L1 single jet triggers in the 2012 run period B and C.	39
¹⁴⁷		
¹⁴⁸	3.3. Results of a cumulative EMG function fit to the turn-on curves for H_T in 2012 run period B and C.	40
¹⁴⁹		
¹⁵⁰	3.4. Results of a cumulative EMG function fit to the efficiency turn-on curves for L1 single jet triggers in the 2012 run period C, for low,medium and high pile-up conditions.	41
¹⁵¹		
¹⁵²		
¹⁵³	3.5. Results of a cumulative EMG function fit to the efficiency turn-on curves for Level-1 single jet triggers in the 2012 run period C, for low,medium and high pile-up conditions.	42
¹⁵⁴		
¹⁵⁵		
¹⁵⁶	4.1. A summary of the Simplified Model Spectra (SMS) models interpreted in this analysis, involving both direct (D) and gluino-induced (G) production of squarks and their decays.	46
¹⁵⁷		
¹⁵⁸		
¹⁵⁹	4.2. Jet Identification criteria for the “loose” CaloJet ID used with the analysis.	53
¹⁶⁰		
¹⁶¹	4.3. Muon Identification criteria used within the analysis for selection/veto purposes in the muon control/signal selections.	54
¹⁶²		
¹⁶³	4.4. Photon Identification criteria used within the analysis for selection/veto purposes in the $\gamma +$ jets control/signal selections.	54

164	4.5. Electron Identification criteria used within the analysis for veto purposes.	55
165	4.6. Jet thresholds used in the three H_T regions of the analysis.	56
166	B.1. Results of a cumulative EMG function fit to the turn-on curves for the	
167	matching efficiency of the leading jet in an event to a Level-1 jet in run	
168	2012C and 2012B data.	71

¹⁶⁹

“The Universe is about 1,000,000 years old.”

— Matthew Kenzie, 1987-present : Discoverer of the Higgs Boson.

¹⁷⁰

Chapter 1.

¹⁷¹ Introduction

¹⁷² During the 20th century great advances have been made in our understanding of the
¹⁷³ universe, where it comes from, where it is going and what it is made of. The Standard
¹⁷⁴ Model (**SM**) first formulated in the 1960's is one of the crowning achievements in science's
¹⁷⁵ quest to explain the most fundamental processes and interactions that make up our
¹⁷⁶ universe. It has provided a highly successful explanation of a wide range of phenomena
¹⁷⁷ in Particle Physics and has stood up to extensive experimental scrutiny [1].

¹⁷⁸ Despite it's successes it is not a complete theory, with significant questions remaining
¹⁷⁹ unanswered. It describes only three of the four known forces with gravity not incorpo-
¹⁸⁰ rated within the framework of the **SM**. Cosmological experiments infer that just $\sim 4\%$
¹⁸¹ of the observable universe exists as matter, with elusive "Dark Matter" accounting for a
¹⁸² further $\sim 23\%$ [2]. However no particle predicted by the **SM** is able to account for it. At
¹⁸³ higher energy scales and small distances the (non-)unification of the fundamental forces
¹⁸⁴ point to problems with the **SM** at least at higher energies not yet probed experimentally.

¹⁸⁵ Many theories exist as extensions to the **SM** and predict a range of observables
¹⁸⁶ that can be detected at the Large Hadron Collider (**LHC**) of which SUperSYmmetry
¹⁸⁷ (**SUSY**) is one such example. It predicts a new symmetry of nature in which all current
¹⁸⁸ particles in the **SM** would have a corresponding supersymmetric partner. Common to
¹⁸⁹ most Supersymmetric theories is a stable, weakly interacting Lightest Supersymmetric
¹⁹⁰ Partner (**LSP**), which has the properties of a possible dark matter candidate. The **SM**
¹⁹¹ and the main principles of Supersymmetric theories are outlined in Chapter 2, with
¹⁹² emphasis on placed on how experimental signatures of **SUSY** may reveal themselves at
¹⁹³ the **LHC**.

194 The experimental goal of the **LHC** is to further test the framework of the **SM**,
195 exploring the TeV mass scale for the first time, and to seek a connection between the
196 particles produced in proton collisions and dark matter. The first new discovery by
197 this extraordinary machine was announced on the 4th of July 2012. The long-awaited
198 discovery was the culmination decades of experimental endeavours in the search for the
199 Higgs boson, providing an answer to the mechanism of electroweak symmetry breaking
200 within the **SM** [3][4].

201 This discovery was made possible through data taken by the two multi purpose
202 detectors (**CMS** and A Toroidal LHC ApparatuS (**ATLAS**)) located on the **LHC** ring.
203 An experimental description of the **CMS** detector and the **LHC** is described in Chapter 3,
204 including some of the object reconstruction used by **CMS** in searches for **SUSY** signatures.
205 The performance of the **CMS** Level-1 calorimeter trigger, benchmarked by the author is
206 also included within this chapter.

207 The analysis conducted by the author is detailed within Chapter 4. This chapter
208 contains a description of the search for evidence of the production of Supersymmetric
209 particles at the **LHC**. The main basis of the search centres around the kinematic
210 dimensionless α_T variable, which provides strong rejection of backgrounds with fake
211 missing energy signatures whilst maintaining good sensitivity to a variety of **SUSY**
212 topologies. The author's work as an integral part of the analysis group is documented in
213 detail, which has culminated in numerous publications over the past two years. The latest
214 of which was published in the European Physical Journal C (**EPJC**) [5] and contains the
215 results which are discussed within this and the sequential Chapter.

216 The author in particular has played a major role in the extension of the α_T analysis into
217 the additional b-tagged and jet multiplicity dimensions increasing the sensitivity of the
218 analysis to a range of **SUSY** topologies. Additionally the author has worked extensively
219 in both increasing the statistical precision of electroweak predictions measured from
220 simulation through analytical techniques, and the derivation of a data driven systematic
221 uncertainty through the establishment of closure tests within the control samples of the
222 analysis.

223 Also included within this Chapter is a method to search for **SUSY** signatures which
224 are rich in top and bottom flavoured jet final states. A parametrisation of the b-tagging
225 distribution for different Electroweak processes is used to establish templates, which
226 are then used to estimate the expected number of 3 or 4 b-tagged jet events from **SM**

227 processes. The α_T search is used as a cross check for this template method to establish
228 it's functionality.

229 Finally the interpretation of such results within the framework of a variety of Simplified
230 Model Spectra (**SMS**), which describe an array of possible **SUSY** event topologies is
231 documented in Chapter 5. A description of the statistical model used to derive these
232 interpretations and the possible implications of the results presented in this thesis is
233 discussed within this Chapter. Natural units are used throughout this thesis in which \hbar
234 = c = 1.

Chapter 2.

²³⁵ A Theoretical Overview

²³⁶ Within this chapter, a brief introduction and background to the **SM** is given. Its success
²³⁷ as a rigorously tested and widely accepted theory is discussed as well as the deficiencies
²³⁸ with this theory that hint there this theory is not a complete description of our universe.
²³⁹ The motivations for new physics at the TeV scale and in particular Supersymmetric
²⁴⁰ theories are outlined within Section (2.3), with the chapter concluding with how an
²⁴¹ experimental signature of such theories can be produced and observed at the **LHC**,
²⁴² Section (2.4).

²⁴³ 2.1. The Standard Model

²⁴⁴ The **SM** is the name given to the relativistic Quantum Field Theory (**QFT**), where
²⁴⁵ particles are represented as excitations of fields, which describes the interactions and
²⁴⁶ properties of all the known elementary particles [6][7][8][9]. It is a renormalisable field
²⁴⁷ theory which contains three symmetries: $SU(3)$ for colour charge, $SU(2)$ for weak isospin
²⁴⁸ and $U(1)$ relating to weak hyper charge, which require its Lagrangian \mathcal{L}_{SM} to be invariant
²⁴⁹ under local gauge transformation.

²⁵⁰ Within the **SM** theory, matter is composed of spin $\frac{1}{2}$ fermions, which interact with each
²⁵¹ other via the exchange of spin-1 gauge bosons. A summary of the known fundamental
²⁵² fermions and bosons is given in Table 2.1.

²⁵³ Fermions are separated into quarks and leptons of which only quarks interact with
²⁵⁴ the strong nuclear force. Quarks unlike leptons are not seen as free particles in nature,
²⁵⁵ but rather exist only within baryons, composed of three quarks with an overall integer

Particle	Symbol	Spin	Charge	Mass (GeV)
First Generation Fermions				
Electron Neutrino	ν_e	$\frac{1}{2}$	0	$< 2.2 \times 10^{-6}$
Electron	e	$\frac{1}{2}$	-1	0.51×10^{-3}
Up Quark	u	$\frac{1}{2}$	$\frac{2}{3}$	$2.3^{+0.7}_{-0.5} \times 10^{-3}$
Down Quark	d	$\frac{1}{2}$	$-\frac{1}{3}$	$4.8^{+0.7}_{-0.3} \times 10^{-3}$
Second Generation Fermions				
Muon Neutrino	ν_μ	$\frac{1}{2}$	0	-
Muon	μ	$\frac{1}{2}$	-1	1.05×10^{-3}
Charm Quark	c	$\frac{1}{2}$	$\frac{2}{3}$	1.275 ± 0.025
Strange Quark	s	$\frac{1}{2}$	$-\frac{1}{3}$	$95 \pm 5 \times 10^{-3}$
Third Generation Fermions				
Tau Neutrino	ν_τ	$\frac{1}{2}$	0	-
Tau	τ	$\frac{1}{2}$	-1	1.77
Top Quark	t	$\frac{1}{2}$	$\frac{2}{3}$	173.5 ± 0.8
Bottom Quark	b	$\frac{1}{2}$	$-\frac{1}{3}$	4.65 ± 0.03
Gauge Bosons				
Photon	γ	1	0	0
W Boson	W^\pm	1	± 1	80.385 ± 0.015
Z Boson	Z	1	0	91.187 ± 0.002
Gluons	g	1	0	0
Higgs Boson	H	0	0	125.3 ± 0.5 [4]

Table 2.1.: The fundamental particles of the SM, with spin, charge and mass displayed. Latest mass measurements taken from [1].

charge, and quark-anti-quark pairs called mesons. Both leptons and quarks are grouped into three generations which have the same properties, but with ascending mass in each subsequent generation.

The gauge bosons mediate the interactions between fermions. The field theories of Quantum Electro-Dynamics (QED) and Quantum Chromo-Dynamics (QCD), yield massless mediator bosons, the photon and eight coloured gluons which are consequences of the gauge invariance of those theories, detailed in Section (2.1.1).

The unification of the electromagnetic and weak-nuclear forces into the current Electroweak theory yield the weak gauge bosons, W^\pm and Z through the mixing of the associated gauge fields. The force carriers of this theory were experimentally detected by

266 the observation of weak neutral current, discovered in 1973 in the Gargamelle bubble
267 chamber located at European Organization for Nuclear Research (**CERN**) [10], with the
268 masses of and the weak gauge bosons measured by the UA1 and U2 experiments at the
269 Super Proton Synchrotron (**SPS**) collider in 1983 [11][12].

270 2.1.1. Gauge Symmetries of the SM

271 Symmetries are of fundamental importance in the description of physical phenomena.
272 Noether's theorem states that for a dynamical system, the consequence of any symmetry
273 is an associated conserved quantity [13]. Invariance under translations, rotations, and
274 Lorentz transformations in physical systems lead to conservation of momentum, energy
275 and angular momentum.

276 In the **SM**, a quantum theory described by Lagrangian formalism, the weak, strong and
277 electromagnetic interactions are described in terms of “gauge theories”. A gauge theory
278 possesses invariance under a set of “local transformations”, which are transformations
279 whose parameters are space-time dependent. The requirement of gauge invariance within
280 the **SM** necessitates the introduction of force-mediating gauge bosons and interactions
281 between fermions and the bosons themselves. Given the nature of the topics covered by
282 this thesis, the formulation of Electroweak Sector (**EWK**) within the **SM** Lagrangian is
283 reviewed within this section.

284 The simplest example of the application of the principle of local gauge invariance
285 within the **SM** is in Quantum Electro-Dynamics (**QED**), the consequences of which
286 require a massless photon field [14][15].

287 Starting from the free Dirac Lagrangian written as

$$\mathcal{L} = \bar{\psi}(i\gamma^\mu \partial_\mu - m)\psi, \quad (2.1)$$

288 where ψ represents a free non interacting fermionic field, with the matrices $\gamma^\mu, \mu \in$
289 $0, 1, 2, 3$ defined by the anti commutator relationship $\gamma^\mu \gamma^\nu + \gamma^\nu \gamma^\mu = 2\eta^{\mu\nu} I_4$ where $\eta^{\mu\nu}$ is
290 the flat space-time metric $(+, -, -, -)$ and I_4 is the 4×4 identity matrix.

291 Under a local U(1) abelian gauge transformation in which ψ transforms as:

$$\psi(x) \rightarrow \psi'(x) = e^{i\theta(x)}\psi(x) \quad \bar{\psi}(x) \rightarrow \bar{\psi}'(x) = e^{i\theta(x)}\bar{\psi}(x) \quad (2.2)$$

292 the kinetic term of the Lagrangian does not remain invariant, due to the partial
293 derivative interposed between the $\bar{\psi}$ and ψ yielding,

$$\partial_\mu \psi \rightarrow e^{i\theta(x)} \partial_\mu \psi + i e^{i\theta(x)} \psi \partial_\mu \theta. \quad (2.3)$$

294 To ensure that \mathcal{L} remains invariant, a modified derivative, D_μ , that transforms
295 covariantly under phase transformations is introduced. In doing this a vector field A_μ
296 with transformation properties that cancel out the unwanted term in (2.3) must also be
297 included,

$$D_\mu \equiv \partial_\mu - ieA_\mu, \quad A_\mu \rightarrow A_\mu + \frac{1}{e} \partial_\mu \theta. \quad (2.4)$$

298 Invariance of the Lagrangian is then achieved by replacing ∂_μ by D_μ :

$$\begin{aligned} \mathcal{L} &= i\bar{\psi}\gamma^\mu D_\mu \psi - m\bar{\psi}\psi \\ &= \bar{\psi}(i\gamma^\mu \partial_\mu - m)\psi + e\bar{\psi}\gamma^\mu \psi A_\mu \end{aligned} \quad (2.5)$$

299 An additional interaction term is now present in the Lagrangian, coupling the Dirac
300 particle to this vector field, which is interpreted as the photon in QED. To regard this
301 new field as the physical photon field, a term corresponding to its kinetic energy must be
302 added to the Lagrangian from Equation (2.5). Since this term must also be invariant
303 under the conditions of Equation (2.4), it is defined in the form $F_{\mu\nu} = \partial^\mu A^\nu - \partial^\nu A^\mu$.

304 This then leads to the Lagrangian of QED:

$$\mathcal{L}_{QED} = \underbrace{i\bar{\psi}\gamma^\mu\partial_\mu\psi - \frac{1}{4}F_{\mu\nu}F^{\mu\nu}}_{\text{kinetic term}} + \underbrace{m\bar{\psi}\psi}_{\text{mass term}} + \underbrace{e\bar{\psi}\gamma^\mu\psi A_\mu}_{\text{interaction term}} \quad (2.6)$$

305 Within the Lagrangian there remains no mass term of the form $m^2A_\mu A^\mu$, which is
 306 prohibited by gauge invariance. This implies that the gauge particle, the photon, must
 307 be massless.

308 2.1.2. The Electroweak Sector and Electroweak Symmetry 309 Breaking

310 The same application of gauge symmetry and the requirement of local gauge invariance
 311 can be used to unify QED and the Weak force in the Electroweak Sector (EWK).
 312 The nature of EWK interactions is encompassed within a Lagrangian invariant under
 313 transformations of the group $SU(2)_L \times U(1)_Y$.

314 The weak interactions from experimental observation [16], are known to violate parity
 315 and are therefore not symmetric under interchange of left and right helicity fermions.
 316 Thus within the SM the left and right handed parts of these fermion fields are treated
 317 separately. A fermion field is then split into two left and right handed chiral components,
 318 $\psi = \psi_L + \psi_R$, where $\psi_{L/R} = (1 \pm \gamma^5)\psi$.

319 The $SU(2)_L$ group is the special unitary group of 2×2 matrices U satisfying $UU^\dagger = I$
 320 and $\det(U) = 1$. It may be written in the form $U = e^{-i\omega_i T_i}$, with the generators of the
 321 group $T_i = \frac{1}{2}\tau_i$ where τ_i , $i \in 1,2,3$ being the 2×2 Pauli matrices

$$\tau_1 = \begin{pmatrix} 0 & 1 \\ 1 & 0 \end{pmatrix} \quad \tau_2 = \begin{pmatrix} 0 & -i \\ i & 0 \end{pmatrix} \quad \tau_3 = \begin{pmatrix} 1 & 0 \\ 0 & -1 \end{pmatrix}, \quad (2.7)$$

322 which form a non Abelian group obeying the commutation relation $[T^a, T^b] \equiv$
 323 $if^{abc}T^c \neq 0$. The gauge fields that accompany this group are represented by $\hat{W}_\mu =$
 324 $(\hat{W}_\mu^1, \hat{W}_\mu^2, \hat{W}_\mu^3)$ and act only on the left handed component of the fermion field ψ_L .

325 One additional generator Y which represents the hypercharge of the particle under
 326 consideration is introduced through the $U(1)_Y$ group acting on both components of the
 327 fermion field, with an associated vector boson field \hat{B}_μ .

328 The $SU(2)_L \times U(1)_Y$ transformations of the left and right handed components of ψ
 329 are summarised by,

$$\begin{aligned}\chi_L &\rightarrow \chi'_L = e^{i\theta(x) \cdot T + i\theta(x)Y} \chi_L, \\ \psi_R &\rightarrow \psi'_R = e^{i\theta(x)Y} \psi_R,\end{aligned}\tag{2.8}$$

330 where the left handed fermions form isospin doubles χ_L and the right handed fermions
 331 are isosinglets ψ_R . For the first generation of leptons and quarks this represents

$$\begin{aligned}\chi_L &= \begin{pmatrix} \nu_e \\ e \end{pmatrix}_L, & \begin{pmatrix} u \\ d \end{pmatrix}_L \\ \psi_R &= e_R, & u_R, d_R\end{aligned}\tag{2.9}$$

332 Imposing local gauge invariance within \mathcal{L}_{EWK} is once again achieved by modifying
 333 the covariant derivative

$$D_\mu = \partial_\mu - \frac{ig}{2}\tau^i W_\mu^i - \frac{ig'}{2}Y B_\mu,\tag{2.10}$$

334 where g and g' are the coupling constant of the $SU(2)_L$ and $U(1)_Y$ groups respectively.
 335 Taking the example of the first generation of fermions defined in Equation.(2.9), with input
 336 hypercharge values of -1 and -2 for χ_L and e_R respectively, would lead to a Lagrangian
 337 \mathcal{L}_1 of the form,

$$\begin{aligned}\mathcal{L}_1 = &\bar{\chi}_L \gamma^\mu [i\partial_\mu - g \frac{1}{2}\tau \cdot W_\mu - g'(-\frac{1}{2})B_\mu] \chi_L \\ &+ \bar{e}_R \gamma^\mu [i\partial_\mu - g'(-1)B_\mu] e_R - \frac{1}{4}W_{\mu\nu} \cdot W^{\mu\nu} - \frac{1}{4}B_{\mu\nu} B^{\mu\nu}.\end{aligned}\tag{2.11}$$

³³⁸ As in **QED**, these additional gauge fields introduce field strength tensors $B_{\mu\nu}$ and
³³⁹ $W_{\mu\nu}$,

$$\hat{B}_{\mu\nu} = \partial_\mu \hat{B}_\nu - \partial_\nu \hat{B}_\mu \quad (2.12)$$

$$\hat{W}_{\mu\nu} = \partial_\mu \hat{W}_\nu - \partial_\nu \hat{W}_\mu - g \hat{W}_\mu \times \hat{W}_\nu \quad (2.13)$$

³⁴⁰ corresponding to the kinetic energy and self coupling of the W_μ fields and the kinetic
³⁴¹ energy term of the B_μ field.

³⁴² None of these gauge bosons are physical particles, and instead linear combinations of
³⁴³ these gauge bosons make up γ and the W and Z bosons, defined as

$$W^\pm = \frac{1}{\sqrt{2}} (W_\mu^1 \mp i W_\mu^2) \quad \begin{pmatrix} Z_\mu \\ A_\mu \end{pmatrix} = \begin{pmatrix} \cos\theta_W & -\sin\theta_W \\ \sin\theta_W & \cos\theta_W \end{pmatrix} \begin{pmatrix} W_\mu^3 \\ B_\mu \end{pmatrix} \quad (2.14)$$

³⁴⁴ where the mixing angle, $\theta_w = \tan^{-1} \frac{g'}{g}$, relates the coupling of the neutral weak and
³⁴⁵ electromagnetic interactions.

³⁴⁶ As in the case of the formulation of the **QED** Lagrangian there remains no mass term
³⁴⁷ for the photon. However this is also the case for the W, Z and fermions in the Lagrangian,
³⁴⁸ contrary to experimental measurement. Any explicit introduction of mass terms would
³⁴⁹ break the symmetry of the Lagrangian and instead mass terms can be introduced through
³⁵⁰ spontaneous breaking of the **EWK** symmetry via the Higgs mechanism.

³⁵¹ The Higgs mechanism induces spontaneous symmetry breaking through the introduc-
³⁵² tion of a complex scalar SU(2) doublet field ϕ which attains a non-zero Vacuum
³⁵³ Expectation Value (**VEV**) [17][18][19][20].

$$\phi = \begin{pmatrix} \phi^+ \\ \phi^0 \end{pmatrix} \quad \text{with} \quad \begin{aligned} \phi^+ &\equiv (\phi_1 + i\phi_2)/\sqrt{2} \\ \phi^0 &\equiv (\phi_3 + i\phi_4)/\sqrt{2} \end{aligned} \quad (2.15)$$

354 The Lagrangian defined in Equation (2.11) attains an additional term \mathcal{L}_{Higgs} of the
355 form

$$\mathcal{L}_{Higgs} = \overbrace{(D_\mu \phi)^\dagger (D^\mu \phi)}^{\text{kinetic}} - \overbrace{\mu^2 \phi^\dagger \phi - \lambda (\phi^\dagger \phi)^2}^{\text{potential } V(\phi)} \quad (\mu^2, \lambda) > 0 \in \mathbb{R},$$

$$\mathcal{L}_{SM} = \mathcal{L}_{EWK} + \mathcal{L}_{Higgs}, \quad (2.16)$$

356 where the covariant derivative D_μ is that defined in Equation (2.10). The last two
357 terms of \mathcal{L}_{Higgs} correspond to the Higgs potential, in which positive real positive values
358 of μ^2 and λ are required to ensure the generation of masses for the bosons and leptons.
359 The minimum of this potential is found at $\phi^\dagger \phi = \frac{1}{2}(\phi_1^2 + \phi_2^2 + \phi_3^2 + \phi_4^2) = \mu^2/\lambda = v^2$,
360 where v represents the **VEV**.

361 Defining the ground state of the ϕ field to be consistent with the $V(\phi)$ minimum, and
362 then expanding around a ground state chosen to maintain an unbroken electromagnetic
363 symmetry thus preserving a zero photon mass [21] leads to

$$\phi_0 = \sqrt{\frac{1}{2}} \begin{pmatrix} 0 \\ v \end{pmatrix}, \quad \phi(x) = e^{i\tau \cdot \theta(x)/v} \sqrt{\frac{1}{2}} \begin{pmatrix} 0 \\ v + h(x) \end{pmatrix}, \quad (2.17)$$

364 where the fluctuations from the vacuum ϕ_0 are parametrized in terms of four real
365 fields, $\theta_1, \theta_2, \theta_3$ and $h(x)$.

366 Choosing to gauge away the three massless Goldstone boson fields by setting $\theta(x)$ to
367 zero and substituting $\phi(x)$ back into kinetic term of \mathcal{L}_{Higgs} from Equation (2.16) leads to
368 mass terms for the W^\pm and Z bosons

$$(D_\mu \phi)^\dagger (D^\mu \phi) = \frac{1}{2}(\partial_\mu h)^2 + \frac{g^2 v^2}{2} W_\mu^+ W^{-\mu} + \frac{v^2 g^2}{8 \cos^2 \theta_w} Z_\mu Z^\mu + 0 A_\mu A^\mu, \quad (2.18)$$

369 where the relations between the physical and electroweak gauge fields from Equation
370 (2.14) are used. The W^\pm and Z bosons can then be determined to be

$$M_W = \frac{1}{2}gv \quad M_Z = \frac{1}{2} \frac{gv}{\cos \theta_w}. \quad (2.19)$$

371 This mechanism is also used to generate fermion masses by introducing a Yukawa
 372 coupling between the fermions and the ϕ field [22], with the coupling strength of a particle
 373 to the ϕ field governing its mass. Additionally a scalar boson h with mass $m_h = v\sqrt{\frac{\lambda}{2}}$, is
 374 also predicted as a result of this spontaneous symmetry breaking and became known as
 375 the Higgs boson. Its discovery by the CMS and ATLAS experiments in 2012 is concrete
 376 evidence to support this method of mass generation within the SM.

377 2.2. Motivation for Physics Beyond the Standard 378 Model

379 As has been described, the SM has proved to be a very successful theory, predicting the
 380 existence of the W^\pm and Z bosons and the top quark long before they were experimentally
 381 observed. However the theory does not accurately describe all observed phenomena and
 382 has some fundamental theoretical flaws that hint at the need for additional extensions to
 383 the current theory.

384 On a theoretical level, the SM is unable to incorporate the gravitational interactions
 385 of fundamental particles within the theory. Whilst at the electroweak energy scales the
 386 relative strength of gravity is negligible compared to the other three fundamental forces,
 387 at much higher energy scales $M_{planck} \sim 10^{18} GeV$ quantum gravitational effects become
 388 increasingly dominant. The failure to reconcile gravity within the SM, demonstrates that
 389 the SM must become invalid at some higher energy scale.

390 Some other deficiencies with the SM include the fact that the predicted rate of
 391 Charge-Parity violation does not account for the matter dominated universe which we
 392 inhabit, and the SM prediction of zero neutrino mass conflicts with the observation of
 393 neutrino flavour mixing, attributed to mixing between neutrino mass eigenstates [23][24].

394 Perhaps one of the most glaring gaps in the predictive power of the SM is that there
 395 exists no candidate to explain the cosmic dark matter observed in galactic structures
 396 through indirect techniques including gravitational lensing and measurement of the
 397 orbital velocity of stars in galactic edges. Any such candidate must be very weakly

398 interacting which must also be stable, owing to the lack of direct detection of the decay
399 products of such an process. Providing a dark matter candidate is of the prime goals
400 which be tackled by any Beyond Standard Model (**BSM**) physics model.

401 The recent discovery of the Higgs boson whilst a significant victory for the predictive
402 power of the **SM**, brings with it still unresolved questions. This issue is commonly
403 described as the “hierarchy problem”.

404 In the absence of new physics between the TeV and Planck scale, calculating beyond
405 tree-level contributions to the Higgs mass term given by its self interaction, result in
406 divergent terms that push the Higgs mass up to the planck mass M_{planck} .

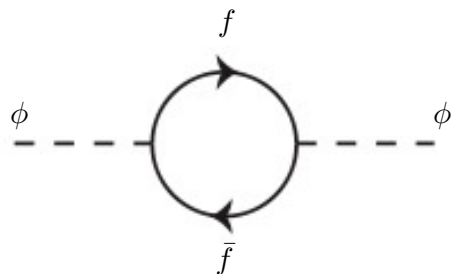


Figure 2.1.: One loop quantum corrections to the Higgs squared mass parameter m_h^2 due to a fermion.

407 This can be demonstrated by considering the one loop quantum correction to the
408 Higgs mass with a fermion f , shown in Figure 2.1 with mass m_f . The Higgs field couples
409 to f with a term in the Lagrangian $-\lambda_f h \bar{f} f$, yielding a correction of the form [25],

$$\delta m_h^2 = -\frac{|\lambda_f|^2}{8\pi^2} \Lambda^2 + \dots, \quad (2.20)$$

410 where λ_f represents the coupling strength for each type of fermion $\propto m_f$, and Λ the
411 cutoff energy scale at which the **SM** ceases to be a valid theory.

412 To recover the mass of the now discovered Higgs boson would require a fine-tuning of
413 the parameters to cancel out these mass corrections the the Higgs mass to the scale of
414 30 orders of magnitude. This appears as an unnatural solution to physicists and it is
415 this hierarchy problem that provides one of the strongest motivations for the theory of
416 SUperSYmmetry (**SUSY**).

⁴¹⁷ 2.3. Supersymmetry Overview

⁴¹⁸ Supersymmetry provides potential solutions to many of the issues raised in the previous
⁴¹⁹ section. It provides a dark matter candidate, can explain baryogenesis in the early
⁴²⁰ universe and also provides an elegant solution to the hierarchy problem [26][27][28][29].
⁴²¹ At its heart it represents a new space-time symmetry that relates fermions and bosons.
⁴²² This symmetry converts bosonic states into fermionic states, and vice versa, see Equation
⁴²³ (2.21) ,

$$Q|Boson\rangle = |Fermion\rangle \quad Q|Fermion\rangle = |Boson\rangle, \quad (2.21)$$

⁴²⁴ where the operator Q is the generator of these transformations. Quantum field theories
⁴²⁵ which are invariant under such transformations are called supersymmetric.

⁴²⁶ This symmetry operator therefore acts upon a particles spin altering it by a half integer
⁴²⁷ value. The consequences of the introduction of this additional space-time symmetry
⁴²⁸ introduce a new rich phenomenology. For example in supersymmetric theories, both
⁴²⁹ the left handed $SU(2)$ doublet and right handed singlet of fermions will have a spin-0
⁴³⁰ superpartner, containing the same electric charge, weak isospin, and colour as its **SM**
⁴³¹ partner. In the case of the leptons $(\nu_l, l)_L$ will have two superpartners, a sneutrino $\tilde{\nu}_l{}_L$
⁴³² and a slepton \tilde{l}_L , whilst the singlet l_R also has a superpartner slepton \tilde{l}_R .

⁴³³ Each particle in a supersymmetric theory is paired together with their superpartners
⁴³⁴ as a result of this supersymmetric transformations in a so called supermultiplet. These
⁴³⁵ superpartners will then consequently also contribute to the corrections to the Higgs mass.
⁴³⁶ Bosonic and fermionic loops contributing to the correction appear with opposite signs,
⁴³⁷ and therefore cancellation of these divergent terms will stabilise the Higgs mass, solving
⁴³⁸ the hierarchy problem [30][31].

⁴³⁹ One of the simplest forms of **SUSY** would predict a whole set of supersymmetric
⁴⁴⁰ partners to their **SM** counterparts with the same mass and interactions. However the
⁴⁴¹ currently lack of any experimental evidence for the predicted sparticle spectrum implies
⁴⁴² **SUSY** must be a broken symmetry in which any sparticle masses must be greater than
⁴⁴³ their SM counterparts.

⁴⁴⁴ There exist many techniques which can induce supersymmetric breaking [32][33][34].
⁴⁴⁵ Of particular interest to experimental physicists are those at which the breaking scale

⁴⁴⁶ is of an order that is experimentally accessible to the LHC i.e. \sim TeV scale. Whilst
⁴⁴⁷ there is no requirement for supersymmetric breaking to occur at this energy scale, for
⁴⁴⁸ supersymmetry to provide a solution to the hierarchy problem, it is necessary for this
⁴⁴⁹ scale to not differ too drastically from the EWK scale [35][36].

⁴⁵⁰ 2.3.1. R-Parity

⁴⁵¹ Some supersymmetric theories also present a solution to the dark matter problem. Such
⁴⁵² theories can contain a Lightest Supersymmetric Partner (LSP), which matches the criteria
⁴⁵³ of a Weakly Interacting Massive Particle (WIMP) required by cosmological observation
⁴⁵⁴ if R-parity is conserved.

⁴⁵⁵ Baryon (B) and Lepton (L) number conservation is forbidden in the SM by renor-
⁴⁵⁶ malisability requirements. The violation of Baryon or Lepton number would result in
⁴⁵⁷ the proton lifetime much shorter than those set by experimental limits [37]. Another
⁴⁵⁸ symmetry called R-parity is then often introduced to SUSY theories to maintain baryon
⁴⁵⁹ and lepton conservation.

⁴⁶⁰ R-parity is described by the equation

$$R_P = (-1)^{3(B-L)+2s}, \quad (2.22)$$

⁴⁶¹ where s represents the spin of the particles. $B = \pm \frac{1}{3}$ for quarks/antiquarks and $B = 0$
⁴⁶² for all others, $L = \pm 1$ for leptons/antileptons, $L = 0$ for all others.

⁴⁶³ R-parity ensures the stability of the proton in SUSY models, and also has other
⁴⁶⁴ consequences for the production and decay of supersymmetric particles. At particle
⁴⁶⁵ colliders supersymmetric particles can only be pair produced, and similarly the decay
⁴⁶⁶ of any produced supersymmetric particle is restricted to a SM particle and a lighter
⁴⁶⁷ supersymmetric particle as allowed by conservation laws. A further implication of R-
⁴⁶⁸ parity is that once a supersymmetric particle has decayed to the LSP it remains stable,
⁴⁶⁹ unable to decay into a SM particle.

⁴⁷⁰ A LSP would not interact in a detector at a particle collider, leaving behind a missing
⁴⁷¹ energy \cancel{E}_T signature. The assumption of R-parity and its consequences are used to
⁴⁷² determine the physical motivation and search strategies for SUSY model at the LHC.

473 2.4. Experimental signatures of SUSY at the LHC

474 Should strongly interacting sparticles be within the experimental reach of the LHC, then
475 it is expected that they can be produced in a variety of ways.

- 476 • squark/anti-squark and gluino pairs can be produced via both gluon fusion and
477 quark/anti-quark scattering.
- 478 • a gluino and squark produced together via quark-gluon scattering
- 479 • squark pairs produced via quark-quark scattering

480 Whilst most SUSY searches invoke the requirement of R-parity to explore parameter
481 phase space, there still exist a whole plethora of possible SUSY model topologies which
482 could be discovered at the LHC.

483 During the 2011 run period at a $\sqrt{s} = 7$ TeV particular models were used to benchmark
484 performance and experimental reach of both CMS searches and previous experiments.
485 The Compressed Minimal SuperSymmetric Model (CMSSM) was initially chosen for a
486 number of reasons [38]. One of the most compelling being the reduction from the up to
487 105 new parameters introduced by SUSY in addition to the existing 19 of the SM to that
488 of just 5 free extra free parameters. It was this simplicity, combined with the theory not
489 requiring any fine tuning of particle masses to produce the experimentally verified SM
490 that made it an attractive model to interpret physics results.

491 However recent results from the LHC now strongly disfavour large swathes of CMSSM
492 parameter space [39][40][41]. In the face of such results a more pragmatic model indepen-
493 dent search strategy is now applied across most SUSY searches at the LHC, see Section
494 (2.4.1).

495 As previously stated, a stable LSP that exhibits the properties of a dark matter would
496 be weakly interacting and therefore will not be directly detected in a detector environment.
497 Additionally the cascade decays of supersymmetric particles to the LSP would also result
498 in significant hadronic activity. These signatures can then be characterised through
499 large amounts of hadronic jets (see Section (3.3.1)), leptons and a significant amount of
500 missing energy dependent upon the size of the mass splitting between the LSP and the
501 supersymmetric particle it has decayed from.

502 Whilst the SM contains processes which can exhibit a similar event topology to that
503 described above. The largest contribution of which comes in from the general QCD

environment of a hadron collider. A multitude of different analytical techniques are used by experimental physicists to reduce or estimate any reducible or irreducible backgrounds, allowing a possible **SUSY** signature to be extracted. The techniques employed within this thesis are described in great detail within Section (4.1).

2.4.1. Simplified Models

With such a variety of different ways for a **SUSY** signal to manifest itself, it is necessary to be able to interpret experimental reach through the masses of gluinos and squarks which can excluded by experimental searches rather than on a model specific basis.

This is accomplished through **SMS** models, which are defined by a set of hypothetical particles and a sequence of their production and decay [42][43]. In the **SMS** models considered within this thesis, only the production process for the two primary particles are considered. Each primary particle can undergo a direct or a cascade decay through an intermediate new particle. At the end of each decay chain there remains a neutral, undetected **LSP** particle, denoted $\tilde{\chi}_{LSP}$ which can represent a neutralino or gravitino. Essentially it is easier to consider each **SMS** with branching ratios set to 100% The masses of the primary particle and the **LSP** remain as free parameters, in which the absolute value and relative difference between the primary and **LSP** particle alter the kinematics of the event.

Different **SMS** models are denoted with a T-prefix, with a summary of the types interpreted within this thesis listed below [44].

- **T1,T1xxxx**, models represent a simplified version of gluino pair production with each gluino (superpartner to the gluon) undergoing a three-body decay to a quark-antiquark pair and the **LSP** (i.e. $\tilde{g} \rightarrow q\bar{q}\tilde{\chi}_{LSP}$). The resultant final state from this decay is typically 4 jets + \cancel{E}_T in the absence of initial/final state radiation and detector effects. xxxx denotes models in which the quarks are of a specific flavour, typically t or b quark-antiquarks.
- **T2,T2xx**, models represent a simplified version of squark anti-squark production with each squark undergoing a two-body decay into a light-flavour quark and **LSP** (i.e. $\tilde{q} \rightarrow q\tilde{\chi}_{LSP}$). This results in final states with less jets than gluino mediated production, typically 2 jets + \cancel{E}_T when again ignoring the effect of initial/final state radiation and detector effects. xx models again represent decays in which both the quark and the squark within the decay is of a specific flavour, typically \tilde{t}/t or \tilde{b}/b .

Models rich in b and t quarks are interpreted within this thesis as they remain of particular interest within “Natural SUSY” scenarios [45][46]. The largest contribution to the quadratic divergence in the Higgs mass parameter comes from a loop of top quarks via the Yukawa coupling. Cancellation of these divergences can be achieved in supersymmetric theories by requiring a light right handed top squark, \tilde{t}_R , and left-handed double $SU(2)_L$ doublet containing top and bottom squarks, $(\tilde{\frac{t}{b}})_L$ [47].

These theories therefore solve the hierarchy problem by predicting light \sim EWK scale third generation sleptons, to be accessible at the LHC. Search strategies involving the requirement of b-tagging (see Section (3.3.2)) are used to give sensitivity to these type of SUSY scenarios and are discussed in greater detail within Chapter 5.

Two example decay chains are shown in Figure 2.2; the pair production of gluinos (T1) and the pair production of squarks (T2) decaying into SM particles and LSP’s.

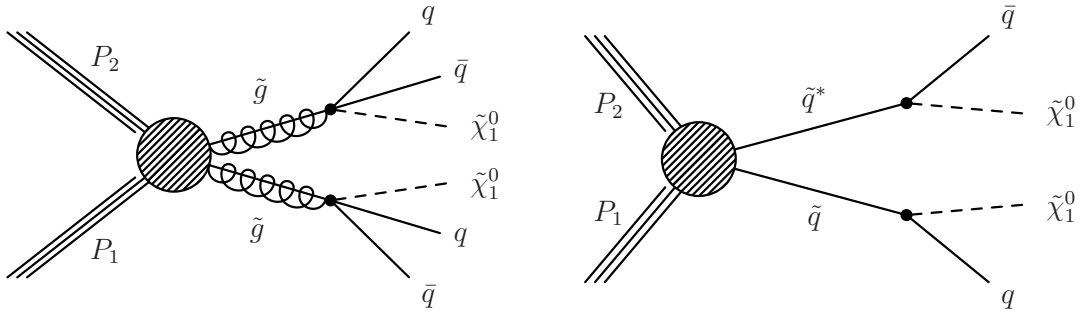


Figure 2.2.: Two example SMS model decays (T1 (left), T2 (right)), which are used in interpretations of physics reach by CMS.

Chapter 3.

⁵⁴⁸ The LHC and the CMS Detector

⁵⁴⁹ Probing the SM for signs of new physics would not be possible without the immensely
⁵⁵⁰ complex electronics and machinery that makes the TeV energy scale accessible for the
⁵⁵¹ first time. This chapter will cover the LHC based at European Organization for Nuclear
⁵⁵² Research (CERN) and the Compact Muon Solenoid (CMS) detector, being the experiment
⁵⁵³ the author is a member of. Section (3.2) serves to introduce an overview of the different
⁵⁵⁴ components of the CMS detector, with more detail spent on those that are relevant in
⁵⁵⁵ the search for Supersymmetric particles. Section (3.3) will focus on event and object
⁵⁵⁶ reconstruction again with more emphasis on jet level quantities which are most relevant
⁵⁵⁷ to the author's analysis research. Finally Section (3.4) will cover work performed by
⁵⁵⁸ the author, as service to the CMS Collaboration, in measuring the performance of the
⁵⁵⁹ Global Calorimeter Trigger (GCT) component of the L1 trigger during the 2012-2013
⁵⁶⁰ run period.

⁵⁶¹ 3.1. The LHC

⁵⁶² The LHC is a storage ring, accelerator, and collider of circulating beams of protons or
⁵⁶³ ions. Housed in the tunnel dug for the Large Electron-Positron collider (LEP), it is
⁵⁶⁴ approximately 27 km in circumference, 100 m underground, and straddles the border
⁵⁶⁵ between France and Switzerland outside of Geneva. It is currently the only collider
⁵⁶⁶ in operation that is able to study physics at the TeV scale. A double-ring circular
⁵⁶⁷ synchrotron, it was designed to collide both proton-proton (pp) and heavy ion (PbPb)
⁵⁶⁸ with a centre of mass energy $\sqrt{s} = 14$ TeV at a final design luminosity of $10^{34}\text{cm}^{-2}\text{s}^{-1}$.

⁵⁶⁹

These counter-circulating beams of protons/Pb ions are merged in four sections around the ring to enable collisions of the beams, with each interaction point being home to one of the four major experiments; A Large Ion Collider Experiment (**ALICE**) [48], A Toroidal LHC ApparatuS (**ATLAS**) [49], Compact Muon Solenoid (**CMS**) [50] and Large Hadron Collider Beauty (**LHC-B**) [51] which record the resultant collisions. The layout of the **LHC** ring is shown in Figure 3.1. The remaining four sections contain acceleration, collimation and beam dump systems. In the eight arc sections, the beams are steered by magnetic fields of up to 8 T provided by super conduction dipole magnets, which are maintained at temperatures of 2 K using superfluid helium. Additional magnets for focusing and corrections are also present in straight sections within the arcs and near the interaction regions where the detectors are situated.

581

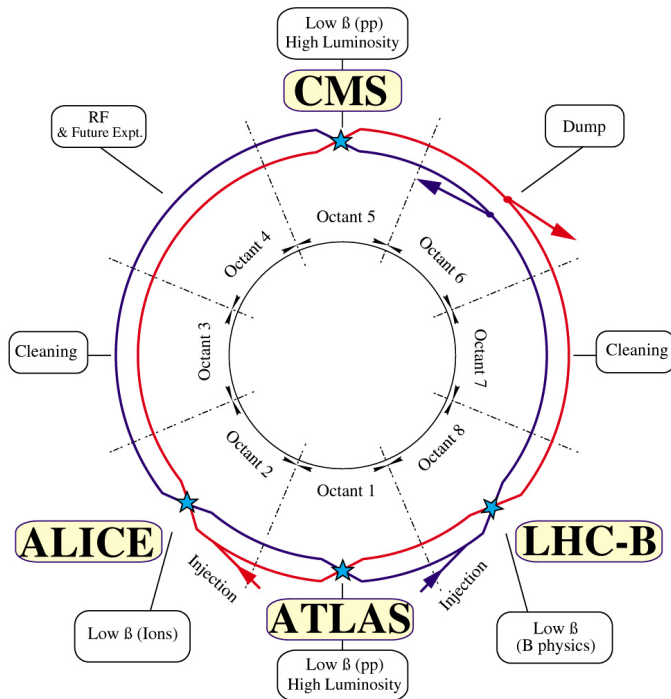


Figure 3.1.: A top down layout of the LHC. [52], with the position of the four main detectors labelled.

Proton beams are formed inside the Proton Synchrotron (**PS**) from bunches of protons 50 ns apart with an energy of 26 GeV. The protons are then accelerated in the Super Proton Synchrotron (**SPS**) to 450 GeV before being injected into the **LHC**. These **LHC** proton beams consists of many “bunches” i.e. approximately 1.1×10^{11} protons localized into less than 1 ns in the direction of motion. Before collision the beams are ramped to 4

587 TeV (2012) per beam in a process involving increasing the current passing through the
 588 dipole magnets. Once the desired \sqrt{s} energy is reached then the beams are allowed to
 589 collide at the interaction points. The luminosity falls regularly as the run progresses as
 590 protons are lost in collisions, and eventually the beam is dumped before repeating the
 591 process again.

592

593 Colliding the beams produced an instantaneous luminosity of approximately $5 \times$
 594 $10^{33} \text{ cm}^{-2}\text{s}^{-1}$ during the 2012 run. The high number of protons in each bunch increases
 595 the likelihood of multiple interactions with each crossing of the counter-circulating
 596 beams. This leads to isotropic energy depositions within the detectors positioned at these
 597 interaction points, increasing the energy scale of the underlying event. This is known as
 598 pile-up and the counteracting of it's effects are important to the many measurements
 599 performed at the LHC.

600 In the early phase of prolonged operation after the initial shutdown the machine
 601 operated in 2010-2011 at 3.5 TeV per beam, $\sqrt{s} = 7 \text{ TeV}$, delivering 6.13 fb^{-1} of data
 602 [53]. During the 2012-2013 run period, data was collected at an increased $\sqrt{s} = 8 \text{ TeV}$
 603 improving the sensitivity of searches for new physics. Over the whole run period 23.3
 604 fb^{-1} of data was delivered of which 21.8 fb^{-1} was recorded by the CMS detector as shown
 605 in Figure 3.2 [53]. A total of 12 fb^{-1} of 8 TeV certified data was collected by October
 606 2012, and it is this data which forms the basis of the results discussed within this thesis.

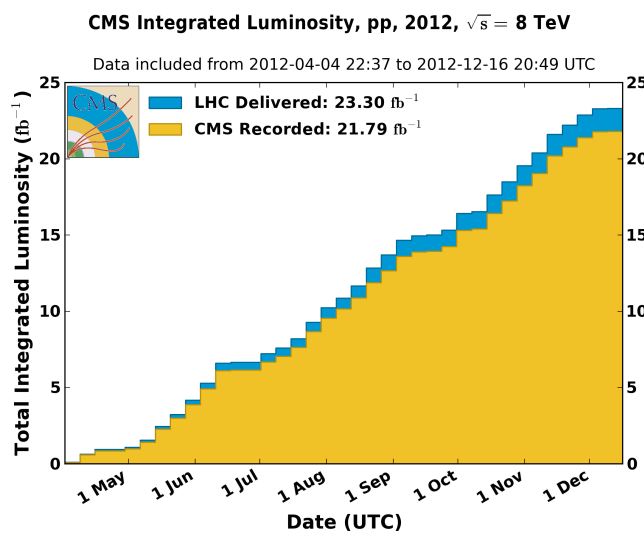


Figure 3.2.: The total integrated luminosity delivered to and collected by CMS during the 2012 8 TeV pp runs.

607 3.2. The CMS detector

608 The Compact Muon Solenoid (**CMS**) detector is one of two general purpose detectors
 609 at the **LHC** designed to search for new physics. The detector is designed to provide
 610 efficient identification and measurement of many physics objects including photons,
 611 electrons, muons, taus, and hadronic showers over wide ranges of transverse momentum
 612 and direction. Its nearly 4π coverage in solid angle allows for accurate measurement of
 613 global transverse momentum imbalance. These design factors give **CMS** the ability to
 614 search for direct production of **SUSY** particles at the TeV scale, making the search for
 615 Supersymmetric particles one of the highest priorities among the wide range of physics
 616 programmes at **CMS**.

617

618 **CMS** uses a right-handed Cartesian coordinate system with the origin at the interaction
 619 point and the z-axis pointing along the beam axis, the x-axis points radially inwards to
 620 the centre of the collider ring, with the y-axis points vertically upward. The azimuthal
 621 angle, ϕ ranging between $[-\pi, \pi]$ is defined in the x-y plane starting from the x-axis. The
 622 polar angle θ is measured from the z axis. The common convention in particle physics is
 623 to express an out going particle in terms of ϕ and its pseudorapidity defined as

$$\eta = -\log \tan \left(\frac{\theta}{2} \right). \quad (3.1)$$

624 The variable $\Delta R = \sqrt{\Delta\phi^2 + \Delta\eta^2}$ is commonly used to define angular distance
 625 between objects within the detector and additionally energy and momentum is typically
 626 measured in the transverse plane perpendicular to the beam line. These values are
 627 calculated from the x and y components of the object and are denoted as $E_T = E \sin \theta$
 628 and $p_T = \sqrt{p_x^2 + p_y^2}$.

629 3.2.1. Detector Subsystems

630 As the range of particles produced in pp collisions interact in different ways with mat-
 631 ter, **CMS** is divided into subdetector systems, which perform complementary roles to
 632 identify the identity, mass and momentum of the different physics objects present in
 633 each event. These detector sub-systems contained inside **CMS** are wrapped in layers

around a central 13 m long 4 T super conducting solenoid as shown in Figure 3.3. With the endcaps closed , CMS is a cylinder of length 22 m, diameter 15 m, and mass 12.5 kilotons. A more detailed complete description of the detector can be found elsewhere [50].

637

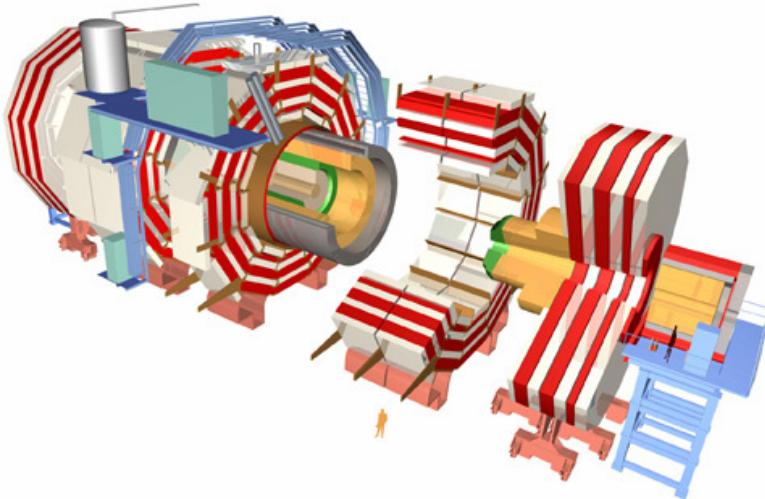


Figure 3.3.: A pictorial depiction of the CMS detector with the main detector subsystems labelled. [54]

638 3.2.2. Tracker

The inner-most subdetector of the barrel is the multi-layer silicon tracker, formed of a pixel detector component encased by layers of silicon strip detectors. The pixel detector consists of three layers of silicon pixel sensors providing measurements of the momentum, position coordinates of the charged particles as they pass, and the location of primary and secondary vertices between 4cm and 10cm transverse to the beam. Outside the pixel detector, ten cylindrical layers of silicon strip detectors extend the tracking system out to a radius of 1.20m from the beam line. The tracking system provides efficient and precise determination of the charges, momenta, and impact parameters of charged particles with the geometry of the tracker extending to cover a rapidity range up to $|\eta| < 2.5$.

648

The tracking system also plays a crucial part in the identification of jets originating from b-quarks through measurement of displaced secondary vertices, which is covered in more detail in Section (3.3.2). The identification of b-jets is important in many searches

for natural SUSY models and forms an important part of the inclusive search strategy described within Section (4.2).

3.2.3. Electromagnetic Calorimeter

Immediately outside of the tracker, but still within the magnet core, sits the Electromagnetic CALorimeter (**ECAL**). Covering a pseudorapidity up to $|\eta| < 3$ and comprising of over 75,000 PbWO₄ (lead tungstate) crystals that scintillate as particles deposit energy, the **ECAL** provides high resolution measurements of the electromagnetic showers from photons, electrons in the detector.

660

Lead tungstate is used because of its short radiation length ($X_0 \sim 0.9\text{cm}$) and small Molieré radius ($\sim 2.1\text{cm}$) leading to high granularity and resolution. It's fast scintillation time ($\sim 25\text{ns}$) reduces the effects of pile-up due to energy from previous collisions still being read out, and its radiation hardness gives it longevity. The crystals are arranged in modules which surround the beam line in a non-projective geometry, angled at 3° with respect to the interaction point to minimise the risk of particles escaping down the cracks between the crystals.

668

The **ECAL** is primarily composed of two sections, the Electromagnetic CALorimeter Barrel (**EB**) which extends in pseudo-rapidity to $|\eta| < 1.479$ with a crystal front cross section of $22 \times 22\text{ mm}^2$ and a length of 230 mm corresponding to 25.8 radiation lengths, and the Electromagnetic CALorimeter Endcap (**EE**) covering a rapidity range of $1.479 < |\eta| < 3.0$, which consists of two identical detectors on either side of the **EB**. A lead-silicon sampling ‘pre-shower’ detector Electromagnetic CALorimeter pre-Shower (**ES**) is placed before the endcaps to aid in the identification of neutral pions. Their arrangement are shown in Figure 3.4.

677

Scintillation photons from the lead tungstate crystals are instrumented with Avalanche Photo-Diodes (**APD**) and Vacuum Photo-Triodes (**VPT**) located in the **EB** and **EE** respectively, converting the scintillating light into an electric signal which is consequently used to determine the amount of energy deposited within the crystal . These instruments are chosen for their resistance under operation to the strong magnetic field of **CMS**. The scintillation of the **ECAL** crystals as well as the response of the **APDs** varies as a function

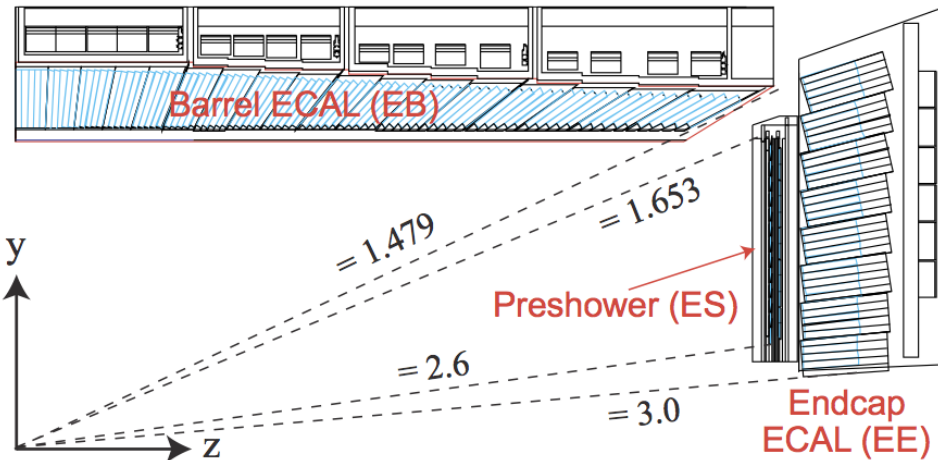


Figure 3.4.: Illustration of the CMS ECAL showing the arrangement of the lead tungstate crystals in the EB and EE. The ES is also shown and is located in front of the EE [55].

684 of temperature and so cooling systems continually maintain an overall constant ECAL
685 temperature $\pm 0.05^\circ C$.

686 3.2.4. Hadronic Calorimeter

687 Beyond the ECAL lies the Hadronic CALorimeter (HCAL) which is responsible for
688 the accurate measurement of hadronic showers, crucial for analyses involving jets or
689 missing energy signatures. The HCAL is a sampling calorimeter which consists of al-
690 ternating layers of brass absorber and plastic scintillator, except in the hadron forward
691 ($3.0 < |\eta| < 5.0$) region in which steel absorbers and quartz fibre scintillators are used
692 because of their increased radiation tolerance. Hadron showers are initiated in the
693 absorber layers inducing scintillation in the plastic scintillator tiles. These scintillation
694 photons are converted by wavelength shifting fibres for read-out by hybrid photodiodes.
695

696 The HCAL's size is constrained to a compact size by the presence of the solenoid,
697 requiring the placement of an additional outer calorimeter on the outside of the solenoid
698 to increase the sampling depth of the HCAL. A schematic of the HCAL can be seen in
699 Figure 3.5.

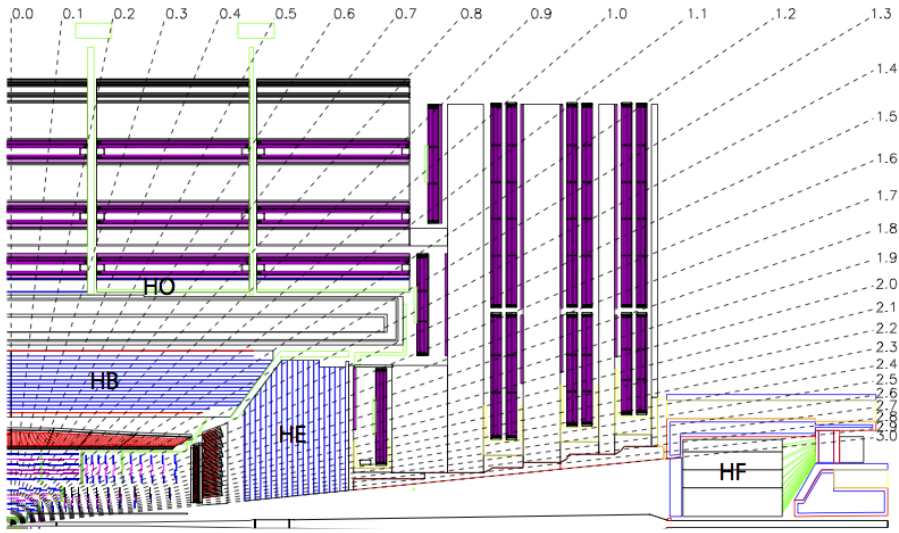


Figure 3.5.: Schematic of the hadron calorimeters in the r-z plane, showing the locations of the **HCAL** components and the **HF**. [50].

701 The **HCAL** covers the range $|\eta| < 5$ and consists of four subdetectors: the Hadron
 702 Barrel (**HB**) $|\eta| < 1.3$, the Hadron Outer (**HO**), the Hadron Endcaps (**HE**) $1.3 < |\eta| < 3.0$
 703 and the Hadron Forward (**HF**). The **HB** is contained between the outer edge of the **ECAL**
 704 and the inner edge of the solenoid, formed of 36 azimuthal wedges it is split between
 705 two half-barrel segments. Each wedge is segmented into four azimuthal angle (ϕ) sectors,
 706 and each half-barrel is further segmented into 16 η towers. The electronic readout chain,
 707 channels the light from the active scintillator layers from one ϕ -segment and all η -towers
 708 of a half-barrel to a Hybrid Photo Diode (**HPD**).

709 The relatively short number of interaction lengths (λ_l , the distance a hadron will
 710 travel through the absorber material before it has lost $\frac{1}{e}$ of its energy) within the **HB**,
 711 the lowest being $\lambda_l = 5.82$ for $|\eta| = 0$, facilitates the need for the ‘tail catching’ **HO**
 712 to increase the sampling depth in the central barrel rapidity region $|\eta| < 1.3$ to 11
 713 interaction lengths . Significant fractions of the hadrons energy will be deposited in the
 714 **ECAL** as it passed through the detector. Therefore measurements of hadron energies
 715 in the central regions $|\eta| < 3.0$ use both the **ECAL** and **HCAL** to reconstruct the true
 716 energy from showering hadrons.

717 **3.2.5. Muon Systems**

718 Muons being too massive to radiate away energy via Bremsstrahlung, interact little in
719 the calorimeters and mostly pass through the detector until they reach the system of
720 muon detectors which forms the outer most part of the **CMS** detector.

721 Outside of the superconducting solenoid are four muon detection layers interleaved
722 with the iron return yokes which measure the muons energy via ionisation of gas within
723 detector elements. Three types of gaseous chamber are used. The Drift Tube (**DT**),
724 Cathode Stripe Chamber (**CSC**), and Resistive Plate Chamber (**RPC**) systems provide
725 efficient detection of muons with pseudo-rapidity $|\eta| < 2.4$. The best reconstruction
726 performance is obtained when the muon chamber is combined with the inner tracking
727 information to determine muon trajectories and their momenta [56].

728

729 **3.3. Event Reconstruction and Object Definition**

730 The goal of event reconstruction is to take the raw information recorded by the detector
731 and to compute from it higher-level quantities which can be used at an analysis level.
732 These typically correspond to an individual particle’s energy and momenta, or groups of
733 particles which shower in a narrow cone and the overall global energy and momentum
734 balance of the event. The reconstruction of these objects are described in great detail in
735 [57], however covered below are brief descriptions of those which are most relevant to the
736 analysis detailed in Chapter 4.

737 **3.3.1. Jets**

738 Quarks and gluons are produced copiously at the LHC in the hard scattering of partons.
739 As these quarks and gluons fragment, they hadronise and decay into a group of strongly
740 interactive particles and their decay products. These streams of particles travel in the
741 same direction, as they have been “boosted” by the momentum of the primary hadron.
742 These collections of decay products are reconstructed and identified together as a “jet”.

743 At **CMS** jets are reconstructed from energy deposits in the detector using the anti-kt
744 algorithm [58] with size parameter $\Delta R = 0.5$. The anti-kt jet algorithm clusters jets by
745 defining a distance between hard (high p_T) and soft (low p_T) particles such that soft

746 particles are preferentially clustered with hard particles before being clustered between
747 themselves. This produces jets which are robust to soft particle radiation from the pile-up
748 conditions experienced at the **LHC**.

749

750 There are two main type of jet reconstruction used at **CMS**, Calorimeter (Calo) and
751 Particle Flow (PF) jets [59]. Calorimeter jets are reconstructed using both the **ECAL**
752 and **HCAL** cells, combined into calorimeter towers . These calorimeter towers consist of
753 geometrically matched **HCAL** cells and **ECAL** crystals. Electronics noise is suppressed by
754 applying a threshold to the calorimeter cells, with pile-up effects reduced by a requirement
755 placed on the tower energy [60]. Calorimter jets are the jets used within the analyses
756 described in this thesis.

757 PF jets are formed from combining information from all of the **CMS** subdetectors
758 systems to determine which final state particles are present in the event. Generally,
759 any particle is expected to produce some combination of a track in the silicon tracker,
760 a deposit in the calorimeters, or a track in the muon system. The PF jet momentum
761 and spatial resolutions are greatly improved with respect to calorimeter jets, as the use
762 of the tracking detectors and of the high granularity of **ECAL** allows resolution and
763 measurement of charged hadrons and photons inside a jet, which together constitute \sim
764 85% of the jet energy [61].

765 The jets reconstructed by the clustering algorithm in **CMS** typically have an energy
766 that differs to the ‘true’ energy measured by a perfect detector. This stems from the
767 non-linear and nonuniform response of the calorimeters as well as other residual effects
768 including pile-up and underlying events, and therefore additional corrections are applied
769 to recover a uniform relative response as a function of pseudo-rapidity. These are applied
770 as separate sub corrections [62].

- 771 • A PU correction is first applied to the jet. It subtracts the average extra energy
772 deposited in the jet that comes from other vertices present in the event and is
773 therefore not part of the hard jet itself.
- 774 • p_T and η dependant corrections derived from Monte Carlo simulations are used to
775 account for the non-uniform response of the detector.
- 776 • p_T and η residual corrections are applied to data only to correct for difference
777 between data and Monte Carlo. The residual is derived from QCD dijet samples
778 and the p_T residual from $\gamma+$ jet and $Z+$ jets samples in data.

⁷⁷⁹ **3.3.2. B-tagging**

⁷⁸⁰ The decays of b quarks are suppressed by small CKM matrix elements. As a result, the
⁷⁸¹ lifetimes of b-flavoured hadrons, produced in the fragmentation of b quarks, are relatively
⁷⁸² long; \mathcal{O} 1ps. The identification of jets origination from b quarks is very important for
⁷⁸³ searches for new physics and for measurements of standard model processes.

⁷⁸⁴

⁷⁸⁵ Many different algorithms developed by CMS select b-quark jets based on variables
⁷⁸⁶ such as the impact parameters of the charged-particle tracks, the properties of recon-
⁷⁸⁷ structed decay vertices, and the presence or absence of a lepton, or combinations thereof
⁷⁸⁸ [63]. One of the most efficient of which is the Combined Secondary Vertex (CSV) which
⁷⁸⁹ operates based on secondary vertex and track-based lifetime information, benchmarked
⁷⁹⁰ in ‘Loose’, ‘Medium’ and ‘Tight’ working points, of which the medium point is the tagger
⁷⁹¹ used within the α_T search detailed in Section (4.1).

⁷⁹² Using the CSV tagger, a likelihood-based discriminator distinguishes between jets
⁷⁹³ from b-quarks, and those from charm or light quarks and gluons, which is shown in Figure
⁷⁹⁴ 3.6. The minimum thresholds on the discriminator for each working point correspond to
⁷⁹⁵ the misidentification probability for light-parton jets of 10%, 1%, and 0.1%, respectively,
⁷⁹⁶ in jets with an average p_T of about 80 GeV.

⁷⁹⁷ The b-tagging performance is evaluated to measure the b-jet tagging efficiency ϵ_b ,
⁷⁹⁸ and the misidentification probability of charm ϵ_c and light-parton jets ϵ_s . The tagging
⁷⁹⁹ efficiencies for each of these three jet flavours are compared between data and MC
⁸⁰⁰ simulation, from which a series of p_T and $|\eta|$ binned jet corrections are determined,

$$SF_{b,c,s} = \frac{\epsilon_{b,c,s}^{data}}{\epsilon_{b,c,s}^{MC}}. \quad (3.2)$$

⁸⁰¹ These are collectively named ‘Btag Scale Factors’ and allow MC simulation to accu-
⁸⁰² rately reflect the running conditions and performance of the tagging algorithm in data.
⁸⁰³ Understanding of the b-tagging efficiency is essential in order to minimise systematic
⁸⁰⁴ uncertainties in physics analyses that employ b-tagging.

⁸⁰⁵

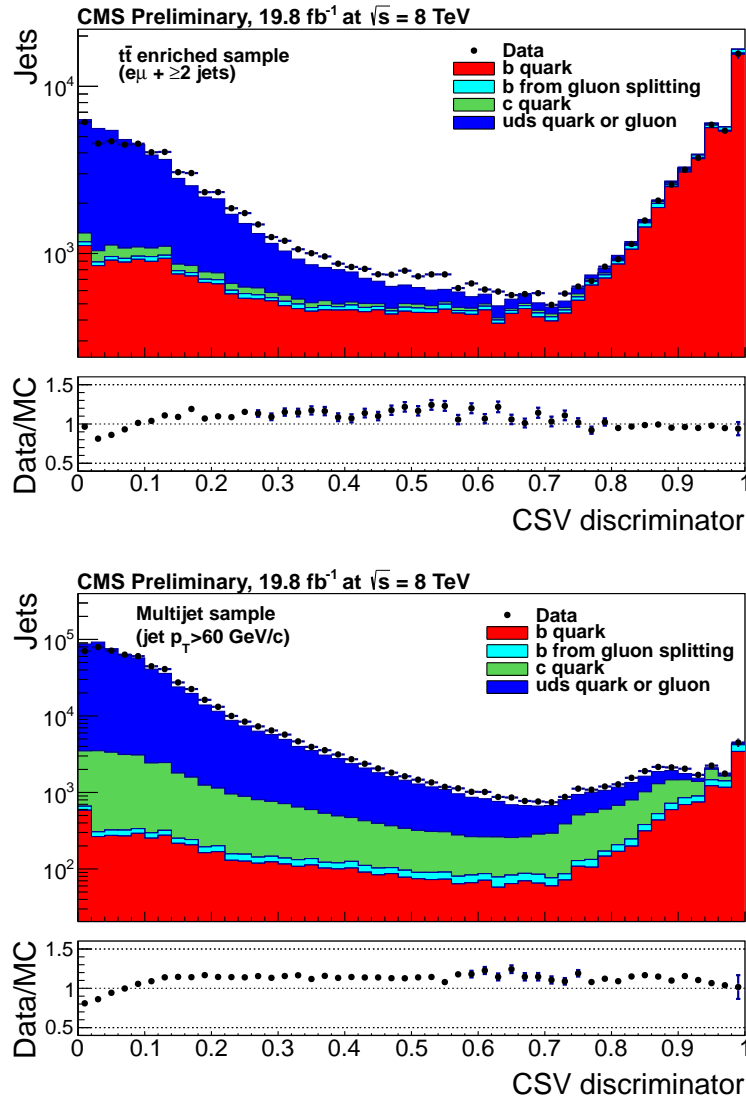


Figure 3.6.: CSV algorithm discriminator values in enriched $t\bar{t}$ (top) and inclusive multi-jet samples (bottom) for b,c and light flavoured jets [64]. Working points are determined from the misidentification probability for light-parton jets to be tagged as a b-jet and are given as 0.244, 0.679 and 0.898 for L,M and T working points respectively.

806 The b-tagging efficiency is measured in data using several methods applied to multi
 807 jet events, primarily based on a sample of jets enriched in heavy flavour content. One
 808 method requires the collection of events with a soft muon within a cone $\Delta R < 0.4$ around
 809 the jet axis. Because the semileptonic branching fraction of b hadrons is significantly
 810 larger than that for other hadrons, these jets are more likely to arise from b quarks than
 811 from another flavour, with the resultant momentum component of the muon transverse
 812 to the jet axis larger for muons from b-hadron decays than from light or charm jets.

813 Additionally the performance of the tagger can also be benchmarked in $t\bar{t}$ events where
 814 in the SM, the top quark is expected to decay to a W boson and a b quark about 99.8%
 815 of the time [1]. Further selection criteria is applied to these events to further enrich the
 816 b quark content of these events. The methods to identify b-jets in data are discussed
 817 in great detail at [65]. The jet flavours are determined in simulation using truth level
 818 information and are compared to data to determine the correction scale factors (SF_b),
 819 which are displayed for the CSVM tagger in Figure 3.7.

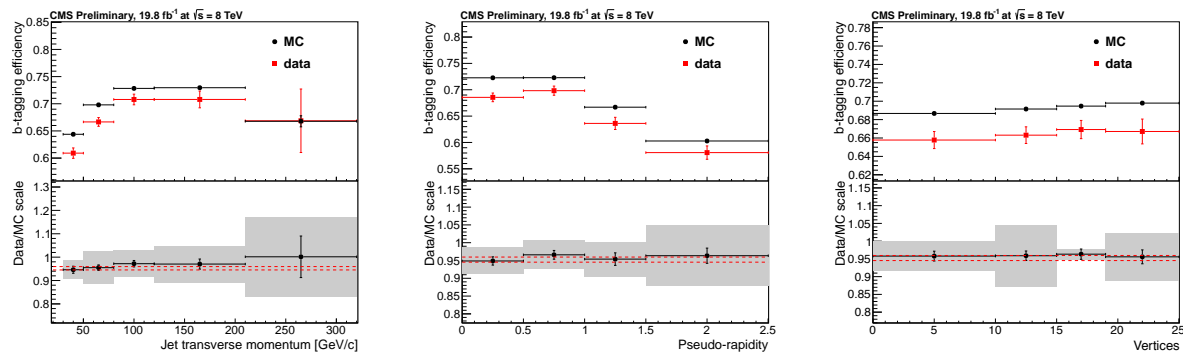


Figure 3.7.: Measured in $t\bar{t} \rightarrow$ di-lepton events using the CSVM tagger: (upper panels) b-tagging efficiencies and (lower panels) data/MC scale factor SF_b as a function of (left) jet p_T , (middle) jet $|\eta|$ and (right) number of primary vertices. In the lower panels, the grey filled areas represent the total statistical and systematic uncertainties, whereas the dotted lines are the average SF_b values within statistical uncertainties.

820 The measurement of the misidentification probability for light-parton jets relies on
 821 the inversion of tagging algorithms, selecting non-b jets using the same variables and
 822 techniques used in benchmarking the b-tagging efficiency. The scale factors (SF_s) to be
 823 applied to MC are shown in Figure 3.8 for the CSVM tagger.

824 3.4. Triggering System

825 With bunch crossings separated by just 25 ns, the rate at which data from all collisions
 826 would have to be written out and processed would be unfeasible. A two-tiered triggering
 827 system is applied at CMS in order to cope with the high collision rate of protons. The
 828 CMS trigger is designed to use limited information from each event to determine whether
 829 to record the event, reducing the rate of data taking to manageable levels whilst ensuring
 830 a high efficiency of interesting physics object events are selected.

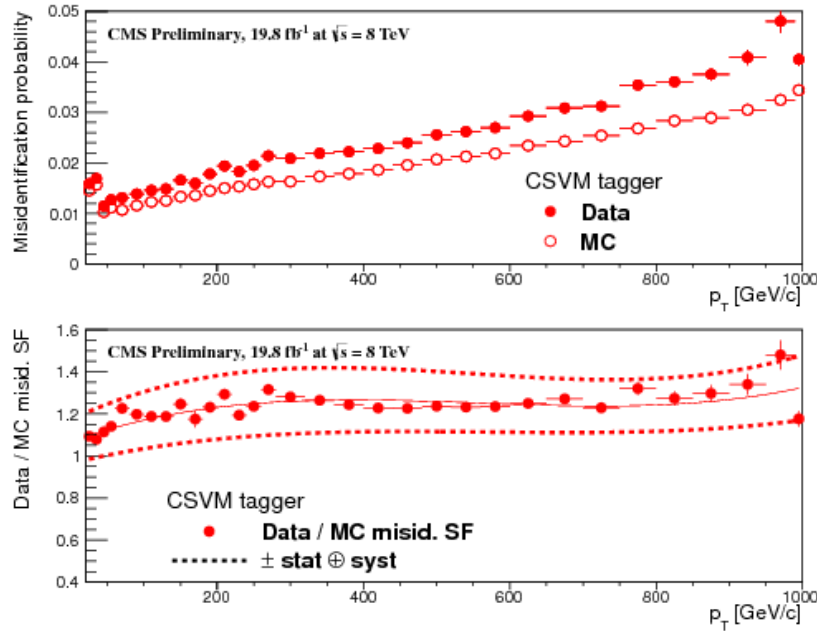


Figure 3.8.: For the **CSVM** tagging criterion: (top) misidentification probability in data (filled circles) and simulation (open circles); (bottom) scale factor for the misidentification probability. The last p_T bin in each plot includes all jets with $p_T > 1000$ GeV. The solid curve is the result of a polynomial fit to the data points. The dashed curves represent the overall statistical and systematic uncertainties on the measurements.

831 The **L1** is a pipelined, dead-timeless system based on custom-built electronics [66],
 832 and is a combination of several sub systems which is shown pictorially in Figure 3.9. The
 833 L1 system is covered in more detail within the following section along with a description
 834 of the service work undertaken by the author to benchmark the performance of the L1
 835 calorimeter trigger during the 2012 8 TeV run period.

836 The Higher Level Trigger (**HLT**) is a large farm of commercial computers [67]. The
 837 **HLT** processes events with software reconstruction algorithms that are more detailed,
 838 giving performance more similar to the reconstruction used offline. The **HLT** reduces
 839 the event rate written to disk by a factor of ~ 500 (~ 200 Hz). The recorded events are
 840 transferred from **CMS** to the **CERN** computing centre, where event reconstruction is
 841 performed, and then distributed to **CMS** computing sites around the globe for storage
 842 and analysis.

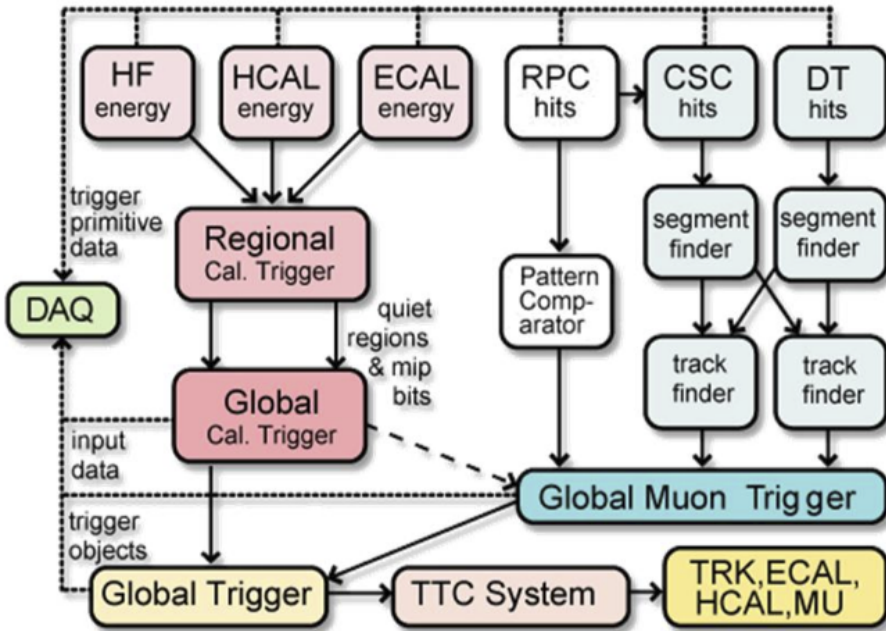


Figure 3.9.: The CMS L1 Trigger system.

3.4.1. The Level-1 Trigger

The L1 trigger reduces the rate of events collected from 40 MHz to ~ 100 kHz using information from the calorimeters and muon chambers, but not the tracker. A tree system of triggers is used to decide whether to pass on an event to the HLT for further reconstruction. Firstly the calorimeter and muon event information is kept separate, with local reconstruction of objects ($\mu, e, \gamma, \text{jets}$) performed by the Regional Calorimeter Trigger (RCT) and Regional Muon Trigger (RMT) respectively. The RCT generates up to 72 isolated and non-isolated electromagnetic objects. These are sorted by rank, which is equivalent to transverse energy E_T , with the four highest ranked electromagnetic objects being passed via the Global Calorimeter Trigger (GCT) and Global MuonTrigger (GMT) to the Global Trigger (GT).

In the L1 GCT, coarse measurements of the energy deposited in the electromagnetic and hadronic calorimeters are combined and by using sophisticated algorithms the following physics objects are formed:

- isolated and non-isolated electromagnetic objects (e and γ);
- hadronic jets in the central and forward sections of the hadronic calorimeters;

- 859 • hadronically decaying tau leptons;
- 860 • total transverse energy (E_T), the scalar sum of the energy measured at L1, and
861 missing transverse energy (\cancel{E}_T), defined as the vector sum of the energy of L1
862 objects;
- 863 • total transverse jet energy (H_T), the scalar sum of the energy of all L1 jet objects,
864 and missing transverse jet energy (\cancel{H}_T), defined as the vector sum of the energy of
865 L1 jets, are calculated from uncorrected L1 jets.

866 In addition quantities suitable for triggering minimum bias events, forward physics and
867 beam background events are calculated. Additionally relevant muon isolation information
868 is also passed on to the **GMT** for decisions involving the muon triggers where it is
869 combined with information from across the three muon sub-systems. The resultant final
870 accept/reject decision at **L1** is then performed by the **GT** based on the objects received
871 from the **GCT** and **GMT** (e/γ , μ , jets, E_T , \cancel{E}_T , H_T).

872 The L1 trigger is therefore of upmost importance to the functioning of the detector.
873 Without a high-performing trigger and a good understanding of it's performance, there
874 would be no data to analyse. Observations of how the L1 trigger performance is affected
875 by changing **LHC** running conditions over the 2012 run period and also the introduction
876 of a jet seed threshold to the L1 jet trigger algorithm is presented in the following Sections
877 (3.4.2 - 3.4.6).

878 3.4.2. L1 Trigger Jet Algorithm

879 The L1 jet trigger uses the transverse energy sums computed in the calorimeter (both
880 hadronic and electromagnetic) trigger regions. Each region consists of 4×4 trigger tower
881 windows, spanning a region of $\Delta\eta \times \Delta\phi = 0.087 \times 0.087$ in pseudorapidity-azimuth. The
882 jet trigger uses a 3×3 calorimeter region (112 trigger towers) sliding window technique
883 which spans the full (η, ϕ) coverage of the **CMS** calorimeter as shown in Figure 3.10.

884 In forming a L1 jet is it required that the central region to be higher than the eight
885 neighbouring regions $E_{T\text{central}} > E_{T\text{surround}}$. Additionally a minimum threshold of 5 GeV
886 on $E_{T\text{central}}$ was introduced during the 2012 run period to suppress noise from pile-up,
887 the effects of which are shown in Section (3.4.4).

888 The L1 jets are characterised by the E_T , summed over the 3×3 calorimeter regions,
889 which corresponds to 12×12 trigger towers in barrel and endcap or 3×3 larger **HF**

890 towers in the **HF**. The ϕ size of the jet window is the same everywhere, whilst the η
891 binning gets somewhat larger at high η due to calorimeter and trigger tower segmentation.
892 The jets are labelled by (η, ϕ) indexes of the central calorimeter region.

893 Jets with $|\eta| > 3.0$ are classified as forward jets, whereas those with $|\eta| < 3.0$ are
894 classified as central. The four highest energy central, forward and τ jets in the calorimeter
895 are passed through Look Up Table (**LUT**)'s, which apply a programmable η -dependent
896 jet energy scale correction. These are then used to make L1 trigger decisions.

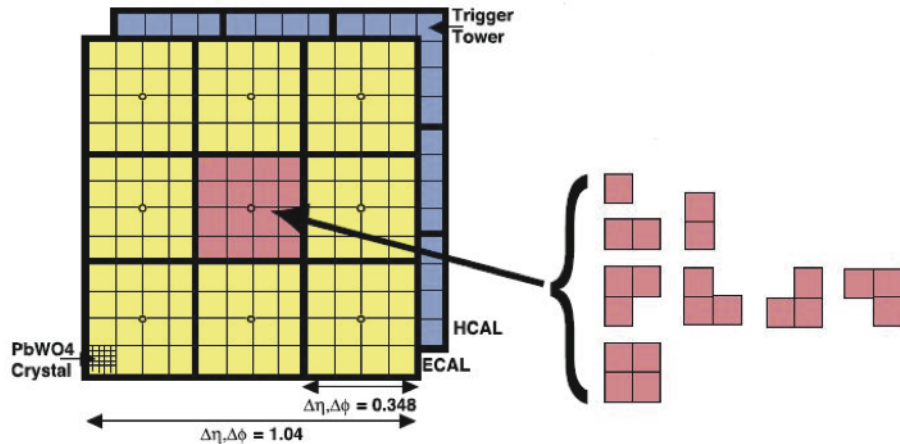


Figure 3.10.: Illustration of the Level-1 jet finding algorithm.

897 The performance of the L1 jets is evaluated with respect to offline jets, which are
898 taken from the standard Calo jet and the PF jet reconstruction algorithms of **CMS**.
899 Jets are corrected for pile-up and detector effects as described in [3.3.1](#). A moderate
900 level of noise rejection is applied to the offline jets by selecting jets passing the “loose
901 identification criteria for both Calo and PF. These criteria are summarised in Appendix
902 ([A.1](#)).

903 3.4.3. Measuring L1 Jet Trigger Efficiencies

904 The L1 jet efficiency is defined as the fraction of leading offline jets which were matched
905 with a L1 tau or central jet above a certain trigger threshold, divided by all the leading
906 offline jets in the event. This quantity is then plotted as a function of the offline jet E_T ,
907 η and ϕ .

908 The efficiency is determined by matching the L1 and reconstructed offline jets spatially
909 in $\eta - \phi$ space. This is done by calculating the minimum separation in ΔR between the

highest offline reconstructed jet in E_T ($E_T > 10$ GeV, $|\eta| < 3$) and any L1 jet. A jet will be matched if this value is found to be < 0.5 . Should more than one jet satisfy this, the jet closest in ΔR is taken as the matched jet. The matching efficiency is close to 100%, above ? 30(45) GeV for run 2012B(C) data (see Appendix (??)).

Each efficiency curve is fitted with a function which is the cumulative distribution function of an Exponentially Modified Gaussian (EMG) distribution:

$$f(x; \mu, \sigma, \lambda) = \frac{\lambda}{2} \cdot e^{\frac{\lambda}{2}(2\mu + \lambda\sigma^2 - 2x)} \cdot \text{erfc}\left(\frac{\mu + \lambda\sigma^2 - x}{\sqrt{2}\sigma}\right) \quad (3.3)$$

where erfc is the complementary error function defined as:

$$\text{erfc}(x) = 1 - \text{erf}(x) = \frac{2}{\sqrt{\pi}} \int_x^\infty e^{-t^2} dt.$$

In this functional form, the parameter μ determines the point of 50% of the plateau efficiency and the σ gives the resolution. This parametrisation is used to benchmark the efficiency at the plateau, the turn-on points and resolution for each L1 Jet trigger. The choice of function is purely empirical. Previous studies used the error function alone, which described the data well at high threshold values but could not describe the efficiencies well at lower thresholds [68].

The efficiency turn-on curves for various L1 jet thresholds are evaluated as a function of the offline reconstructed jet E_T for central jets with $|\eta| < 3$. These are measured using single isolated μ triggers which have high statistics, and are orthogonal and therefore unbiased to the hadronic triggers under study. The efficiency is calculated with respect to offline Calo and PF Jets in Figure 3.11. Table 3.1 shows the values of these parameters, calculated for three example L1 single jet triggers taken from 2012 8 TeV data.

The results from the L1 single jet triggers shows good performance for both Calo and PF jets. A better resolution for Calo jets with respect to L1 jets quantities is observed. This effect is due to Calo jet reconstruction using the same detector systems as in L1 jets, whereas with PF jet construction using tracker and muon information, a more smeared resolution when compared to L1 is expected.

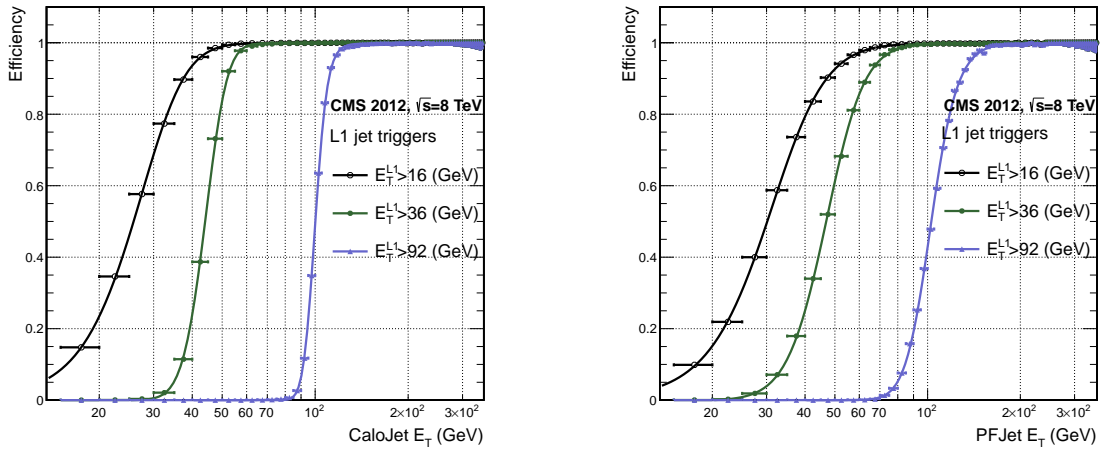


Figure 3.11.: L1 jet efficiency turn-on curves as a function of the offline CaloJet E_T (left) and PFJet E_T (right), measured in 2012 Run Period C data and collected with an isolated single μ data sample.

Trigger	Calo		PF	
	μ	σ	μ	σ
L1_SingleJet16	21.09 ± 0.03	7.01 ± 0.02	22.17 ± 0.04	7.83 ± 0.03
L1_SingleJet36	41.15 ± 0.05	5.11 ± 0.02	39.16 ± 0.06	8.04 ± 0.03
L1_SingleJet92	95.36 ± 0.13	5.62 ± 0.03	90.85 ± 0.19	11.30 ± 0.10

Table 3.1.: Results of a cumulative EMG function fit to the turn-on curves for L1 single jet triggers in run 2012 Run Period C, measured in an isolated μ data sample. The turn-on point, μ , and resolution, σ , of the L1 jet triggers are measured with respect to offline Calo Jets (left) and PF Jets (right).

3.4.4. Effects of the L1 Jet Seed

Between run period B and C of the 2012 data taking period, a jet seed threshold was introduced into the L1 trigger jet algorithm. There was previously no direct requirement made on the energy deposited in the central region. The introduction of a jet seed threshold required that the central region have $E_T \geq 5\text{GeV}$, and was introduced to counteract the effects of high pile up running conditions which create a large number of soft non-collimated jets, that are then added to the jets from the primary interaction or other soft jets from other secondary interactions [69]. This in turn causes a large increase in trigger rate due to the increase in the likelihood that the event causes the L1 trigger to fire. This was implemented to maintain trigger thresholds by cutting the rate of events recorded without significant reduction in the efficiency of physics events of interest.

The effect of the introduction of this jet seed threshold between these two run periods is benchmarked through a comparison of the efficiency of the L1 jet triggers with respect to offline Calo jets shown in Figure 3.12, and the L1 H_T trigger efficiency in Figure 3.14 which is compared to offline H_T constructed from Calo jets with $E_T \geq 40\text{GeV}$.

To negate any effects from different pile-up conditions in the run periods, the efficiencies are measured in events which contain between 15 and 20 primary vertices as defined in Appendix (A.2).

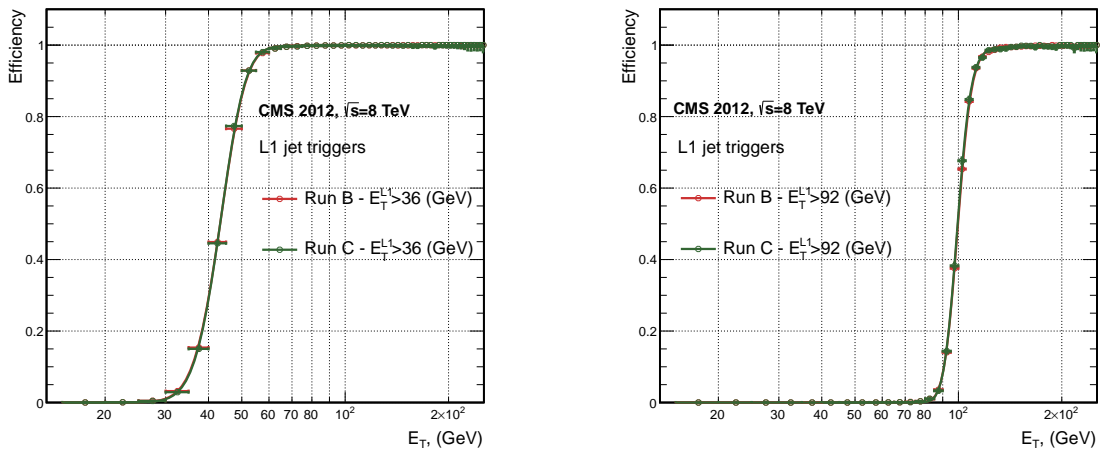


Figure 3.12.: L1 jet efficiency turn-on curves as a function of the offline CaloJet E_T , measured for the L1 SingleJet 36 and 92 trigger in 2012 run period B and C collected with an isolated single μ' sample.

It can be seen that the performance of the $E_T > 36, 92$ single jet are almost identical, with the jet seed having no measurable effect on these triggers as shown in Table 3.2 .

Trigger	2012B		2012C	
	μ	σ	μ	σ
L1_SingleJet36	40.29 ± 0.04	5.34 ± 0.02	40.29 ± 0.11	5.21 ± 0.05
L1_SingleJet92	94.99 ± 0.09	5.93 ± 0.06	94.82 ± 0.29	5.74 ± 0.18

Table 3.2.: Results of a cumulative EMG function fit to the turn-on curves for L1 single jet triggers in the 2012 run period B and C, preselected on an isolated muon trigger. The turn-on point μ and resolution σ of the L1 jet triggers are measured with respect to offline Calo Jets in run B (left) and run C (right).

For the H_T triggers, a large increase in rate during high pile-up conditions is expected. This is due to the low energy threshold required for a jet to be added to the L1 H_T sum,

which is compiled from all uncorrected L1 jets formed in the RCT. The introduction of the jet seed threshold removes the creation of many of these soft low E_T jets, thus lowering the H_T calculation at L1. The effect on the trigger cross section for L1 H_T 150 trigger can be seen in Figure 3.13.

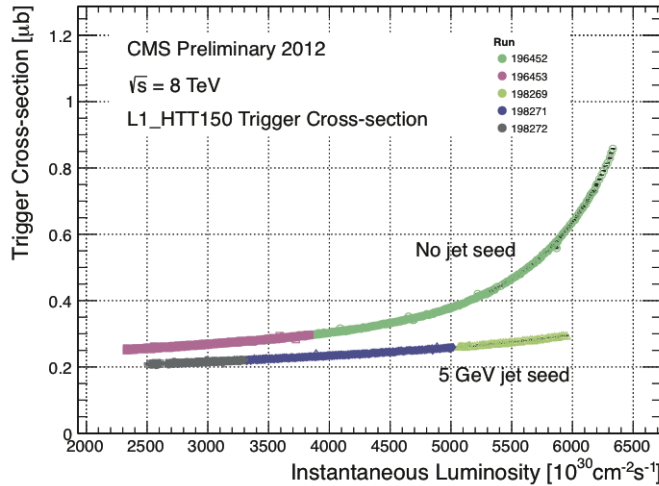


Figure 3.13.: Trigger cross section for the L1HTT150 trigger path. Showing that a 5 GeV jet seed threshold dramatically reduces the dependance of cross section on the instantaneous luminosity for L1 H_T triggers [70].

Different behaviours for the trigger turn ons between these run periods are therefore expected. The turn on point is observed to shift to higher H_T values after the introduction of the jet seed threshold, whilst having a sharper resolution due to less pile-up jets being included the H_T sum, the results are shown in Table 3.3.

Trigger	2012B		2012C	
	μ	σ	μ	σ
L1 HT-100	157.5 ± 0.08	32.9 ± 0.08	169.8 ± 0.08	28.7 ± 0.03
L1 H1-150	230.9 ± 0.02	37.3 ± 0.01	246.4 ± 0.16	31.8 ± 0.05

Table 3.3.: Results of a cumulative EMG function fit to the turn-on curves for H_T in run 2012 B and C, preselected on an isolated single μ trigger. The turn-on point μ , resolution σ of the L1 H_T triggers are measured with respect to offline H_T formed from CaloJets with a $E_T \geq 40$ in run period B (left) and C (right).

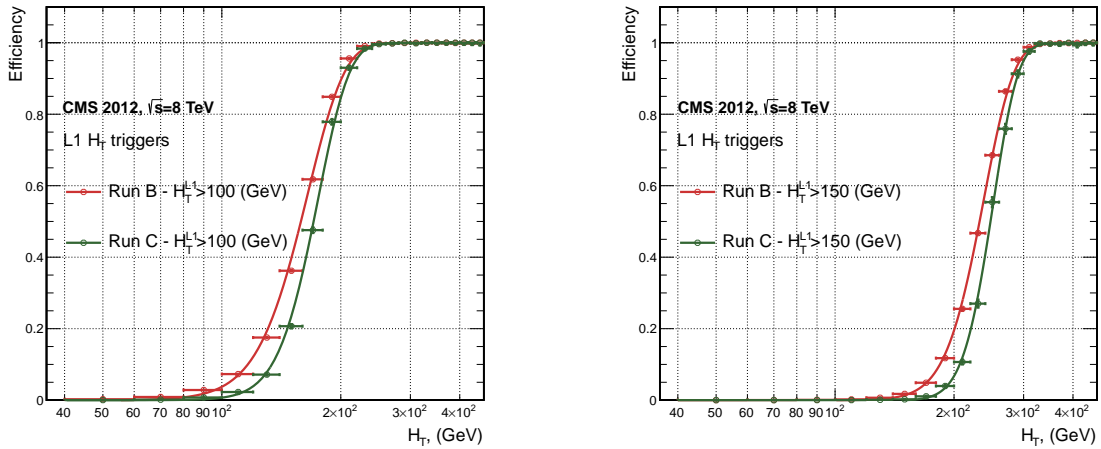


Figure 3.14.: L1 H_T efficiency turn-on curves as a function of the offline CaloJet H_T , measured for the L1 H_T 100 and 150 trigger during the run 2012 B and C collected using an isolated single μ triggered sample.

964 3.4.5. Robustness of L1 Jet Performance against Pile-up

965 The performance of the L1 single jet triggers is evaluated in different pile-up conditions
966 to benchmark any dependence on pile-up. Three different pile-up bins of 0-10, 10-20 and
967 >20 vertices are defined, reflecting the low, medium and high pile-up running conditions
968 at CMS in 2012. This is benchmarked relative to Calo and PF jets for the run 2012 C
969 period where the jet seed threshold is applied, with L1 single jet thresholds of 16, 36 and
970 92 GeV, shown in Figure 3.15. The results of fits to these efficiency turn-on curves are
971 given in Table 3.4 and Table 3.5 for Calo and PF jets respectively.

Vertices	0-10		11-20		> 20	
	μ	σ	μ	σ	μ	σ
L1_SingleJet16	19.9 ± 0.1	6.1 ± 0.3	20.8 ± 0.1	6.5 ± 0.1	22.3 ± 0.2	7.5 ± 0.1
L1_SingleJet36	41.8 ± 0.1	4.6 ± 0.1	40.9 ± 0.1	5.1 ± 0.1	40.6 ± 0.6	5.9 ± 0.2
L1_SingleJet92	95.9 ± 0.2	5.4 ± 0.1	95.2 ± 0.2	5.6 ± 0.1	94.5 ± 0.6	6.2 ± 0.3

Table 3.4.: Results of a cumulative EMG function fit to the efficiency turn-on curves for L1 single jet triggers in the 2012 run period C, measured from isolated μ triggered data. The turn-on point, μ , and resolution, σ , of the L1 jet triggers are measured with respect to offline Calo jets in low (left), medium (middle) and high (right) pile-up conditions.

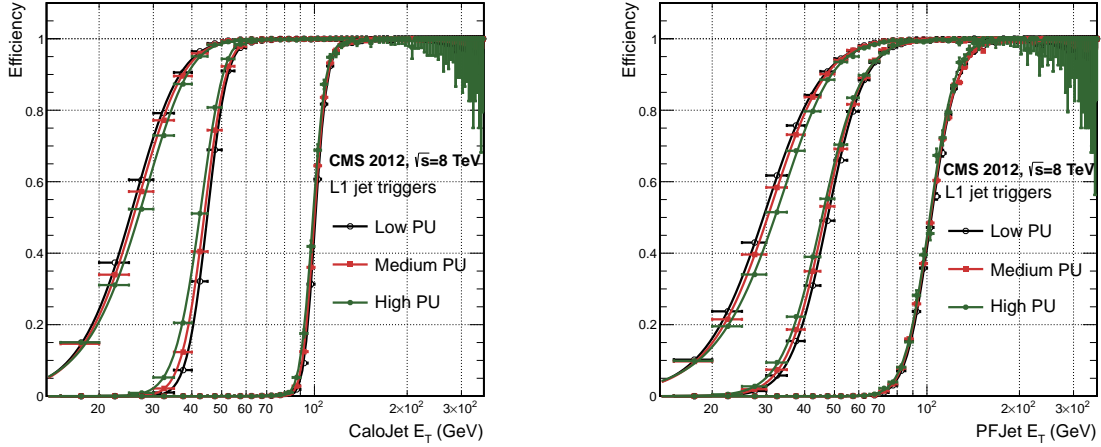


Figure 3.15.: L1 jet efficiency turn-on curves as a function of the leading offline E_T Calo (left) and PF (right) jet, for low, medium and high pile-up conditions.

Vertices	0-10		11-20		> 20	
	μ	σ	μ	σ	μ	σ
L1_SingleJet16	21.1 ± 0.1	7.16 ± 0.05	22.34 ± 0.1	7.9 ± 0.1	24.6 ± 0.2	9.5 ± 0.1
L1_SingleJet36	39.6 ± 0.1	7.4 ± 0.1	38.4 ± 0.1	7.4 ± 0.1	37.1 ± 0.2	7.5 ± 0.1
L1_SingleJet92	91.6 ± 0.3	11.3 ± 0.2	90.4 ± 0.3	11.2 ± 0.1	92.0 ± 0.9	12.1 ± 0.4

Table 3.5.: Results of a cumulative EMG function fit to the efficiency turn-on curves for Level-1 single jet triggers in the 2012 run period C, measured from isolated μ triggered data. The turn-on point, μ , and resolution, σ , of the L1 jet triggers are measured with respect to offline PF jets in low (left), medium (middle) and high (right) pile-up conditions.

No significant drop in efficiency is observed in the presence of a high number of primary vertices. The increase in hadronic activity in higher pile-up conditions, combined with the absence of pile-up subtraction for L1 jets, results in the expected observation of a decrease in the μ value of the efficiency turn-ons as a function of pile-up, while the resolution, σ of the turn-ons are found to gradually worsen as expected with increasing pile-up.

These features are further emphasised when shown as a function of

$$\frac{(L1 E_T - Offline E_T)}{Offline E_T} \quad (3.4)$$

in bins of matched leading offline jet E_T , of which the individual fits can be found in Appendix (B.2). Each of these distributions are fitted with an EMG function as defined in Equation (3.3).

The μ , σ and λ values extracted for the low, medium and high pile-up conditions are shown for Calo and PF jets in Figure 3.16 and Figure 3.17 respectively. The central value of $\frac{(L1 E_T - \text{Offline } E_T)}{\text{Offline } E_T}$ is observed to increases as a function of jet E_T , whilst the resolution is also observed to improve at higher offline jet E_T .

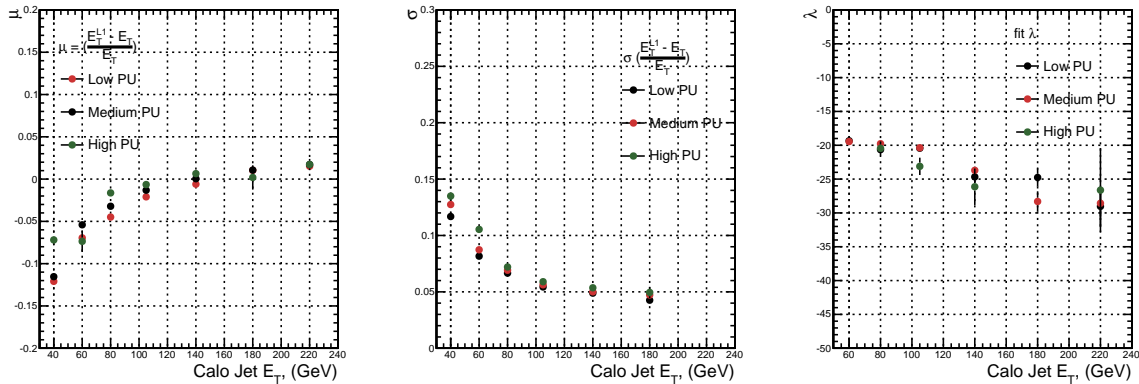


Figure 3.16.: Fit values from an EMG function fitted to the resolution plots of leading Calo jet E_T measured as a function of $\frac{(L1 E_T - \text{Offline } E_T)}{\text{Offline } E_T}$ for low, medium and high pile-up conditions. The plots show the mean μ (left), resolution σ (middle) of the Gaussian as well as the decay term λ (right) of the exponential.

The resolution of other L1 energy sum quantities, H_T , \not{E}_T and $\sum E_T$ parameterised as in Equation (3.4), can be found in Appendix (B.3). The same behaviour observed for the single jet triggers is also found for these quantities, where in the presence of higher pile-up the μ values are shifted to higher values, with a worsening resolution, σ again due to the increase in soft pile-up jets and the absence of pile-up subtraction at L1.

3.4.6. Summary

The performance of the CMS Level-1 Trigger has been studied and evaluated for jets and energy sum quantities using data collected during the 2012 LHC 8TeV run. These studies include the effect of introduction of a 5 GeV jet seed threshold into the jet algorithm configuration, the purpose of which is to mitigate the effects of pile-up on the rate of L1 triggers whilst not adversely affecting the efficiency of these triggers. No significant

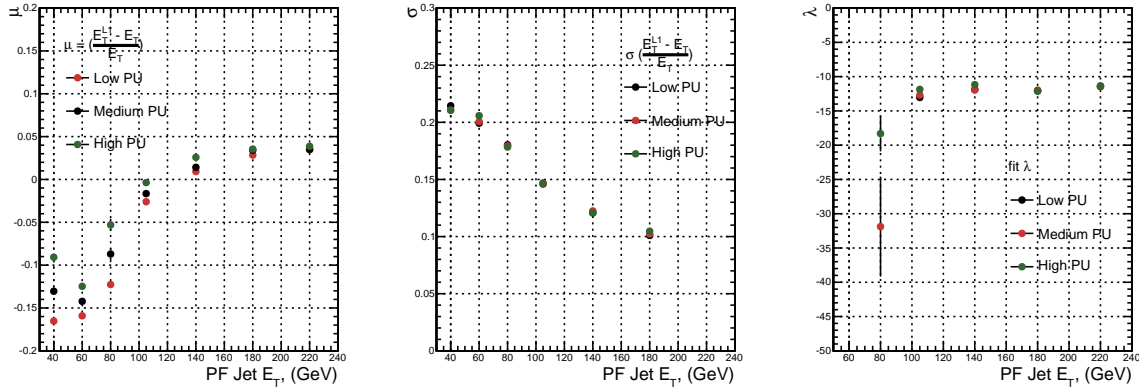


Figure 3.17.: Fit values from an **EMG** function fitted to the resolution plots of leading PF jet E_T measured as a function of $\frac{(L1\ E_T - \text{Offline}\ E_T)}{\text{Offline}\ E_T}$ for low and medium pile-up conditions. The plots show the mean μ (left), resolution σ (middle) of the Gaussian as well as the decay term λ (right) of the exponential.

997 change in performance is observed with this change and good performance is observed
 998 for a range of L1 quantities.

Chapter 4.

₉₉₉ SUSY searches in Hadronic Final ₁₀₀₀ States

₁₀₀₁ In this chapter a model independent search for **SUSY** in hadronic final states with \cancel{E}_T
₁₀₀₂ using the α_T variable and b-quark multiplicity is introduced and described in detail. The
₁₀₀₃ results presented are based on a data sample of pp collisions collected in 2012 at $\sqrt{s} = 8$
₁₀₀₄ TeV, corresponding to an integrate luminosity of $11.7 \pm 0.5 \text{ fb}^{-1}$.

₁₀₀₅ The kinematic variable α_T is motivated as a variable to provide strong rejections
₁₀₀₆ of QCD backgrounds, whilst maintaining sensitivity to possible a **SUSY** signal within
₁₀₀₇ Section (4.1). The search and trigger strategy in addition to the event reconstruction
₁₀₀₈ and selection are outlined within Sections (4.2-4.2.2).

₁₀₀₉ The method in which the **SM** background is estimated using an analytical technique
₁₀₁₀ to improve statistical precision at higher b-tag multiplicities is detailed within Section
₁₀₁₁ (4.4), with a discussion on the impact of b-tagging and mis-tagging scale factors between
₁₀₁₂ data and MC on any background predictions. Finally a description of the formulation of
₁₀₁₃ appropriate systematic uncertainties applied to the background predictions to account for
₁₀₁₄ theoretical uncertainties and limitations in the simulation modelling of event kinematics
₁₀₁₅ and instrumental effects is covered in Section (4.6).

₁₀₁₆ In addition to the α_T search, a complimentary technique is discussed as a means to
₁₀₁₇ predict the distribution of 3 and 4 reconstructed b-quark jets in an event in Section
₁₀₁₈ (4.7). The recent discovery of the Higgs boson has made third-generation “Natural **SUSY**”
₁₀₁₉ models attractive, given that light top and bottom squarks are a candidate to stabilise
₁₀₂₀ divergent loop corrections to the Higgs boson mass.

1021 Using the α_T search as a base, a simple templated fit is employed to estimate the
 1022 **SM** background in higher b-tag multiplicities (3-4) from a region of a low number
 1023 of reconstructed b-jets (0-2). The predictions using this technique are first tested in
 1024 simulation before being compared to the **SM** background predictions obtained from the
 1025 α_T search.

1026 The experimental reach of the analysis discussed within this thesis is interpreted in
 1027 two classes of **SMS** models, the topologies of which are detailed in Section (2.4.1). The
 1028 **SMS** models considered in this analysis are summaries in Table 4.1. For each model, the
 1029 **LSP** is assumed to be the lightest neutralino.

1030 Within Table 4.1 is also defined reference points, parameterised in terms of parent
 1031 gluino/squark and **LSP** sparticle masses, m_{parent} and m_{LSP} , respectively, which are used
 1032 within the following two chapters to demonstrate potential yields within the signal region
 1033 of the search. The masses are chosen to reflect parameter space which is within the
 1034 expect sensitivity reach of the search.

Model	Production/decay mode	Reference model	
		m_{parent}	m_{LSP}
G1 (T1)	$pp \rightarrow \tilde{g}\tilde{g}^* \rightarrow q\bar{q}\tilde{\chi}_1^0 q\bar{q}\tilde{\chi}_1^0$	700	300
G2 (T1bb)	$pp \rightarrow \tilde{g}\tilde{g}^* \rightarrow b\bar{b}\tilde{\chi}_1^0 b\bar{b}\tilde{\chi}_1^0$	900	500
G3 (T1tt)	$pp \rightarrow \tilde{g}\tilde{g}^* \rightarrow t\bar{t}\tilde{\chi}_1^0 t\bar{t}\tilde{\chi}_1^0$	850	250
D1 (T2)	$pp \rightarrow \tilde{q}\tilde{q}^* \rightarrow q\tilde{\chi}_1^0 \bar{q}\tilde{\chi}_1^0$	600	250
D2 (T2bb)	$pp \rightarrow \tilde{b}\tilde{b}^* \rightarrow b\tilde{\chi}_1^0 \bar{b}\tilde{\chi}_1^0$	500	150
D3 (T2tt)	$pp \rightarrow \tilde{t}\tilde{t}^* \rightarrow t\tilde{\chi}_1^0 \bar{t}\tilde{\chi}_1^0$	400	0

Table 4.1.: A summary of the **SMS** models interpreted in this analysis, involving both direct (D) and gluino-induced (G) production of squarks and their decays. Reference models are also defined in terms of parent and **LSP** sparticle mass

1035 4.1. An introduction to the α_T search

1036 The experimental signature of **SUSY** signal in the hadronic channel would manifest as a
 1037 final state containing energetic jets and \cancel{E}_T . The search focuses on topologies where new
 1038 heavy supersymmetric, R-parity conserving particles are pair-produced in pp collisions.
 1039 These particles decaying to a **LSP** escape the detector undetected, leading to significant
 1040 missing energy and missing hadronic transverse energy,

$$\mathcal{H}_T = \left| \sum_{i=1}^n p_T^{jet_i} \right|, \quad (4.1)$$

1041 defined as the vector sum of the transverse energies of jets selected in an event.
1042 Energetic jets produced in the decay of these supersymmetric particles also can produce
1043 significant visible transverse energy,

$$H_T = \sum_{i=1}^n E_T^{jet_i}, \quad (4.2)$$

1044 defined as the scalar sum of the transverse energies of jets selected in an event.

1045 A search within this channel is greatly complicated in a hadron collider environment,
1046 where the overwhelming background comes from inherently balanced multi-jet (“QCD”)
1047 events which are produced with an extremely large cross section as demonstrated within
1048 Figure 4.1. \cancel{E}_T can appear in such events with a substantial mis-measurement of jet
1049 energy or missed objects due to detector miscalibration or noise effects.

1050 Additional **SM** background from **EWK** processes with genuine \cancel{E}_T from escaping
1051 neutrinos comprise the irreducible background within this search and come mainly from:

- 1052 • $Z \rightarrow \nu\bar{\nu}$ + jets,
- 1053 • $W \rightarrow l\nu$ + jets in which a lepton falls outside of detector acceptance, or the lepton
1054 decays hadronically $\tau \rightarrow \text{had}$,
- 1055 • $t\bar{t}$ with at least one leptonic W decay,
- 1056 • small background contributions from DY, single top and Diboson (WW,ZZ,WZ)
1057 processes.

1058 The search is designed to have a strong separation between events with genuine and
1059 “fake” \cancel{E}_T which is achieved primarily through the dimensionless kinematic variable, α_T
1060 [71][72].

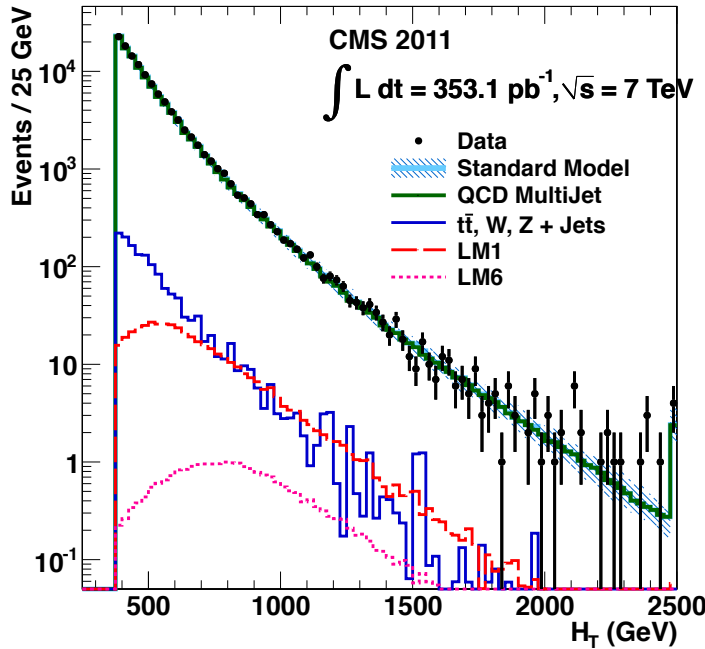


Figure 4.1.: Reconstructed offline H_T for 11.7fb^{-1} of data after a basic pre-selection. Sample is collected from prescaled H_T triggers. Overlaid are expectations from MC simulation of EWK processes as well as a reference signal model (labelled D2 from Table 4.1).

1061 4.1.1. The α_T variable

1062 For a perfectly measured di-jet QCD event, conservation laws dictate that they must be
 1063 produced back-to-back and of equal magnitude. However in di-jet events with real \cancel{E}_T , both of these jets are produced independently of one another, depicted in Figure 4.2.

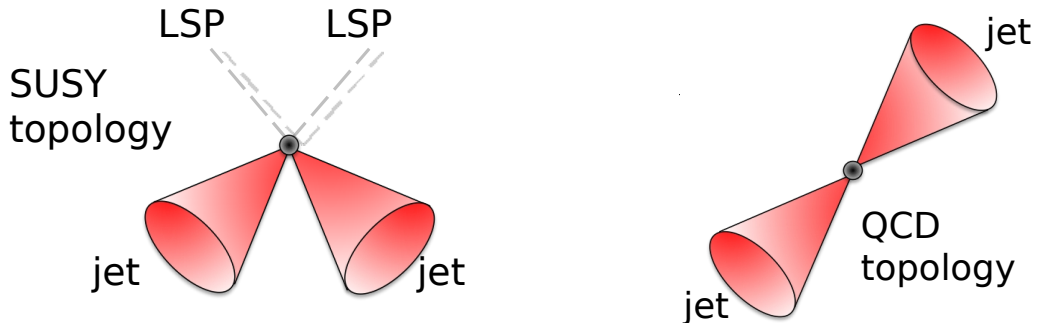


Figure 4.2.: The event topologies of background QCD dijet events (right) and a generic SUSY signature with genuine \cancel{E}_T (left).

1065 Exploiting this feature leads to the formulation of α_T in di-jet systems defined as,

$$\alpha_T = \frac{E_T^{j2}}{M_T}, \quad (4.3)$$

1066 where E_T^{j2} is the transverse energy of the least energetic of the two jets and M_T
1067 defined as:

$$M_T = \sqrt{\left(\sum_{i=1}^2 E_T^{ji}\right)^2 - \left(\sum_{i=1}^2 p_x^{ji}\right)^2 - \left(\sum_{i=1}^2 p_y^{ji}\right)^2} \equiv \sqrt{H_T^2 - \cancel{H}_T^2}. \quad (4.4)$$

1068 A perfectly balanced di-jet event i.e. $E_T^{j1} = E_T^{j2}$ would give an $\alpha_T = 0.5$, where as
1069 events with jets which are not back-to-back, for example in events in which a W or Z
1070 recoils off a system of jets, α_T can achieve values in excess of 0.5.

1071 α_T can be extended to apply to any arbitrary number of jets, undertaken by modelling
1072 a system of n jets as a di-jet system, through the formation of two pseudo-jets [73].
1073 The two pseudo-jets are built by merging the jets present in the event such that the 2
1074 pseudo-jets are chosen to be as balanced as possible, i.e the $\Delta H_T \equiv |E_T^{pj1} - E_T^{pj2}|$ is
1075 minimised between the two pseudo jets. Using Equation (4.4), α_T can be rewritten as,

$$\alpha_T = \frac{1}{2} \frac{H_T - \Delta H_T}{\sqrt{H_T^2 - \cancel{H}_T^2}} = \frac{1}{2} \frac{1 - \Delta H_T/H_T}{\sqrt{1 - (\cancel{H}_T/H_T)^2}}. \quad (4.5)$$

1076 The distribution of α_T for the two jet categories used within this analysis, 2,3 and
1077 ≥ 4 jets, is shown in the Figure 4.3, demonstrating the ability of the α_T variable to
1078 discriminate between multi jet events and EWK processes with genuine \cancel{E}_T in the final
1079 state.

1080 The α_T requirement used within the search is chosen to be $\alpha_T > 0.55$ to ensure
1081 that the QCD multijet background is negligible even in the presence of moderate jet
1082 mis-measurement. There still remains other effects which can cause multijet events to
1083 artificially have a large α_T value, which are discussed in detail in Section (4.2.2).

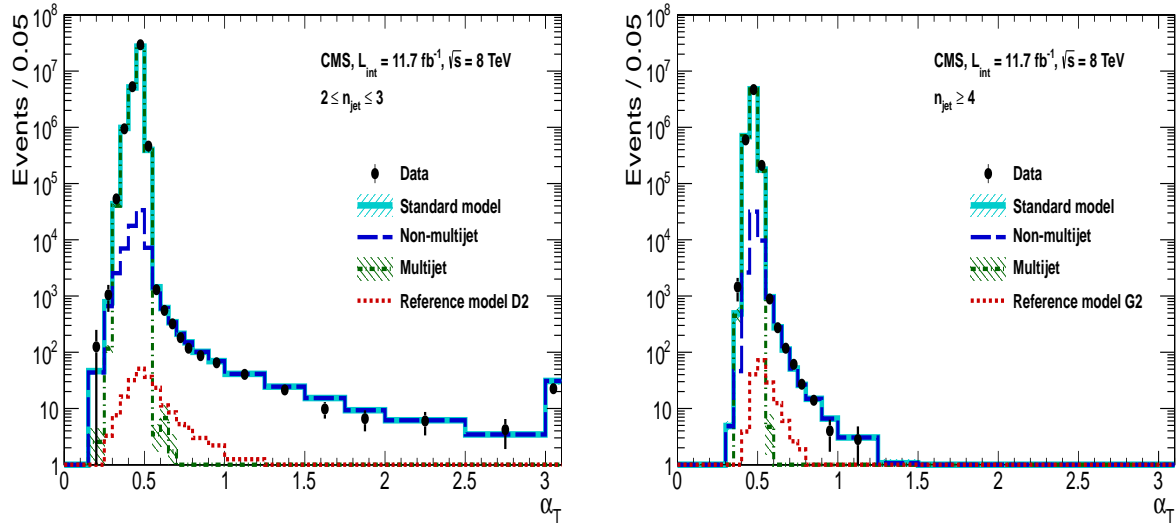


Figure 4.3.: The α_T distributions for the low 2-3 (left) and high ≥ 4 (right) jet multiplicities after a full analysis selection and shown for $H_T > 375$. Data is collected using both prescaled H_T triggers and dedicated α_T triggers for below and above $\alpha_T = 0.55$ respectively. . Expected yields as given by simulation are also shown for multijet events (green dash-dotted line), EWK backgrounds with genuine \cancel{E}_T (blue long-dashed line), the sum of all SM processes (cyan solid line) and the reference signal model D2 (left, red dotted line) or G2 (right, red dotted line).

4.2. Search Strategy

The aim of the analysis presented in this thesis is to identify an excess of events in data over the SM background expectation in multi-jet final states and significant \cancel{E}_T . The essential suppression of the dominant QCD background for such a search is addressed by the α_T variable described in the previous section. For estimation of the remaining EWK backgrounds, three independent data control samples are used to predict the different processes that compose the background :

- $\mu + \text{jets}$ to determine $W + \text{jets}$, $t\bar{t}$ and single top backgrounds,
- $\gamma + \text{jets}$ to determine the irreducible $Z \rightarrow \nu\bar{\nu} + \text{jets}$ background,
- $\mu\mu + \text{jets}$ to determine the irreducible $Z \rightarrow \nu\bar{\nu} + \text{jets}$ background.

These control samples are chosen to both be rich in specific EWK processes, be free of QCD multi-jet events and to also be kinematically similar to the hadronic signal region that they are estimating the backgrounds of, see Section (4.2.3).

1097 To remain inclusive to a large range of possible **SUSY** models, the signal region is
1098 binned in the following categories to allow for increased sensitivity in the interpretation
1099 of results for different **SUSY** topologies:

1100 **Sensitivity to a range of SUSY mass splittings**

1101 The hadronic signal region is defined by $H_T > 275$, divided into eight bins in H_T .

- 1102 – Two bins of width 50 GeV in the range $275 < H_T < 375$ GeV,
- 1103 – five bins of width 100 GeV in the range $375 < H_T < 875$ GeV,
- 1104 – and a final open bin, $H_T > 875$ GeV.

1105 The choice at low H_T is driven primarily by trigger constraints. The mass difference
1106 between the **LSP** and the particle that it decays from is an important factor in the
1107 amount of hadronic activity in the event.

1108 A large mass splitting will lead to hard high p_T jets which contribute to the H_T
1109 sum. From Figure 4.1 it can be seen that the **SM** background falls sharply at high
1110 H_T values, therefore a large number of H_T bins will lead to easier identification
1111 of such signals. Conversely smaller mass splittings lead to softer jet p_T 's which will
1112 subsequently fall into the lower H_T range.

1113 **Sensitivity to production method of SUSY particles**

1114 The production mechanism of any potential **SUSY** signal can lead to different event
1115 topologies. One such way to discriminate between gluino ($g\tilde{g}$ - “high multiplicity”),
1116 and direct squark ($q\tilde{q}$ - “low multiplicity”) induced production of **SUSY** particles is
1117 realised through the number of reconstructed jets in the final state.

1118 The analysis is thus split into two jet categories : 2-3 jets , ≥ 4 jets to give sensitivity
1119 to both of these mechanisms.

1120 **Sensitivity to “Natural SUSY” via tagging jets from b-quarks**

1121 Jets originating from bottom quarks (b-jets) are identified through vertices that
1122 are displaced with respect to the primary interaction. The algorithm used to tag
1123 b-jets is the Combined Secondary Vertex Medium Working Point (**CSV**) tagger,
1124 described within Section (3.3.2). A cut is placed on the discriminator variable of
1125 > 0.679 , leading to a gluon/light-quark mis-tag rate of 1% and a jet p_T dependant
1126 b-tagging efficiency of 60-70% [64].

Natural **SUSY** models would be characterised through final-state signatures rich in bottom quarks. A search relying on methods to identify jets originating from bottom quarks through b-tagging, will significantly improve the sensitivity to this class of signature.

This is achieved via the binning of events in the signal region according to the number of b-tagged jets reconstructed in each event, in the following: 0,1,2,3, ≥ 4 b-tag categories . In the highest ≥ 4 b-tag category due to a limited number of expected signal and background, just three H_T bins are employed: 275-325 GeV, 325-375 GeV, ≥ 375 GeV.

This characterisation is identically mirrored in all control samples, with the information from all samples and b-tag categories used simultaneously in the likelihood model (see Chapter 5) in order to interpret the results in a coherent and powerful way.

The combination of the H_T , jet multiplicity and b-tag categorisation of the signal region as described above, resultantly leads to 67 different bins in which the analysis is interpreted in, which is depicted in Figure 4.4.

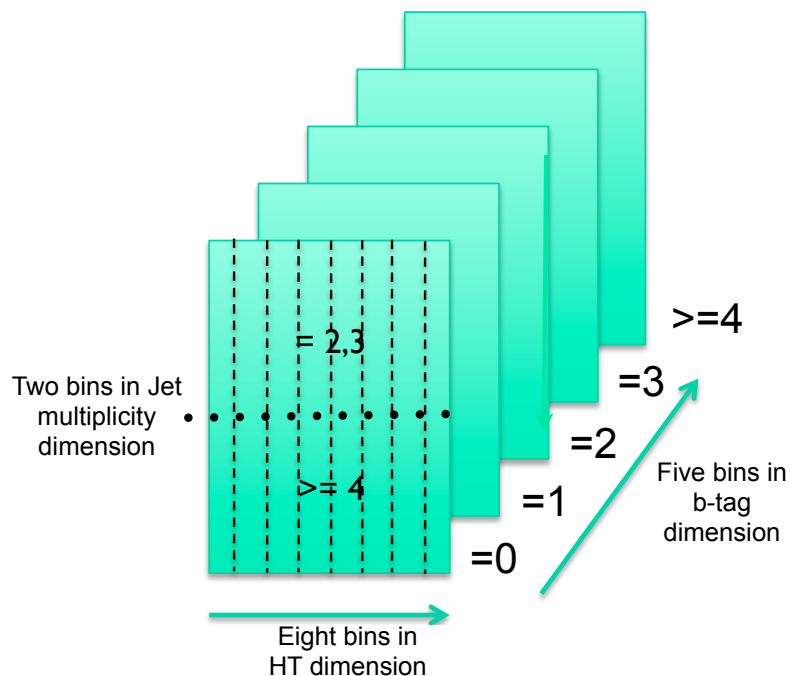


Figure 4.4.: Pictorial depiction of the analysis strategy employed by the α_T search to increase sensitivity to a wide spectra of **SUSY** models.

¹¹⁴³ 4.2.1. Physics Objects

¹¹⁴⁴ The physics objects used in the analysis defined below, follow the recommendation of
¹¹⁴⁵ the various CMS Physics Object Groups ([POGs](#)).

¹¹⁴⁶ • **Jets**

¹¹⁴⁷ The jets used in this analysis are CaloJets, reconstructed as described in Section
¹¹⁴⁸ ([3.3.1](#)) using the anti- k_T jet clustering algorithm.

¹¹⁴⁹ To ensure the jet object falls within the calorimeter systems a pseudo-rapidity
¹¹⁵⁰ requirement of $|\eta| < 3$ is applied. Each jet must pass a “loose” identification criteria
¹¹⁵¹ to reject jets resulting from unphysical energy, the criteria of which are detailed in
¹¹⁵² Table [4.2](#) [[74](#)].

Variable	Definition
$f_{HPD} < 0.98$	Fraction of jet energy contributed from “hottest” HPD , which rejects HCAL noise.
$f_{EM} > 0.01$	Noise from the HCAL is further suppressed by requiring a minimal electromagnetic component to the jet f_{EM} .
$N_{hits}^{90} \geq 2$	Jets that have $> 90\%$ of its energy from a single channel are rejected, to serve as a safety net that catches jets arising from undiagnosed noisy channels.

Table 4.2.: Jet Identification criteria for the “loose” CaloJet ID, used to reject reconstructed jets resulting from fake calorimeter deposits representing unphysical energy.

¹¹⁵³ • **Muons**

¹¹⁵⁴ Muons are selected in the $\mu +$ jets and $\mu\mu +$ jets control samples, and vetoed in
¹¹⁵⁵ the signal region. The same cut based identification criteria is applied to muons in
¹¹⁵⁶ both search regions and is summarised in Table [4.3](#) [[75](#)].

¹¹⁵⁷ Additionally muons are required to be within the acceptance of the muon tracking
¹¹⁵⁸ systems. For the muon control samples, trigger requirements necessitate a $|\eta| <$
¹¹⁵⁹ 2.1 for the selection of muons. In the signal region where muons are vetoed these
¹¹⁶⁰ conditions are relaxed to $|\eta| < 2.5$ and a minimum threshold of $p_T > 10$ GeV is
¹¹⁶¹ required of muon objects.

¹¹⁶² • **Photons**

Categories	Criteria
Global Muon	True
PFMuon	True
χ^2	< 10
Muon chamber hits	> 0
Muon station hits	> 1
Transvere impact d_{xy}	< 0.2mm
Longitudinal distance d_z	< 0.5mm
Pixel hits	> 0
Track layer hits	> 5
PF Isolation (DeltaB corrected)	<0.12

Table 4.3.: Muon Identification criteria used within the analysis for selection/veto purposes in the muon control/signal selections.

1163 Photons are selected within the $\gamma +$ jets control sample and vetoed in all other
1164 selections. Photons are identified in both cases according to the cut based criteria
1165 listed in Table 4.4 [76].

Variable	Definition
$H/E < 0.05$	The ratio of hadronic energy in the HCAL tower directly behind the ECAL super-cluster and the ECAL super-cluster itself.
$\sigma_{in\eta} < 0.011$	The log energy weighted width (σ), of the extent of the shower in the η dimension.
$R9 < 1.0$	The ratio of the energy of the 3×3 crystal core of the super-cluster compared to the total energy stored in the 5×5 super-cluster.
Combined Isolation < 6 GeV	The photons are required to be isolated with no electromagnetic or hadronic activity within a radius $\Delta R = 0.3$ of the photon object. A combination of the pileup subtracted [77], ECAL , HCAL and tracking isolation sums are used to determine the combined total isolation value.

Table 4.4.: Photon Identification criteria used within the analysis for selection/veto purposes in the $\gamma +$ jets control/signal selections.

1166 Photon objects are also required to have a minimum momentum of $p_T > 25$ GeV.

1167 **• Electrons**

1168 Electron identification is defined for veto purposes. They are selected according to
1169 the following cut-based criteria listed in Table 4.5, utilising PF-based isolation.

Categories	Barrel	EndCap
$\Delta\eta_{In}$	0.007	0.009
$\Delta\phi_{In}$	0.15	0.10
$\sigma_{inj\eta}$	0.01	0.03
H/E	0.12	0.10
d0 (vtx)	0.02	0.02
dZ (vtx)	0.20	0.20
$ (1/E_{ECAL} - 1/p_{track}) $	0.05	0.05
PF Combined isolation/ p_T	0.15	0.15
Vertex fit probability	10^{-6}	10^{-6}

Table 4.5.: Electron Identification criteria used within the analysis for veto purposes.

1170 Electrons are required to be identified at $|\eta| < 2.5$, with a minimum $p_T > 10$ GeV
1171 threshold to ensure that the electron falls within the tracking system of the detector.

1172 **• Noise and E_T Filters**

1173 A series of Noise filters are applied to veto events which contain spurious non-physical
1174 jets that are not picked up by the jet id, and events which give large unphysical E_T
1175 values. These filters are listed within Appendix (A.1).

1176 **4.2.2. Event Selection**

1177 The selection criteria for events within the analysis are detailed below. A set of common
1178 cuts are applied to both signal (maximise acceptance to a range of SUSY signatures), and
1179 control samples (retain similar jet kinematics for background predictions), with additional
1180 selection cuts applied to each control sample to enrich the sample in a particular EWK
1181 processes, see Section (4.2.3).

1182 The jets considered in the analysis are required to have a transverse momentum $p_T >$
1183 50 GeV, with a minimum of two jets required in the event. The highest E_T jet is required
1184 to lie within the central tracker acceptance $|\eta| < 2.5$, and the two leading p_T jets must

1185 each have $p_T > 100\text{GeV}$. Any event which has a jet with $p_T > 50\text{ GeV}$ that either fails
1186 the “loose” identification criteria described in Section(4.2.1) or has $|\eta| > 3.0$, is rejected.
1187 Similarly events in which an electron,muon or photon fails object identification but pass
1188 η and p_T restrictions are identified as an “odd” lepton/photon and the event is vetoed.

1189 At low H_T , the jet threshold requirements applied to be considered as part of the
1190 analysis and enter the H_T sum are scaled downwards. These are scaled down in order to
1191 not restrict phase space, preserving jet multiplicities and background admixture in the
1192 lower H_T bins, as listed in Table 4.6.

H_T bin	minimum jet p_T	second leading jet p_T
$275 < H_T < 325$	36.7	73.3
$325 < H_T < 375$	43.3	86.6
$375 < H_T$	50.0	100.0

Table 4.6.: Jet thresholds used in the three H_T regions of the analysis.

1193 Within the signal region to suppress **SM** processes with genuine \cancel{E}_T from neutrinos,
1194 events containing isolated electrons or muons are vetoed. Furthermore to ensure a pure
1195 multi-jet topology, events are vetoed if an isolated photon is found with $p_T > 25\text{ GeV}$.

1196 An α_T requirement of > 0.55 is required to reduce the QCD multi-jet background
1197 to a negligible amount. Finally additional cleaning cuts are applied to protect against
1198 pathological deficiencies such as reconstruction failures or severe energy mis-measurements
1199 due to detector inefficiencies:

- Significant \cancel{H}_T can arise in events with no real \cancel{E}_T due to multiple jets falling below the p_T threshold used for selecting jets. This in turn leads to events which can then incorrectly pass the α_T requirements of the analysis. This effect can be negated by requiring that the missing transverse momentum reconstructed from jets alone does not greatly exceed the missing transverse momentum reconstructed from all of the detector’s calorimeter towers,

$$\cancel{H}_T/\cancel{E}_T < 1.25.$$

- 1200 • Fake \cancel{E}_T and \cancel{H}_T can arise due to significant jet mis-measurements cause by a small
1201 number of non-functioning **ECAL** regions. These regions absorb electromagnetic
1202 showers which are subsequently not added to the jet energy sum. To circumvent

1203 this problem the following procedure is employed : For each jet in the event, the
1204 angular separation

$$\Delta\phi_j^* \equiv \Delta\phi(\vec{p}_j - \sum_{i \neq j} \vec{p}_i), \quad (4.6)$$

1205 is calculated where that jet is itself removed from the event. Here $\Delta\phi^*$ is a measure
1206 of how aligned the H_T of an event is with a jet, a small value is compatible with the
1207 hypothesis of an inherently balanced event in which a jet has been mis-measured.
1208 For every jet in a event with $\Delta\phi^* < 0.5$, if the ΔR distance between the selected jet
1209 and the closest dead **ECAL** region is also < 0.3 , then the event is rejected. Similarly
1210 events are rejected if the jet points within $\Delta R < 0.3$ of the **ECAL** barrel-endcap
1211 gap at $|\eta| = 1.5$.

1212 Some of the key distributions of the data used in this analysis compared to MC
1213 simulation are shown in Figure 4.5. The MC samples are normalised to a luminosity of
1214 11.7 fb^{-1} , with no requirement placed upon the number of b-tagged jets or number of
1215 jets in the events.

1216 The distributions shown are presented for purely illustrative purposes, with the MC
1217 simulation itself not used in absolute term to estimate the yields from background
1218 processes, see Sections (4.2.3,4.4). However it is nevertheless important to demonstrate
1219 that good agreement exists between simulation and observation in data.

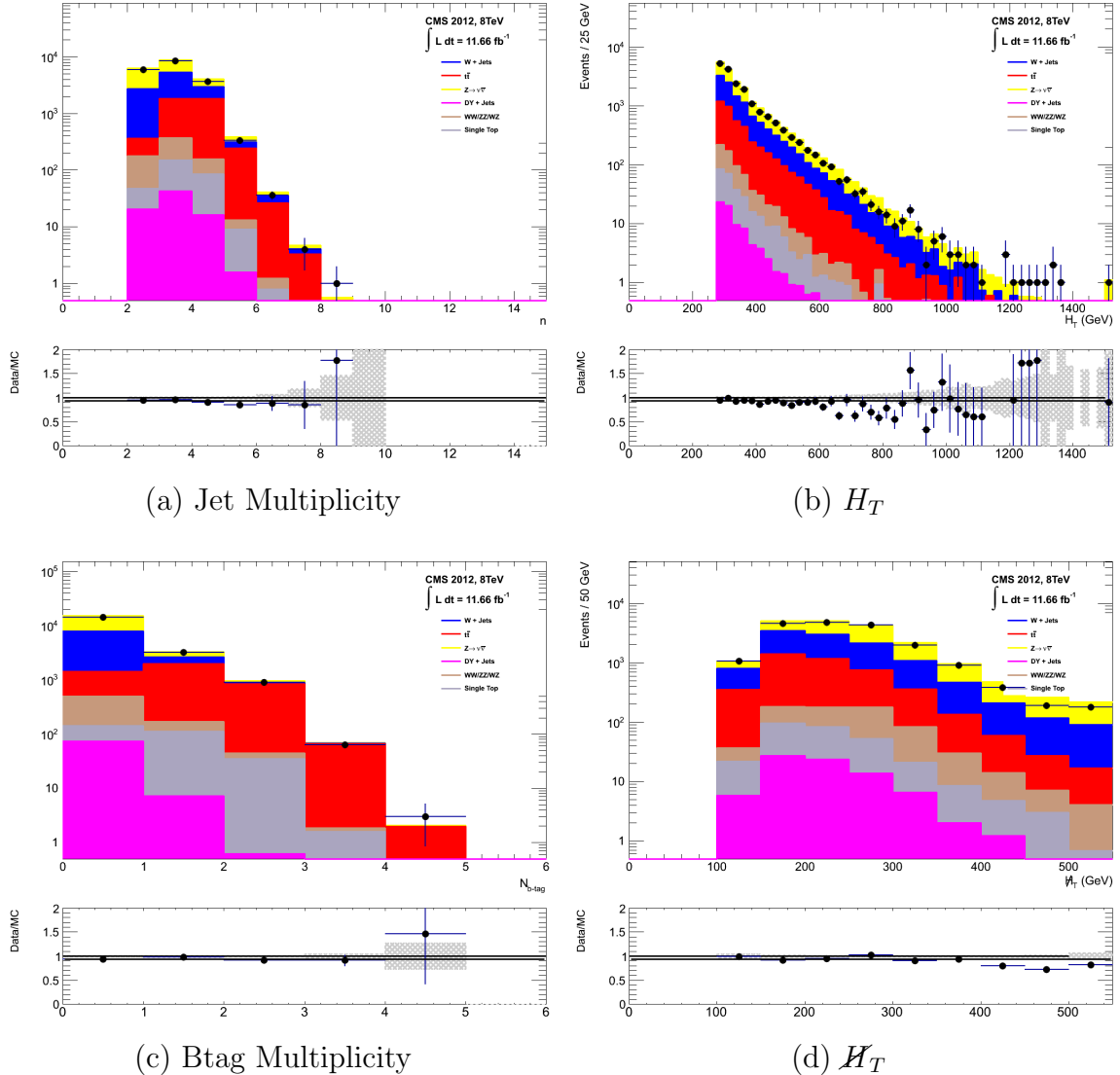


Figure 4.5.: DataMC comparisons of key variables for the hadronic signal region, following the application of the hadronic selection criteria and the requirements of $H_T > 275$ GeV and $\alpha_T > 0.55$. Bands represent the uncertainties due to the statistical size of the MC samples. No requirement is made upon the number of b-tagged jets or jet multiplicity in these distributions.

4.2.3. Control Sample Definition

The method used to estimate the background contributions in the hadronic signal region relies on the use of a Transfer Factor (TF). This is determined from MC simulation in both the control, N_{MC}^{control} , and signal, N_{MC}^{signal} , region to transform the observed yield measured in data for a control sample, $N_{\text{obs}}^{\text{control}}$, into a background prediction, $N_{\text{pred}}^{\text{signal}}$, via Equation (4.7),

$$N_{\text{pred}}^{\text{signal}} = \frac{N_{\text{MC}}^{\text{signal}}}{N_{\text{MC}}^{\text{control}}} \times N_{\text{obs}}^{\text{control}}. \quad (4.7)$$

1227 All MC samples are normalised to the luminosity of the data samples, 11.7 fb^{-1} .
1228 Through this method, “vanilla” predictions for the **SM** background in the signal region
1229 can be made by considering separately the sum of the prediction from either the $\mu + \text{jets}$
1230 and $\gamma + \text{jets}$ or $\mu + \text{jets}$ and $\mu\mu + \text{jets}$ samples. However the final background estimation
1231 from which results are interpreted, is calculated via a fitting procedure defined formally
1232 by the likelihood model described in Chapter 5.

1233 The sum of the expected yields from all MC processes, in each control sample enter
1234 the denominator, $N_{\text{MC}}^{\text{control}}$, of the **TF** defined in Eq (4.7). However for the numerator
1235, $N_{\text{MC}}^{\text{signal}}$, only the relevant processes that the control sample is used in estimating a
1236 background for, enter into the **TF**.

1237 For the $\mu + \text{jets}$ sample the simulated MC processes which enter the numerator of
1238 the **TF** are,

$$N_{\text{MC}}^{\text{signal}}(H_T, n_{\text{jet}}) = N_W + N_{t\bar{t}} + N_{DY} + N_t + N_{di-boson}, \quad (4.8)$$

1239 whilst for both the $\mu\mu + \text{jets}$ and $\gamma + \text{jets}$ samples the only MC process used in the
1240 numerator is,

$$N_{\text{MC}}^{\text{signal}}(H_T, n_{\text{jet}}) = N_{Z \rightarrow \nu\bar{\nu}}. \quad (4.9)$$

1241 The control samples and the **EWK** processes they are specifically tuned to select
1242 are defined below, with distributions of key variables for each of the control samples
1243 shown for illustrative purposes in Figures 4.6, 4.7 and 4.8. No requirement is placed
1244 upon the number of b-tagged jets or jet multiplicity in the distributions shown. The
1245 MC distributions highlight the background compositions of each control sample, where
1246 in general, good agreement is observed between data and simulation, giving confidence

1247 that the samples are well understood. The contribution from QCD multi-jet events is
1248 expected to be negligible :

1249 **The $\mu +$ jets control sample**

1250 Events from $W +$ jets and $t\bar{t}$ processes enter into the hadronic signal sample due to
1251 unidentified leptons from acceptance or threshold effects and hadronic tau decays.
1252 These leptons originate from the decay of high p_T W bosons.

1253 The control samples specifically identifies $W \rightarrow \mu\bar{\nu}$ decays within the same phase-
1254 space of the signal region, where the muon is subsequently ignored in the calculation
1255 of event level variables, i.e. H_T , \mathcal{H}_T , α_T . All kinematic jet-based cuts are identical
1256 to those applied in the hadronic search region detailed in Section (4.2.2), with the
1257 same H_T , jet multiplicity and b-jet multiplicity binning described above.

- 1258 – Muons originating from W boson decays are selected by requiring one tightly
1259 isolated muon defined in Table 4.3, with a $p_T > 30$ GeV and $|\eta| < 2.1$. Both of
1260 these threshold arise from trigger restrictions.
- 1261 – The transverse mass of the W candidate must satisfy $M_T(\mu, \cancel{E}_T) < 30$ GeV (to
1262 suppress QCD multi-jet events).
- 1263 – Events which contain a jet overlapping with a muon $\Delta R(\mu, \text{jet}) < 0.5$ are vetoed
1264 to remove events from muons produced as part of a jet’s hadronisation process.
- 1265 – Events containing a second muon candidate which has failed id, but passed p_T
1266 and $|\eta|$ requirements, are checked to have an invariant mass that satisfies $m_Z - 25 < M_{\mu_1\mu_2} > m_Z + 25$, thus removing $Z \rightarrow \mu\mu$ contamination.

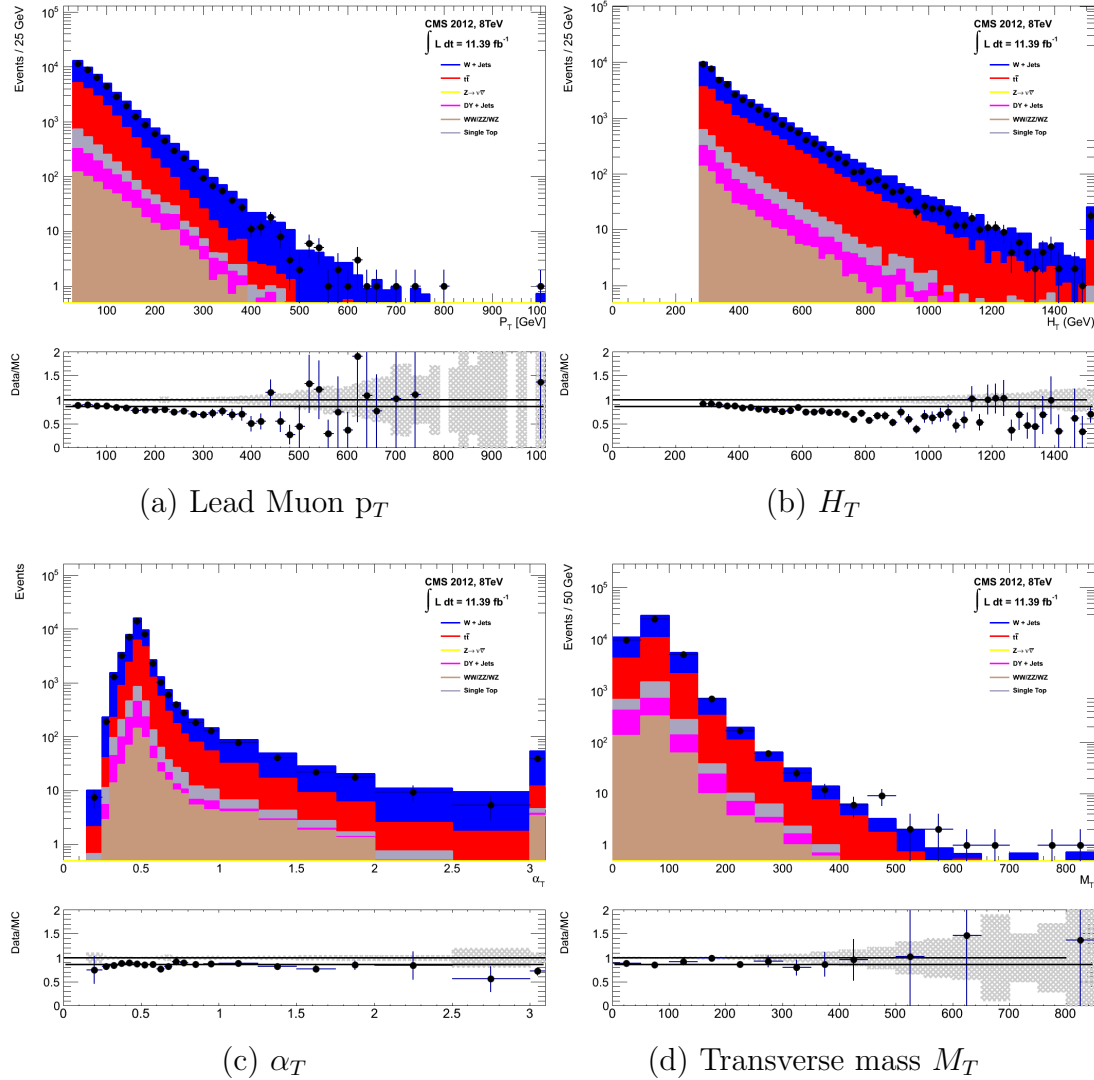


Figure 4.6.: DataMC comparisons of key variables for the $\mu + \text{jets}$ selection, following the application of selection criteria and the requirements that $H_T > 275$ GeV. Bands represent the uncertainties due to the statistical size of the MC samples. No requirement is made upon the number of b-tagged jets or jet multiplicity in these distributions.

The $\mu\mu + \text{jets}$ control sample

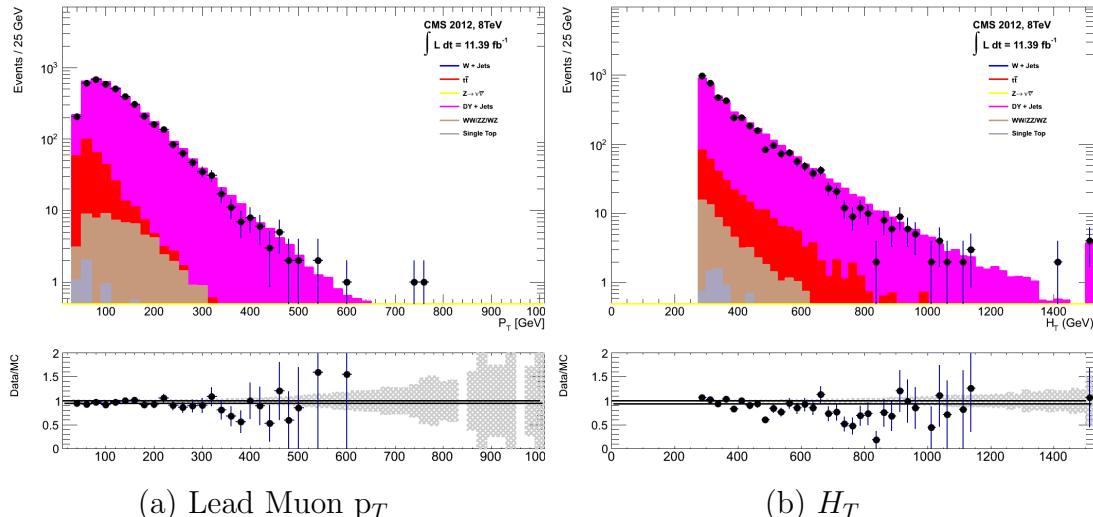
The $Z \rightarrow \nu\bar{\nu} + \text{jets}$ background enters into the signal region from genuine E_T from the escaping neutrinos. This background is estimated using two control samples, the first of which is the $Z \rightarrow \mu\bar{\mu} + \text{jets}$ process, which posses identical kinematic properties, but with different acceptance and branching ratio [1].

The same acceptance requirements as the $\mu + \text{jets}$ selection for muons is applied, as defined in Table 4.3. Muons in the event are ignored for the purpose of the

calculation of event level variables. Kinematic jet-based cuts and phase space binning identical to the hadronic search region are also applied.

- Muons origination from a Z boson decay are selected requiring exactly two tightly isolated muons. Due to trigger requirements the leading muon is required to have $p_T > 30$ GeV and $|\eta| < 2.1$. The requirement of the p_T on the second muon is relaxed to 10 GeV.
- Events are vetoed if containing a jet overlapping with a muon $\Delta R(\mu, \text{jet}) < 0.5$.
- In order to specifically select two muons both originating from a single Z boson decay, the invariant mass of the two muons must satisfy $m_Z - 25 > M_{\mu_1\mu_2} < m_Z + 25$.

The $\mu\mu + \text{jets}$ sample is used to make predictions in the signal region in the two lowest H_T bins, providing coverage where the $\gamma + \text{jets}$ sample is unable to, due to trigger requirements. In higher H_T bins, the higher statistics of the $\gamma + \text{jets}$ sample is instead used to determine the $Z \rightarrow \nu\bar{\nu}$ estimation.



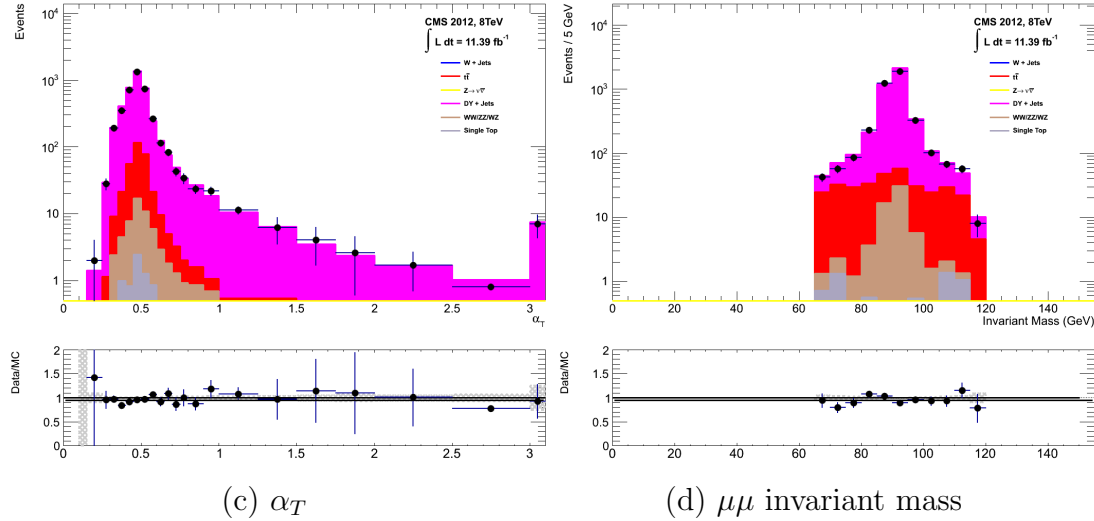


Figure 4.7.: DataMC comparisons of key variables for the $\mu\mu + \text{jets}$ selection, following the application of selection criteria and the requirements that $H_T > 275$ GeV. Bands represent the uncertainties due to the statistical size of the MC samples. No requirement is made upon the number of b-tagged jets or jet multiplicity in these distributions.

The $\gamma + \text{jets}$ control sample

The $Z \rightarrow \nu\bar{\nu} + \text{jets}$ background is also estimated from a $\gamma + \text{jets}$ control sample, which possesses a larger cross section and kinematic properties similar to those of $Z \rightarrow \mu\bar{\mu}$ events where the photon is ignored [78][79]. The photon is ignored for the purpose of the calculation of event level variables, and identical selection cuts to the hadronic signal region are applied.

- Exactly one photon is selected, satisfying identification criteria as detailed in Table 4.4, with a minimum $p_T > 165$ GeV to satisfy trigger thresholds and $|\eta| < 1.45$ to ensure the photon remains in the barrel of the detector.
- A selection criteria of $\Delta R(\gamma, \text{jet}) < 1.0$, between the photon and all jets is applied to ensure the acceptance of only well isolated $\gamma + \text{jets}$ events.
- Given that the photon is ignored, this control sample can only be applied in the H_T region > 375 GeV, due to the trigger thresholds on the minimum p_T of the photon, and the H_T requirement of an $\alpha_T > 0.55$ cut from Equation (4.5).

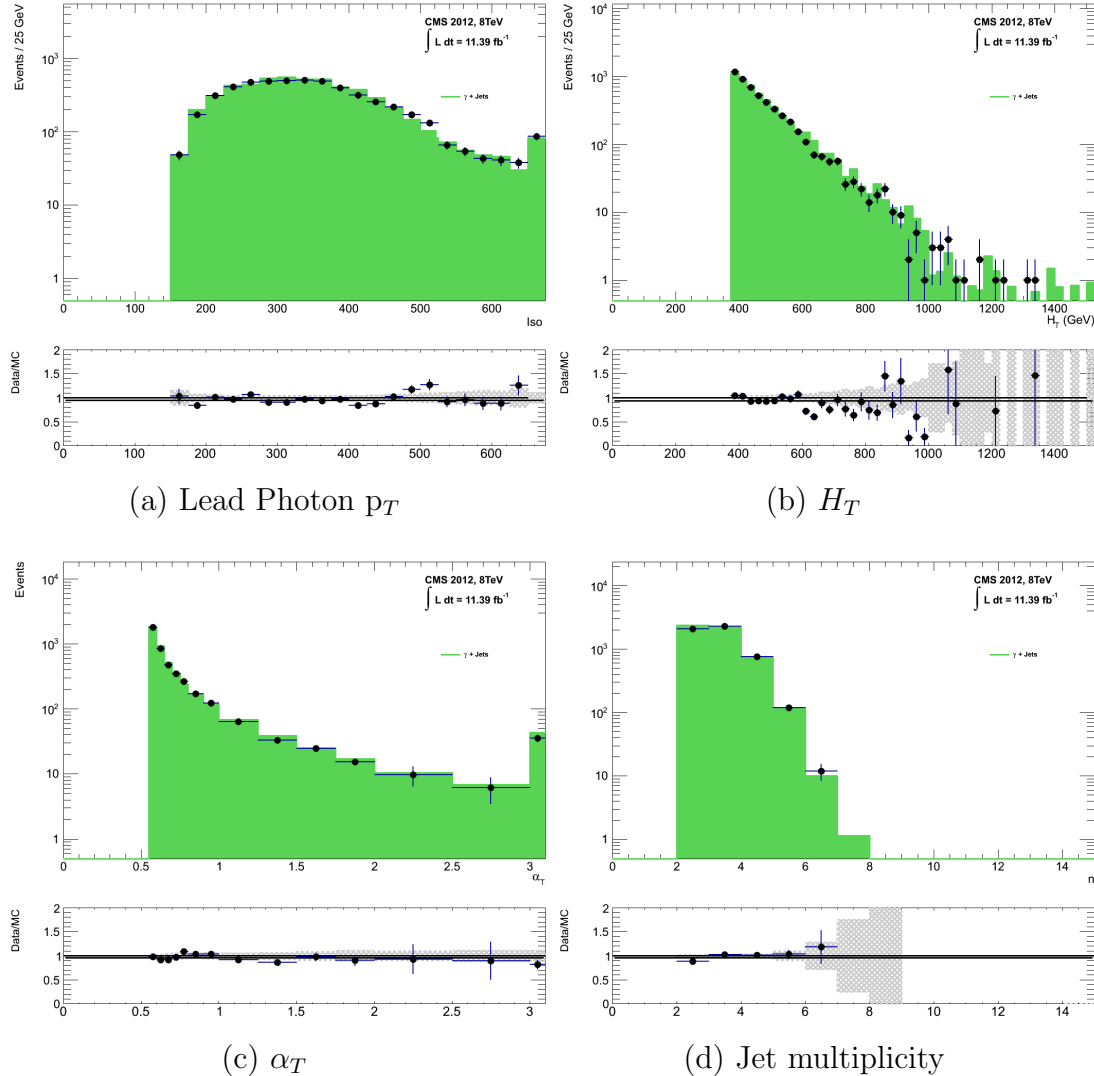


Figure 4.8.: DataMC comparisons of key variables for the $\gamma + \text{jets}$ selection, following the application of selection criteria and the requirements that $H_T > 375 \text{ GeV}$ and $\alpha_T > 0.55$. Bands represent the uncertainties due to the statistical size of the MC samples. No requirement is made upon the number of b-tagged jets or jet multiplicity in these distributions.

The selection criteria of the three control samples are defined to ensure background composition and event kinematics mirror closely the signal region. This is done in order to minimise the reliance on MC simulation to model correctly the backgrounds and event kinematics in the control and signal samples.

However in the case of the $\mu + \text{jets}$ and $\mu\mu + \text{jets}$ samples, the α_T requirement is relaxed in the selection criteria of these samples. This is made possible as contamination from QCD multi-jet events is suppressed to a negligible level by the other kinematic selection criteria within the two control samples, to select pure EWK processes. Thus in

1316 this way, the acceptance of the two muon control samples can be significantly increased,
1317 which simultaneously improves their predictive power and further reduces the effect of
1318 any potential signal contamination.

1319 The modelling of the α_T variable is probed through a dedicated set of closure tests,
1320 described in Section (4.6), which demonstrate that the different α_T acceptances for the
1321 control and signal samples have no significant systematic bias on the prediction.

1322 **4.2.4. Estimating the QCD background multi-jet background**

1323 A negligible background from QCD multi-jet events within the hadronic signal region
1324 is expected due to the selection requirement, and additional cleaning filters applied.
1325 However a conservative approach is still adopted and the likelihood model.

1326 **4.3. Trigger Strategy**

1327 A cross trigger based on the quantities H_T and α_T , labelled is used with varying thresholds
1328 across H_T bins to record the event sample for the hadronic signal region. The α_T legs
1329 of the H_T - α_T triggers used in the analysis are chosen to fully suppress QCD multi-jet
1330 events, whilst maintaining a sustainable trigger rate.

₁₃₃₁ **4.4. A method to determine MC yields with higher
₁₃₃₂ statistical precision**

₁₃₃₃ **4.5. Measuring MC normalisation factors via H_T
₁₃₃₄ sidebands**

₁₃₃₅ **4.6. Systematic Uncertainties on Transfer Factors**

₁₃₃₆ **4.7. Searches for Natural SUSY with B-tag
₁₃₃₇ templates.**

₁₃₃₈ Btag Templates blah blah

Chapter 5.

¹³³⁹ Results

¹³⁴⁰ Results at 12fb 8TeV

¹³⁴¹ 5.1. Statistical Interpretation

¹³⁴² Likelihood stuff

¹³⁴³ 5.2. Interpretation in Simplified Signal Models

¹³⁴⁴ Result interpretation

¹³⁴⁵

Appendix A.

¹³⁴⁶ Miscellaneous

¹³⁴⁷ A.1. Noise Filters

¹³⁴⁸ For Calo jets the following criteria were applied:

¹³⁴⁹ • N90 hits > 1 ,

¹³⁵⁰ • HBHE > 0.01 ,

¹³⁵¹ • fHPD < 0.98 ,

¹³⁵² For PF jets the following criteria were applied:

¹³⁵³ • Neutral hadron fraction < 0.99 ,

¹³⁵⁴ • Neutral EM fraction < 0.99 ,

¹³⁵⁵ • Number of constituents > 1 ,

¹³⁵⁶ • Charged hadron fraction > 0 ,

¹³⁵⁷ • Charged multiplicity > 0 ,

¹³⁵⁸ • Charged EM fraction < 0.99 .

¹³⁵⁹ The following noise filters are applied, to remove events with spurious, non-physical
¹³⁶⁰ jets or missing transverse energy.

¹³⁶¹ • CSC tight beam halo filter,

¹³⁶² • HBHE noise filter with isolated noise rejection,

- 1363 • HCAL laser filter,
- 1364 • ECAL dead cell trigger primitive (TP) filter,
- 1365 • Tracking failure filter,
- 1366 • Bad EE Supercrystal filter,
- 1367 • ECAL Laser correction filter.

1368 A.2. Primary Vertices

1369 The pileup per event is defined by the number of 'good' reconstructed primary vertices
1370 in the event, with each vertex satisfying the following requirements

- 1371 • $N_{dof} > 4$;
- 1372 • vertex position along the bead direction of $|z_{vtx}| < 24\text{cm}$;
- 1373 • vertex position perpendicular to the beam of $\rho < 2\text{cm}$.

Appendix B.

¹³⁷⁴ L1 Jets

¹³⁷⁵ B.1. Jet matching efficiencies

¹³⁷⁶ The single jet turn-on curves are derived from events independent of whether the leading
¹³⁷⁷ jet in an event is matched to a Level 1 jet using ΔR matching detailed in Section (3.4.3)
¹³⁷⁸ or not. These turn-ons are produced from events which are not triggered on jet quantities
¹³⁷⁹ and therefore it is not guaranteed that the lead jet of an event will be seeded by a Level
¹³⁸⁰ 1 jet. Figure B.1 shows the particular matching efficiency of a lead jet to a L1 jet.

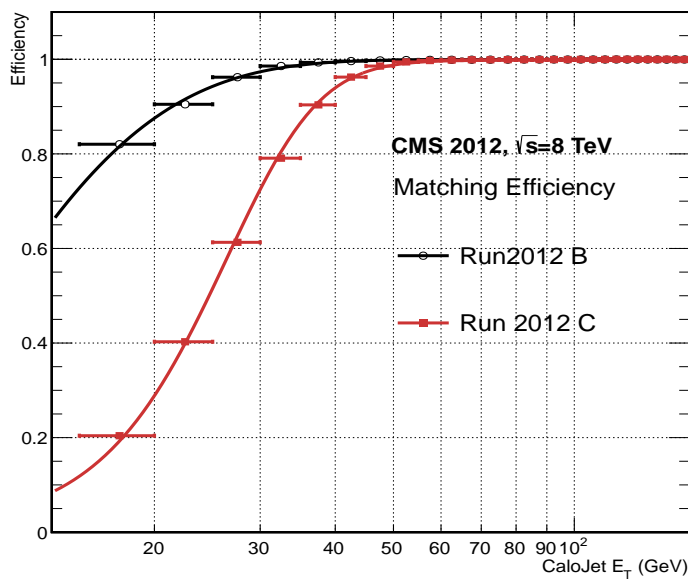


Figure B.1.: Leading jet matching efficiency as a function of the offline CaloJet E_T , measured in an isolated muon triggered dataset in the 2012B and 2012C run periods.

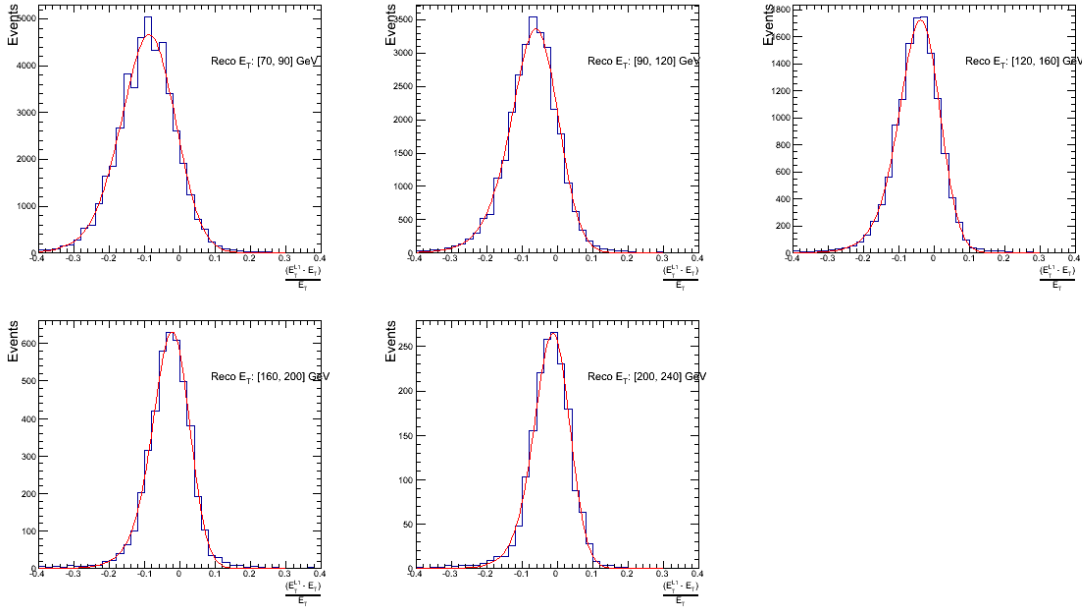
Run Period	μ	σ
2012B	6.62 ± 0.01	0.79 ± 0.03
2012C	19.51 ± 0.03	7.14 ± 0.02

Table B.1.: Results of a cumulative EMG function fit to the turn-on curves for the matching efficiency of the leading jet in an event to a Level-1 jet in run 2012C and 2012B data, measured in an isolated muon triggered sample. The turn-on point, μ , and resolution, σ , are measured with respect to offline Calo Jet E_T .

It can be seen that the turn on is sharper during the 2012B run period. The seed threshold requirement of a 5 GeV jet seed in run 2012C results in more events in which even the lead offline jet does not have an associated L1 jet. For larger jet E_T thresholds, typical of thresholds used in physics analyses, 100% efficiency is observed.

The matching efficiencies have a μ values of 6.62 GeV and 19.51 GeV for Run 2012B and 2012C respectively and is shown in Table B.1.

B.2. Leading Jet Energy Resolution



(a)

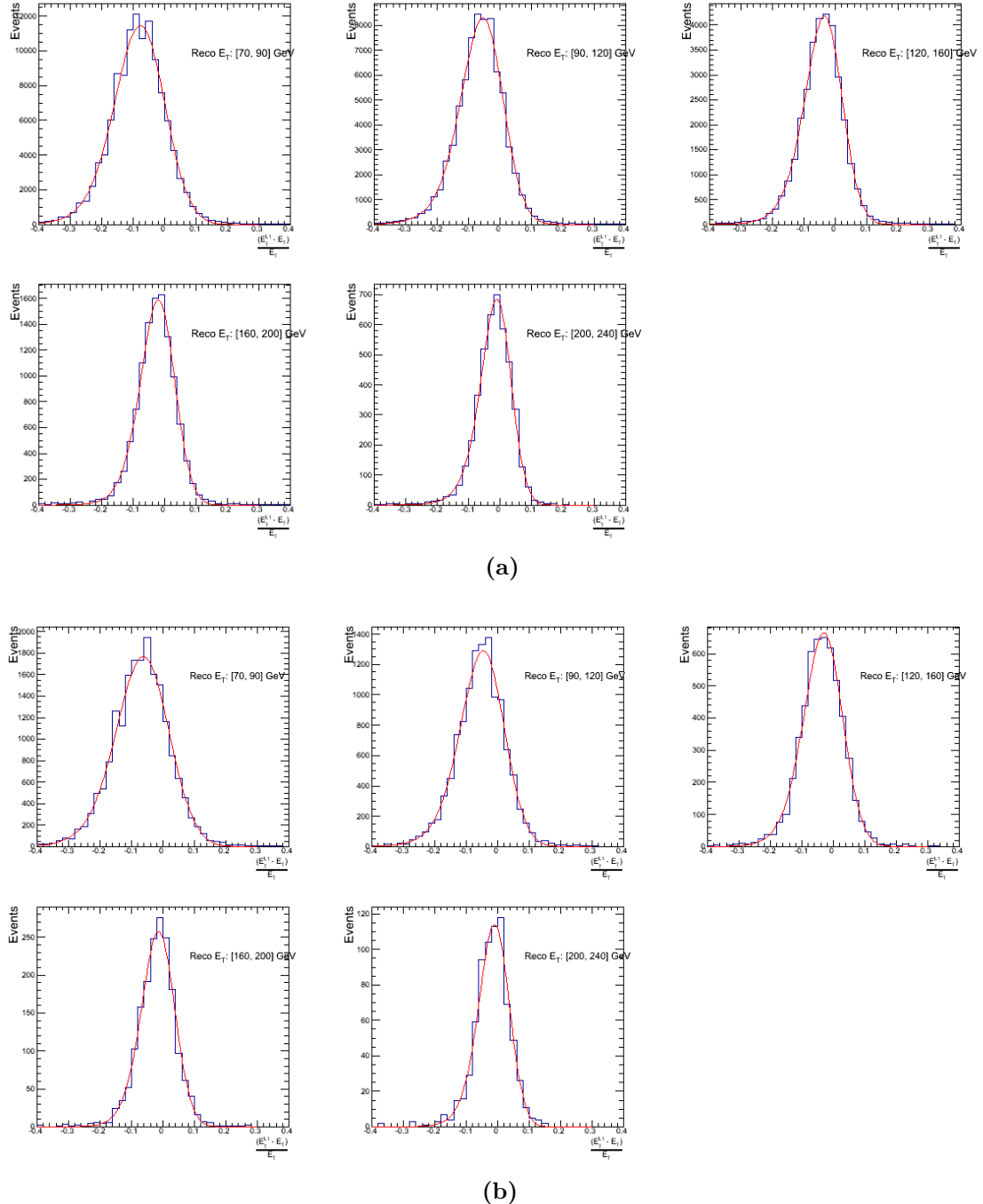
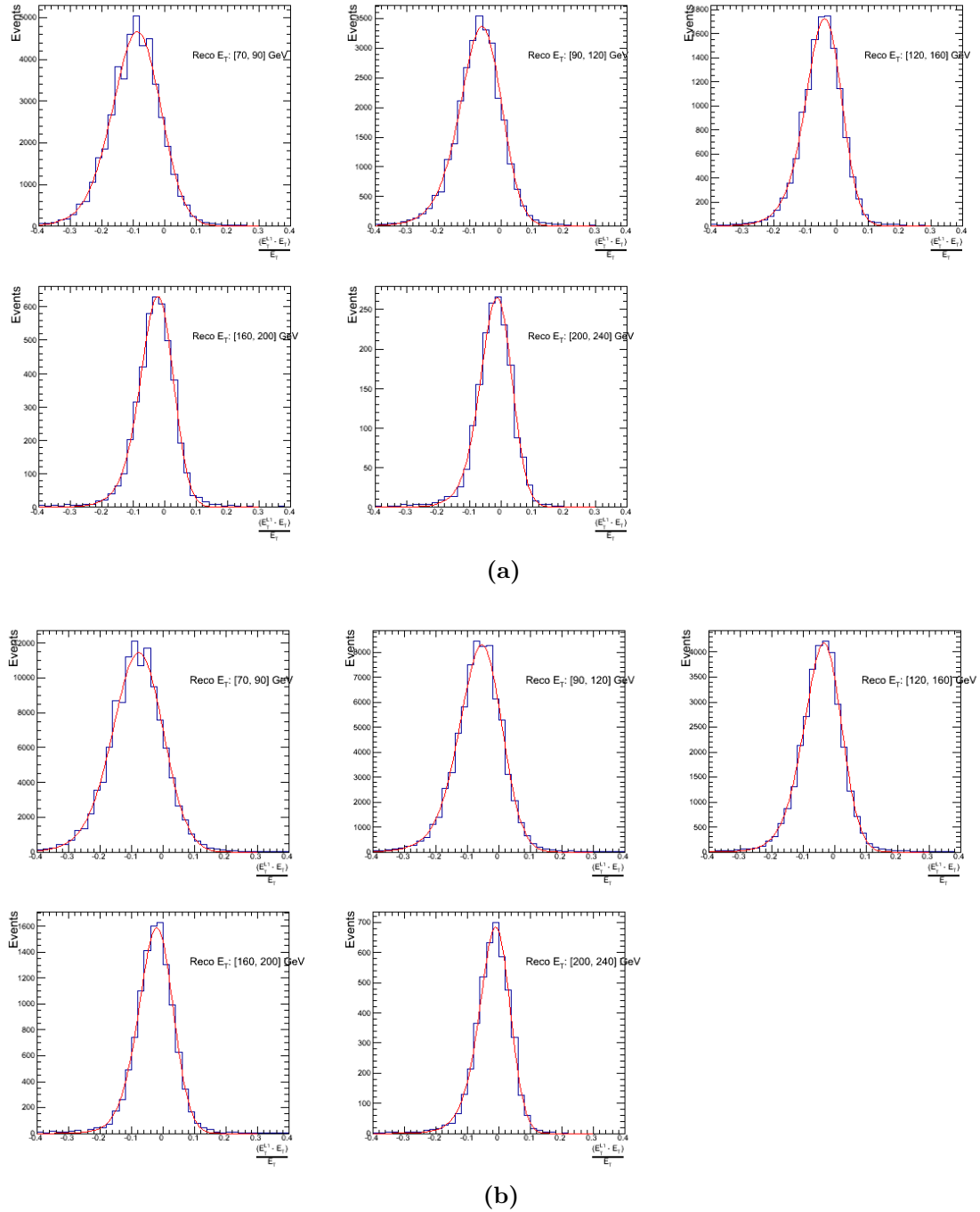
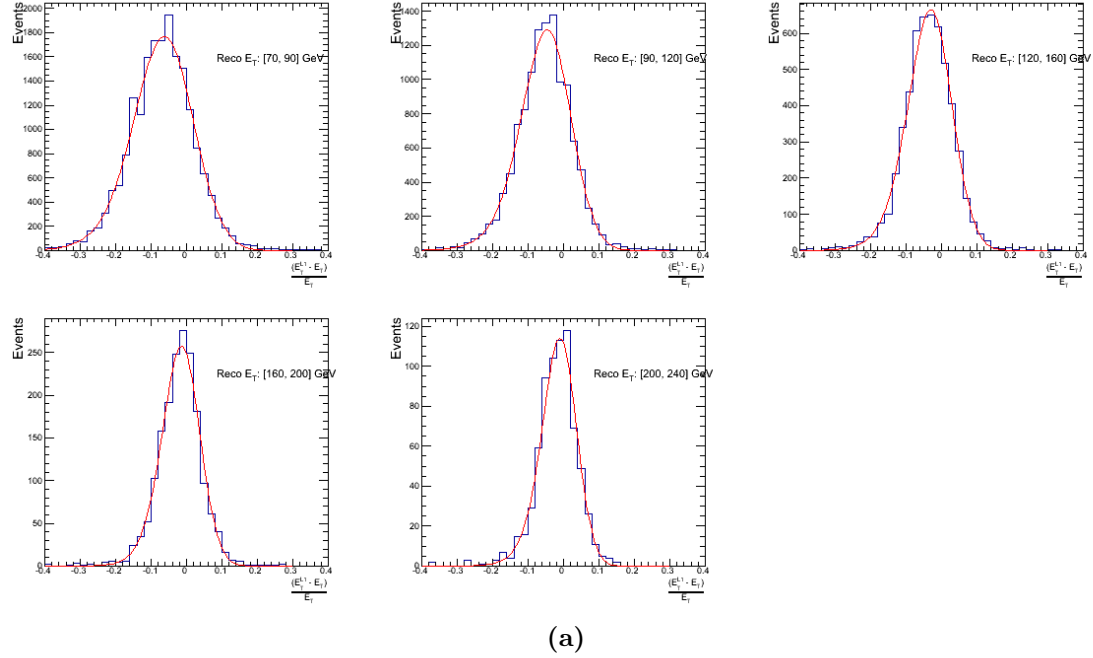


Figure B.2.: Resolution plots of the leading offline jet Calo E_T measured as a function of $\frac{(\text{L1 } E_T - \text{Offline } E_T)}{\text{Offline } E_T}$ for low (a), medium (b) and high (c) pile-up conditions.





(a)

Figure B.3.: Resolution plots of the leading offline jet PF E_T measured as a function of $\frac{(L1 E_T - Offline E_T)}{Offline E_T}$ for low (a), medium (b) and high (c) pile-up conditions.

1388 B.3. Resolution for Energy Sum Quantities

1389 The following plots show the resolution parameters for the four energy sum quantities as
 1390 a function of the quantity (q) itself. In this case, The mean and RMS of the individual
 1391 $\frac{(L1 q - Offline q)}{Offline q}$ distributions, in bins of the quantity q is displayed.

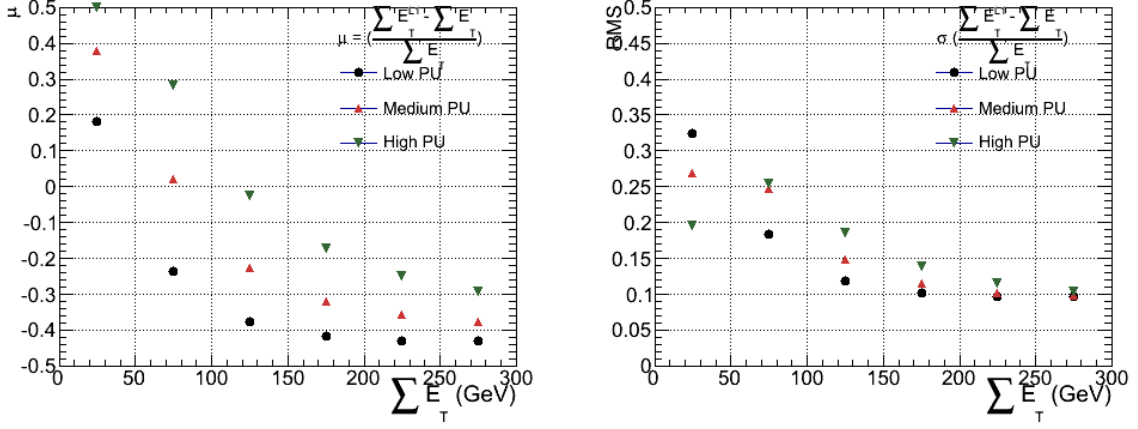


Figure B.4.: $\sum E_T$ resolution parameters in bins of Calo $\sum E_T$ measured for the defined low, medium and high pile up conditions. The plots show the mean μ (left), resolution σ (RMS) of the $\frac{\Delta q}{q}$ distributions.

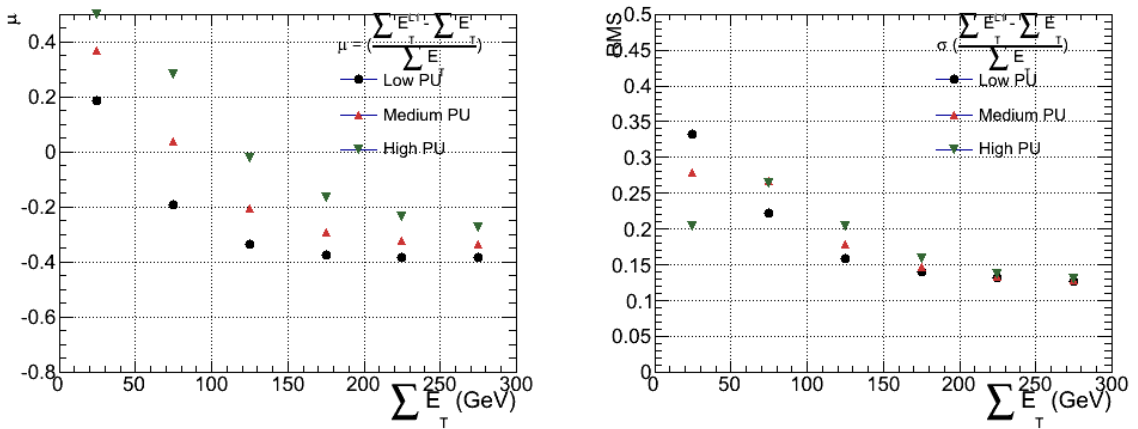


Figure B.5.: $\sum E_T$ resolution parameters in bins of PF $\sum E_T$ measured for the defined low, medium and high pile up conditions. The plots show the mean μ (left), resolution σ (RMS) of the $\frac{\Delta q}{q}$ distributions.

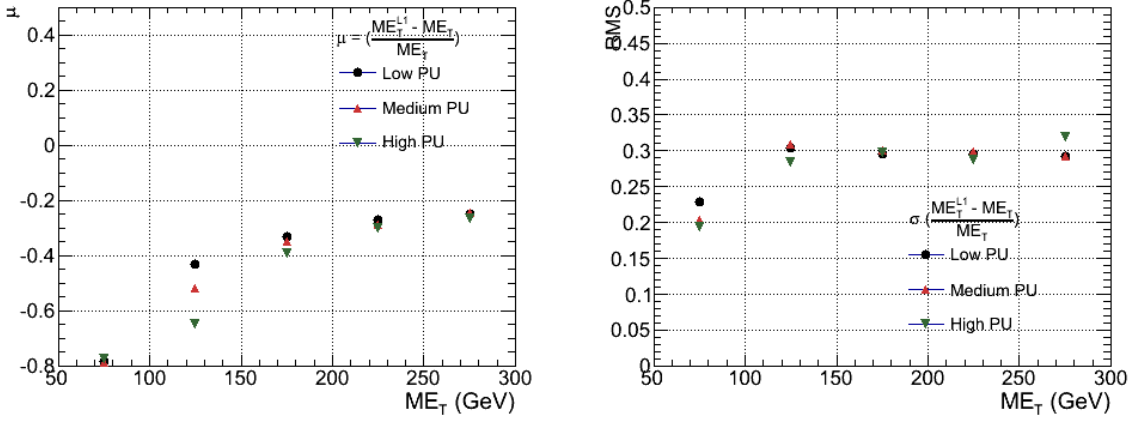


Figure B.6.: \mathcal{E}_T resolution parameters in bins of Calo \mathcal{E}_T measured for the defined low, medium and high pile up conditions. The plots show the mean μ (left), resolution σ (RMS) of the $\frac{\Delta q}{q}$ distributions.

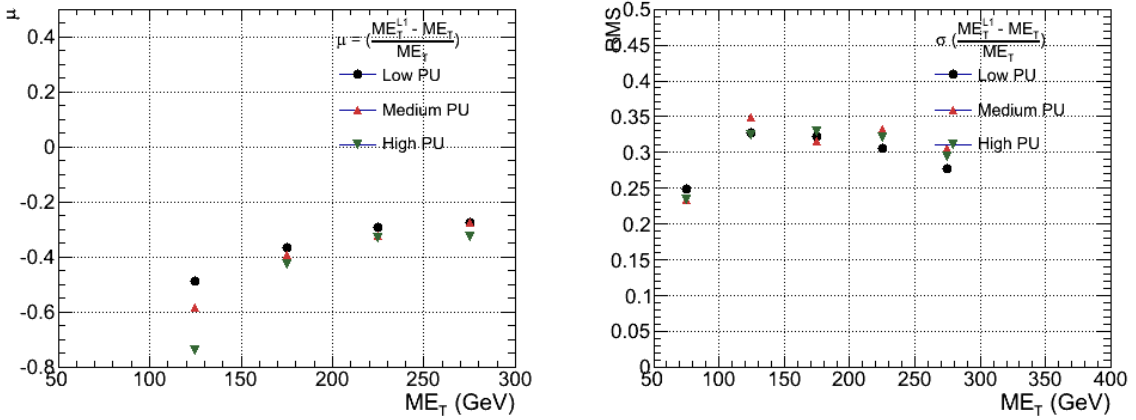


Figure B.7.: \mathcal{E}_T resolution parameters in bins of PF \mathcal{E}_T measured for the defined low, medium and high pile up conditions. The plots show the mean μ (left), resolution σ (RMS) of the $\frac{\Delta q}{q}$ distributions.

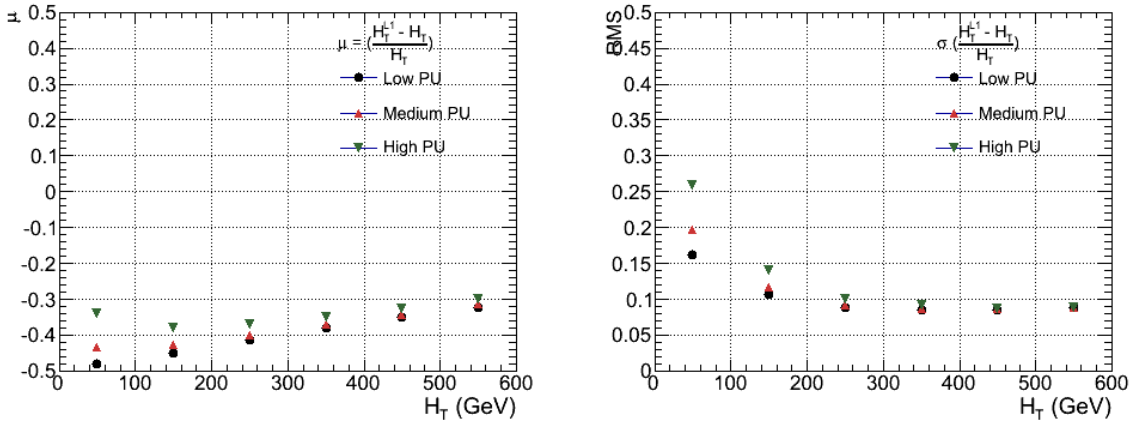


Figure B.8.: H_T resolution parameters in bins of Calo H_T measured for the defined low, medium and high pile up conditions. The plots show the mean μ (left), resolution σ (RMS) of the $\frac{\Delta q}{q}$ distributions.

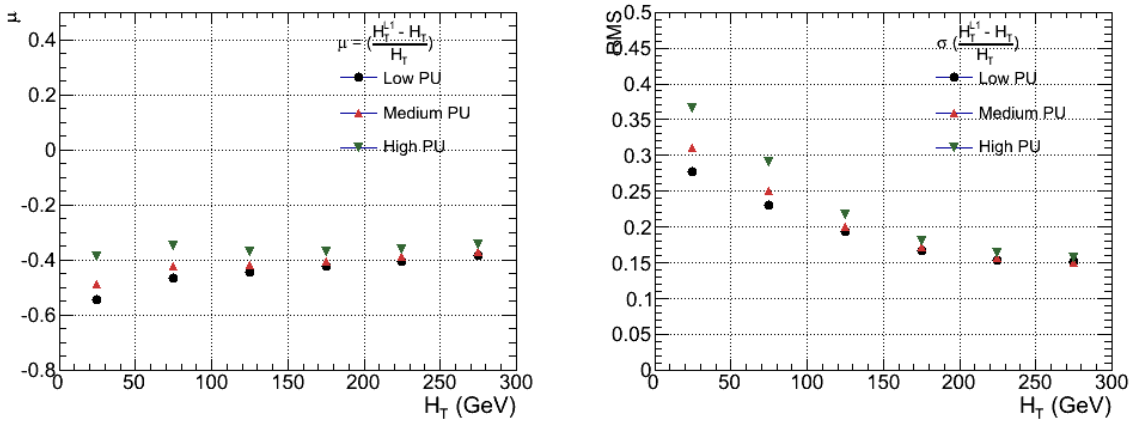


Figure B.9.: H_T resolution parameters in bins of PF H_T measured for the defined low, medium and high pile up conditions. The plots show the mean μ (left), resolution σ (RMS) of the $\frac{\Delta q}{q}$ distributions.

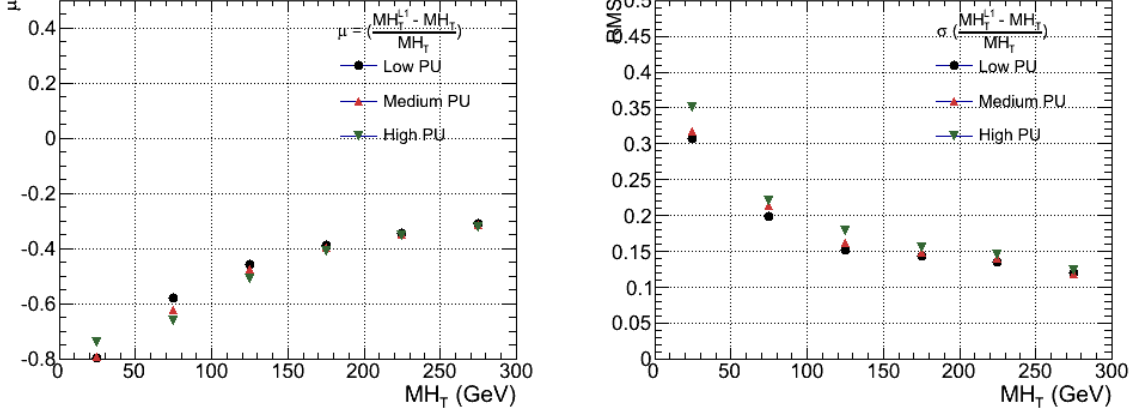


Figure B.10.: H_T resolution parameters in bins of H_T measured for the defined low, medium and high pile up conditions. The plots show the mean μ (left), resolution σ (RMS) of the $\frac{\Delta q}{q}$ distributions.

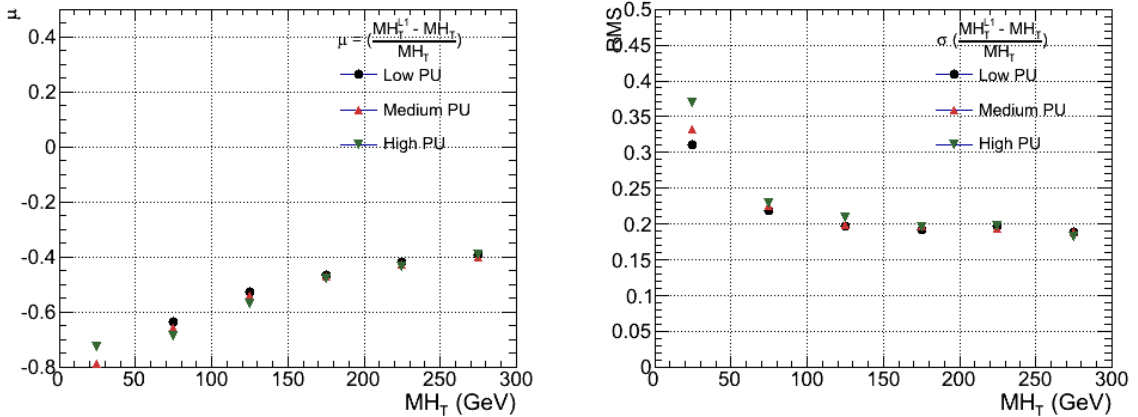


Figure B.11.: H_T resolution parameters in bins of PF H_T measured for the defined low, medium and high pile up conditions. The plots show the mean μ (left), resolution σ (RMS) of the $\frac{\Delta q}{q}$ distributions.

¹³⁹³ Bibliography

- ¹³⁹⁴ [1] J. Beringer *et al.*, “Review of Particle Physics (RPP),” *Phys.Rev.*, vol. D86, p. 010001, 2012.
- ¹³⁹⁵ [2] G. H. et al., “Nine-year wilkinson microwave anisotropy probe (wmap) observations: Cosmological parameter results,” *The Astrophysical Journal Supplement Series*, vol. 208, no. 2, p. 19, 2013.
- ¹³⁹⁶ [3] G. Aad *et al.*, “Observation of a new particle in the search for the Standard Model Higgs boson with the ATLAS detector at the LHC,” *Phys.Lett.*, vol. B716, pp. 1–29, 2012.
- ¹³⁹⁷ [4] S. Chatrchyan *et al.*, “Observation of a new boson at a mass of 125 GeV with the CMS experiment at the LHC,” *Phys.Lett.*, vol. B716, pp. 30–61, 2012.
- ¹³⁹⁸ [5] S. Chatrchyan *et al.*, “Search for supersymmetry in hadronic final states with missing transverse energy using the variables AlphaT and b-quark multiplicity in pp collisions at 8 TeV,” *Eur.Phys.J.*, vol. C73, p. 2568, 2013.
- ¹³⁹⁹ [6] S. Weinberg, “A model of leptons,” *Phys. Rev. Lett.*, vol. 19, pp. 1264–1266, Nov 1967.
- ¹⁴⁰⁰ [7] S. Glashow, “Partial Symmetries of Weak Interactions,” *Nucl.Phys.*, vol. 22, pp. 579–588, 1961.
- ¹⁴⁰¹ [8] A. Salam, “Weak and Electromagnetic Interactions,” *Conf.Proc.*, vol. C680519, pp. 367–377, 1968.
- ¹⁴⁰² [9] G. Hooft, “Renormalizable lagrangians for massive yang-mills fields,” *Nuclear Physics B*, vol. 35, no. 1, pp. 167 – 188, 1971.
- ¹⁴⁰³ [10] F. Hasert *et al.*, “Observation of Neutrino Like Interactions Without Muon Or Electron in the Gargamelle Neutrino Experiment,” *Phys.Lett.*, vol. B46, pp. 138–140, 1973.

- [11] G. Arnison *et al.*, “Experimental Observation of Lepton Pairs of Invariant Mass Around 95-GeV/c**2 at the CERN SPS Collider,” *Phys.Lett.*, vol. B126, pp. 398–410, 1983.
- [12] M. Banner *et al.*, “Observation of Single Isolated Electrons of High Transverse Momentum in Events with Missing Transverse Energy at the CERN anti-p p Collider,” *Phys.Lett.*, vol. B122, pp. 476–485, 1983.
- [13] E. Noether, “Invariante variationsprobleme,” *Nachrichten von der Gesellschaft der Wissenschaften zu Gttingen, Mathematisch-Physikalische Klasse*, vol. 1918, pp. 235–257, 1918.
- [14] F. Halzen and A. D. Martin, “Quarks and leptons.” Wiley, 1985.
- [15] *Introduction to Elementary Particles*. Wiley-VCH, 2nd ed., Oct. 2008.
- [16] C. S. Wu, E. Ambler, R. W. Hayward, D. D. Hoppes, and R. P. Hudson, “Experimental Test of Parity Conservation in Beta Decay,” *Physical Review*, vol. 105, pp. 1413–1415, Feb. 1957.
- [17] P. Higgs, “Broken symmetries, massless particles and gauge fields,” *Physics Letters*, vol. 12, no. 2, pp. 132 – 133, 1964.
- [18] F. Englert and R. Brout, “Broken symmetry and the mass of gauge vector mesons,” *Phys. Rev. Lett.*, vol. 13, pp. 321–323, Aug 1964.
- [19] P. W. Higgs, “Broken symmetries and the masses of gauge bosons,” *Phys. Rev. Lett.*, vol. 13, pp. 508–509, Oct 1964.
- [20] G. S. Guralnik, C. R. Hagen, and T. W. B. Kibble, “Global conservation laws and massless particles,” *Phys. Rev. Lett.*, vol. 13, pp. 585–587, Nov 1964.
- [21] S. Weinberg, “A model of leptons,” *Phys. Rev. Lett.*, vol. 19, pp. 1264–1266, Nov 1967.
- [22] H. Yukawa, “On the interaction of elementary particles. i,” *Progress of Theoretical Physics Supplement*, vol. 1, pp. 1–10, 1955.
- [23] Y. e. a. Fukuda, “Evidence for oscillation of atmospheric neutrinos,” *Phys. Rev. Lett.*, vol. 81, pp. 1562–1567, Aug 1998.
- [24] R. Becker-Szendy, C. Bratton, D. Casper, S. Dye, W. Gajewski, *et al.*, “A Search for muon-neutrino oscillations with the IMB detector,” *Phys.Rev.Lett.*, vol. 69,

- ¹⁴⁴⁸ pp. 1010–1013, 1992.
- ¹⁴⁴⁹ [25] S. P. Martin, “A Supersymmetry primer,” 1997.
- ¹⁴⁵⁰ [26] H. Nilles, *Supersymmetry, Supergravity and Particle Physics*. Physics reports, North-Holland Physics Publ., 1984.
- ¹⁴⁵² [27] H. E. Haber and G. L. Kane, “The Search for Supersymmetry: Probing Physics Beyond the Standard Model,” *Phys.Rept.*, vol. 117, pp. 75–263, 1985.
- ¹⁴⁵⁴ [28] E. Witten, “Dynamical Breaking of Supersymmetry,” *Nucl.Phys.*, vol. B188, p. 513, 1981.
- ¹⁴⁵⁶ [29] J. Wess and B. Zumino, “Supergauge transformations in four dimensions,” *Nuclear Physics B*, vol. 70, no. 1, pp. 39 – 50, 1974.
- ¹⁴⁵⁸ [30] H. Muller-Kirsten and A. Wiedemann, *Introduction to Supersymmetry*. World Scientific lecture notes in physics, World Scientific, 2010.
- ¹⁴⁶⁰ [31] I. Aitchison, *Supersymmetry in Particle Physics: An Elementary Introduction*. Cambridge University Press, 2007.
- ¹⁴⁶² [32] K. A. Intriligator and N. Seiberg, “Lectures on Supersymmetry Breaking,” *Class.Quant.Grav.*, vol. 24, pp. S741–S772, 2007.
- ¹⁴⁶⁴ [33] Y. Shadmi, “Supersymmetry breaking,” pp. 147–180, 2006.
- ¹⁴⁶⁵ [34] C. Burgess, P. G. Camara, S. de Alwis, S. Giddings, A. Maharana, *et al.*, “Warped Supersymmetry Breaking,” *JHEP*, vol. 0804, p. 053, 2008.
- ¹⁴⁶⁷ [35] H. Murayama, “Supersymmetry breaking made easy, viable, and generic,” 2007.
- ¹⁴⁶⁸ [36] H. Baer and X. Tata, *Weak Scale Supersymmetry: From Superfields to Scattering Events*. Cambridge University Press, 2006.
- ¹⁴⁷⁰ [37] S. P. Martin, “Implications of supersymmetric models with natural r-parity conservation,” 1996.
- ¹⁴⁷² [38] G. L. Kane, C. F. Kolda, L. Roszkowski, and J. D. Wells, “Study of constrained minimal supersymmetry,” *Phys.Rev.*, vol. D49, pp. 6173–6210, 1994.
- ¹⁴⁷⁴ [39] C. Stlege, G. Bertone, D. Cerdeno, M. Fornasa, R. Ruiz de Austri, *et al.*, “Updated global fits of the cmSSM including the latest LHC SUSY and Higgs searches and XENON100 data,” *JCAP*, vol. 1203, p. 030, 2012.

- 1477 [40] M. Citron, J. Ellis, F. Luo, J. Marrouche, K. Olive, *et al.*, “The End of the CMSSM
1478 Coannihilation Strip is Nigh,” *Phys.Rev.*, vol. D87, p. 036012, 2013.
- 1479 [41] D. Ghosh, M. Guchait, S. Raychaudhuri, and D. Sengupta, “How Constrained is
1480 the cMSSM?,” *Phys.Rev.*, vol. D86, p. 055007, 2012.
- 1481 [42] D. Alves *et al.*, “Simplified Models for LHC New Physics Searches,” *J.Phys.*, vol. G39,
1482 p. 105005, 2012.
- 1483 [43] J. Alwall, P. Schuster, and N. Toro, “Simplified Models for a First Characterization
1484 of New Physics at the LHC,” *Phys.Rev.*, vol. D79, p. 075020, 2009.
- 1485 [44] S. Chatrchyan *et al.*, “Interpretation of Searches for Supersymmetry with simplified
1486 Models,” *Phys.Rev.*, vol. D88, p. 052017, 2013.
- 1487 [45] J. Hisano, K. Kurosawa, and Y. Nomura, “Natural effective supersymmetry,”
1488 *Nucl.Phys.*, vol. B584, pp. 3–45, 2000.
- 1489 [46] M. Papucci, J. T. Ruderman, and A. Weiler, “Natural SUSY Endures,” *JHEP*,
1490 vol. 1209, p. 035, 2012.
- 1491 [47] B. Allanach and B. Gripaios, “Hide and Seek With Natural Supersymmetry at the
1492 LHC,” *JHEP*, vol. 1205, p. 062, 2012.
- 1493 [48] K. Aamodt *et al.*, “The ALICE experiment at the CERN LHC,” *JINST*, vol. 3,
1494 p. S08002, 2008.
- 1495 [49] G. Aad *et al.*, “The ATLAS Experiment at the CERN Large Hadron Collider,”
1496 *JINST*, vol. 3, 2008.
- 1497 [50] R. Adolphi *et al.*, “The cms experiment at the cern lhc,” *JINST*, vol. 0803, p. S08004,
1498 2008.
- 1499 [51] A. A. Alves *et al.*, “The LHCb Detector at the LHC,” *JINST*, vol. 3, p. S08005,
1500 2008.
- 1501 [52] J.-L. Caron, “Lhc layout.. schema general du lhc..” Sep 1997.
- 1502 [53] C. Collaboration, “Cms luminosity - public results.”
1503 twiki.cern.ch/twiki/bin/view/CMSPublic/LumiPublicResults., 2011.
- 1504 [54] CERN, “Cms compact muon solenoid..” <http://public.web.cern.ch/public/Objects/LHC/CMSnc.jpg>
1505 Feb 2010.

- 1506 [55] *The CMS electromagnetic calorimeter project: Technical Design Report*. Technical
1507 Design Report CMS, Geneva: CERN, 1997.
- 1508 [56] *The CMS muon project: Technical Design Report*. Technical Design Report CMS,
1509 Geneva: CERN, 1997.
- 1510 [57] CMS Collaboration, “The cms physics technical design report, volume 1,”
1511 *CERN/LHCC*, vol. 2006-001, 2006.
- 1512 [58] M. Cacciari, G. P. Salam, and G. Soyez, “The anti- k_t jet clustering algorithm,”
1513 *Journal of High Energy Physics*, vol. 2008, no. 04, p. 063, 2008.
- 1514 [59] “Jet performance in pp collisions at 7 tev,” Tech. Rep. CMS-PAS-JME-10-003,
1515 CERN, Geneva, 2010.
- 1516 [60] X. Janssen, “Underlying event and jet reconstruction in cms,” Tech. Rep. CMS-CR-
1517 2011-012, CERN, Geneva, Jan 2011.
- 1518 [61] T. C. collaboration, “Determination of jet energy calibration and transverse mo-
1519 mentum resolution in cms,” *Journal of Instrumentation*, vol. 6, no. 11, p. P11002,
1520 2011.
- 1521 [62] R. Eusebi and on behalf of the CMS collaboration), “Jet energy corrections and
1522 uncertainties in cms: reducing their impact on physics measurements,” *Journal of
1523 Physics: Conference Series*, vol. 404, no. 1, p. 012014, 2012.
- 1524 [63] “Algorithms for b Jet identification in CMS,” Tech. Rep. CMS-PAS-BTV-09-001,
1525 CERN, 2009. Geneva, Jul 2009.
- 1526 [64] “Performance of b tagging at $\sqrt{s}=8$ tev in multijet, ttbar and boosted topology
1527 events,” no. CMS-PAS-BTV-13-001, 2013.
- 1528 [65] T. C. collaboration, “Identification of b-quark jets with the cms experiment,” *Journal
1529 of Instrumentation*, vol. 8, no. 04, p. P04013, 2013.
- 1530 [66] S. Dasu *et al.*, “CMS. The TriDAS project. Technical design report, vol. 1: The
1531 trigger systems,” 2000.
- 1532 [67] P. Sphicas, “CMS: The TriDAS project. Technical design report, Vol. 2: Data
1533 acquisition and high-level trigger,” 2002.
- 1534 [68] J. B. et al., “Calibration and Performance of the Jets and Energy Sums in the
1535 Level-1 Trigger ,” no. CMS IN 2013/006 (2013), 2013.

- 1536 [69] B. et al., “Study of Level-1 Trigger Jet Performance in High Pile-up Running
1537 Conditions,” no. CMS IN 2013/007 (2013), 2013.
- 1538 [70] J. J. Brooke, “Performance of the cms level-1 trigger,” Tech. Rep. CMS-CR-2012-322.
1539 CERN-CMS-CR-2012-322, CERN, Geneva, Nov 2012.
- 1540 [71] L. Randall and D. Tucker-Smith, “Dijet searches for supersymmetry at the large
1541 hadron collider,” *Phys. Rev. Lett.*, vol. 101, p. 221803, Nov 2008.
- 1542 [72] “SUSY searches with dijet events,” 2008.
- 1543 [73] “Search strategy for exclusive multi-jet events from supersymmetry at CMS,” Tech.
1544 Rep. CMS-PAS-SUS-09-001, CERN, 2009. Geneva, Jul 2009.
- 1545 [74] “Calorimeter Jet Quality Criteria for the First CMS Collision Data,” Tech. Rep.
1546 CMS-PAS-JME-09-008, CERN, 2010. Geneva, Apr 2010.
- 1547 [75] T. C. collaboration, “Performance of cms muon reconstruction in pp collision events
1548 at $\sqrt{s} = 7$ tev,” *Journal of Instrumentation*, vol. 7, no. 10, p. P10002, 2012.
- 1549 [76] “Search for supersymmetry in events with photons and missing energy,” Tech. Rep.
1550 CMS-PAS-SUS-12-018, CERN, Geneva, 2012.
- 1551 [77] M. Cacciari and G. P. Salam, “Pileup subtraction using jet areas,” *Phys.Lett.*,
1552 vol. B659, pp. 119–126, 2008.
- 1553 [78] Z. Bern, G. Diana, L. J. Dixon, F. Febres Cordero, S. Hoche, H. Ita, D. A. Kosower,
1554 D. Maitre, and K. J. Ozeren, “Driving missing data at next-to-leading order,” *Phys.
1555 Rev. D*, vol. 84, p. 114002, Dec 2011.
- 1556 [79] “Data-Driven Estimation of the Invisible Z Background to the SUSY MET Plus
1557 Jets Search,” Tech. Rep. CMS-PAS-SUS-08-002, CERN, 2009. Geneva, Jan 2009.

1558 Acronyms

1559	ALICE	A Large Ion Collider Experiment
1560	ATLAS	A Toroidal LHC ApparatuS
1561	APD	Avalanche Photo-Diodes
1562	BSM	Beyond Standard Model
1563	CERN	European Organization for Nuclear Research
1564	CMS	Compact Muon Solenoid
1565	CMSSM	Compressed Minimal SuperSymmetric Model
1566	CSC	Cathode Stripe Chamber
1567	CSV	Combined Secondary Vertex
1568	CSVM	Combined Secondary Vertex Medium Working Point
1569	DT	Drift Tube
1570	ECAL	Electromagnetic CALorimeter
1571	EB	Electromagnetic CALorimeter Barrel
1572	EE	Electromagnetic CALorimeter Endcap
1573	ES	Electromagnetic CALorimeter pre-Shower
1574	EMG	Exponentially Modified Gaussian
1575	EPJC	European Physical Journal C
1576	EWK	Electroweak Sector
1577	GCT	Global Calorimeter Trigger
1578	GMT	Global MuonTrigger
1579	GT	Global Trigger
1580	HB	Hadron Barrel
1581	HCAL	Hadronic CALorimeter

1582	HE	Hadron Endcaps
1583	HF	Hadron Forward
1584	HLT	Higher Level Trigger
1585	HO	Hadron Outer
1586	HPD	Hybrid Photo Diode
1587	LUT	Look Up Table
1588	L1	Level 1 Trigger
1589	LHC	Large Hadron Collider
1590	LHCb	Large Hadron Collider Beauty
1591	LSP	Lightest Supersymmetric Partner
1592	POGs	Physics Object Groups
1593	PS	Proton Synchrotron
1594	QED	Quantum Electro-Dynamics
1595	QCD	Quantum Chromo-Dynamics
1596	QFT	Quantum Field Theory
1597	RPC	Resistive Plate Chamber
1598	RCT	Regional Calorimeter Trigger
1599	RMT	Regional Muon Trigger
1600	SUSY	SUperSYmmetry
1601	SM	Standard Model
1602	SMS	Simplified Model Spectra
1603	SPS	Super Proton Synchrotron
1604	TF	Transfer Factor
1605	VEV	Vacuum Expectation Value
1606	VPT	Vacuum Photo-Triodes

1607 **WIMP** Weakly Interacting Massive Particle